

# Organic/Metal Interfaces: Electronic and Structural Properties

## DISSERTATION

zur Erlangung des akademischen Grades  
doctor rerum naturalium  
(Dr. rer. nat.)  
im Fach Physik

eingereicht an der  
Mathematisch-Naturwissenschaftlichen Fakultät I  
Humboldt-Universität zu Berlin

von  
Herrn Dipl.-Phys. Steffen Duhm  
geboren am 29.06.1978 in Waldenburg

Präsident der Humboldt-Universität zu Berlin:  
Prof. Dr. C. Marksches

Dekan der Mathematisch-Naturwissenschaftlichen Fakultät I:  
Prof. Dr. C. Limberg

Gutachter:

1. Dr. Norbert Koch
2. Prof. Dr. Recardo Manzke
3. Prof. Dr. Frank Schreiber

eingereicht am: 20.03.2008  
Tag der mündlichen Prüfung: 17.07.2008

## Abstract

This work addresses several important topics of the field of *organic electronics*. The focus lies on organic/metal interfaces, which exist in all organic electronic devices. Physical properties of such interfaces are crucial for device performance. Four main topics have been covered: (i) the impact of molecular orientation on the energy levels, (ii) energy level tuning with strong electron acceptors, (iii) the role of thermodynamic equilibrium at organic/organic homo-interfaces and (iv) the correlation of interfacial electronic structure and bonding distance. To address these issues a broad experimental approach was necessary: mainly ultraviolet photoelectron spectroscopy was used, supported by X-ray photoelectron spectroscopy, metastable atom electron spectroscopy, X-ray diffraction and X-ray standing waves, to examine vacuum sublimed thin films of conjugated organic molecules (COMs) in ultrahigh vacuum.

(i) A novel approach is presented to explain the phenomenon that the ionization energy in molecular assemblies is orientation dependent. It is demonstrated that this is due to a macroscopic impact of intramolecular dipoles on the ionization energy in molecular assemblies. Furthermore, the correlation of molecular orientation and conformation has been studied in detail for COMs on various substrates. (ii) A new approach was developed to tune hole injection barriers ( $\Delta_h$ ) at organic/metal interfaces by adsorbing a (sub-) monolayer of an organic electron acceptor on the metal electrode. Charge transfer from the metal to the acceptor leads to a chemisorbed layer, which reduces  $\Delta_h$  to the COM overlayer. This concept was tested with three acceptors and a lowering of  $\Delta_h$  of up to 1.2 eV could be observed. (iii) A transition from vacuum-level alignment to molecular level pinning at the homo-interface between a lying monolayer and standing multilayers of a COM was observed, which depended on the amount of a pre-deposited acceptor. The measured shift in the vacuum level between monolayer and multilayer coverage was direct evidence for thermodynamically driven charge transfer between molecular layers. (iv) A clear correlation between the strength of chemical bonding of COMs and the bonding distance to metal substrates could be shown. All these findings lead to a better understanding of organic/metal interface physics and may help to enhance performance of organic devices in the future.

### Keywords:

organic/metal interfaces, hole injection barrier, photoelectron spectroscopy, molecular orientation

## Zusammenfassung

In dieser Arbeit werden Fragestellungen aus dem Gebiet der *Organischen Elektronik* behandelt, hauptsächlich Grenzflächen zwischen Metallen und konjugierten organischen Molekülen (KOM), die Bestandteil fast aller Bauteile der Organischen Elektronik sind. Physikalische Eigenschaften solcher Grenzflächen bestimmen die Effizienz von Bauteilen. Im einzelnen wird behandelt: (i) der Einfluss der Orientierung von Molekülen auf die Energieniveaus, (ii) das gezielte Einstellen von Energieniveaus mithilfe starker Elektronenakzeptoren, (iii) die Rolle des thermodynamischen Gleichgewichts an organisch-organischen Grenzflächen und (iv) der Zusammenhang zwischen elektronischer Struktur an Grenzflächen und dem Bindungsabstand. Dazu war ein breiter experimenteller Ansatz nötig: Es wurden hauptsächlich Messungen mit ultravioletter Photoelektronenspektroskopie, unterstützt von Röntgenphotoelektronenspektroskopie, Spektroskopie mit metastabilen Atomen, Röntgenbeugung und stehenden Röntgenwellen, an vakuumsublimierten organischen dünnen Schichten im Ultrahochvakuum durchgeführt.

(i) Eine neue Erklärung für das Phänomen der orientierungsabhängigen Ionisationsenergie in molekularen Verbänden wird gegeben. Dabei kommt es zu einem makroskopischen Einfluss intramolekularer Dipole auf die Ionisationsenergie. (ii) Es wurde eine neue Methode gefunden, um die Lochinjektionsbarriere ( $\Delta_h$ ) an organisch/metallischen Grenzflächen zu kontrollieren. Dazu wurden (Sub-)Monolagen starker Elektronenakzeptoren auf Metalloberflächen adsorbiert. Dabei kommt es zu einem Ladungstransfer, der  $\Delta_h$  eines darauf aufgedampften KOMs verringern kann. Das Konzept wurde mit drei Akzeptoren getestet und  $\Delta_h$  konnte um bis zu 1.2 eV verringert werden. (iii) Ein akzeptorvorbedeckungsabhängiger Übergang von Vakuumniveauangleichung zu einem "Pinning" molekularer Niveaus an Homogrenzflächen eines KOMs mit liegender Mono- und stehender Multilage konnte beobachtet werden – ein direkter Beweis für einen thermodynamisch getriebenen Ladungstransfer. (iv) Ein klarer Zusammenhang zwischen der Stärke der chemischen Bindung und dem Bindungsabstand von KOM zu Metallsubstraten konnte gezeigt werden. Die Ergebnisse führen zu einem besseren Verständnis der Physik von KOM/Metall Grenzflächen und können zu einer Verbesserung der Leistung von organischen Bauteilen führen.

### Schlagwörter:

organischer Halbleiter/Metall Grenzflächen, Lochinjektionsbarriere, Photoelektronenspektroskopie, molekulare Orientierung

# Contents

<b>1</b>	<b>Introduction</b>	<b>1</b>
<b>2</b>	<b>Fundamentals</b>	<b>4</b>
2.1	Organic/metal interfaces . . . . .	4
2.1.1	Charge injection . . . . .	4
2.1.2	Energy level alignment . . . . .	6
2.1.3	Structural properties . . . . .	12
2.2	Methods . . . . .	16
2.2.1	Photoelectron spectroscopy . . . . .	16
2.2.2	Metastable atom electron spectroscopy . . . . .	24
2.2.3	X-ray diffraction . . . . .	26
2.2.4	X-ray standing waves . . . . .	27
<b>3</b>	<b>Materials and Experimental Setups</b>	<b>30</b>
3.1	Materials . . . . .	30
3.1.1	Organic Adsorbates . . . . .	30
3.1.2	Substrates . . . . .	33
3.2	Experimental Setups and Data Analysis . . . . .	33
<b>4</b>	<b>Results and Discussion</b>	<b>39</b>
4.1	Molecular Orientation . . . . .	39
4.1.1	Lying monolayer/standing multilayer . . . . .	40
4.1.2	Upper limit for orientation induced polarization effects	48
4.1.3	Orientation dependent IE of COMs . . . . .	49
4.1.4	Influence of substrate on molecular growth . . . . .	52
4.2	Charge Transfer Complexes . . . . .	65
4.2.1	F4-TCNQ . . . . .	65
4.2.2	FAQ . . . . .	72
4.2.3	TCAQ . . . . .	77
4.3	Energy level alignment mechanisms . . . . .	80
4.4	Bonding Distance . . . . .	85

4.4.1	PTCDA on metals . . . . .	85
4.4.2	Perfluoropentacene and Pentacene . . . . .	94
<b>5</b>	<b>Conclusions and Outlook</b>	<b>100</b>
	<b>Bibliography</b>	<b>104</b>
	<b>Abbreviations</b>	<b>125</b>
	<b>Publications</b>	<b>127</b>
	<b>Acknowledgements</b>	<b>131</b>



# Chapter 1

## Introduction

The field of *organic electronics* is one of the fastest growing research-fields over the past few years [1–3]. Enormous progress in both, understanding of fundamental physics and device performance could be achieved. Some applications like organic photovoltaic devices [4–6], organic field effect transistors [7–9] or organic light emitting diodes [10, 11] are entering the market. The major advantages are low-cost and low-energy fabrication as well as mechanical flexibility. But still a gap exists between the comprehension of classic, inorganic solid state physics with an immense basis of *common knowledge* [12–14] and the comprehension of organic solid state physics [15–17]. Since the number of different conjugated organic molecules (COMs) is virtually unlimited and hence the bulk properties of active materials in organic devices can be altered easily by taking different COMs, especially the functional interfaces of COMs attract interest.

In nearly all COM based devices organic/metal interfaces occur [18–21]. For charge transport in devices like organic solar cells, organic field effect transistors or organic light emitting diodes [Fig. 1.1] the charge carrier injection

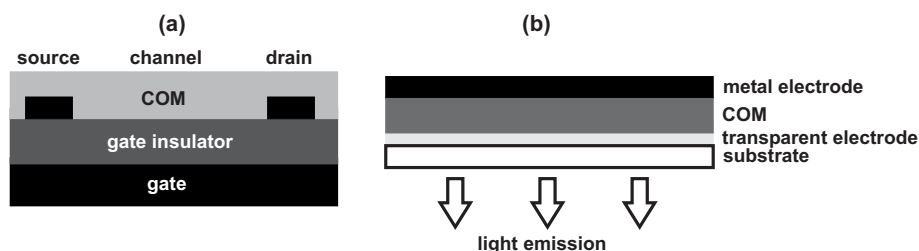


Figure 1.1: Schematic cross section of (a) an organic field effect transistor and (b) an organic photovoltaic device with organic/metal interfaces at (a) the source/COM and drain/COM contact and (b) the electrode/COM contact.

tion barriers at these interfaces often act as bottlenecks. It was shown that lowering the charge carrier injection barrier can enhance device performance by orders of magnitude [12]. For this purpose it is indispensable to get a deeper insight in organic/metal interface properties, since charge injection barriers not only depend on electronic but also on structural properties like molecular orientation, bonding distances or adsorption induced conformation changes of molecules on metal substrates. Therefore, I focused in this work on vacuum sublimed organic thin film model systems on metals to correlate their electronic and structural properties.

This work is organized as follows: In Chapter 2 an introduction into organic solid state physics and the experimental techniques is given, followed by a description of the investigated COMs and details of the experimental setups in Chapter 3. In the main part –Chapter 4– the experimental results are presented and discussed. In Chapter 5 conclusions and outlooks are given.

Chapter 4 starts with the molecular orientation of COMs on metals and the interplay of molecular orientation and electronic structure. As a model system  $\alpha,\omega$ -dihexylsexithiophene (DH6T) is chosen, since it will be shown that this rodlike molecule exhibits a peculiar growth mode on metals: The monolayer is lying flat on the substrate while subsequent multilayers are standing nearly upright. This orientational transition is accompanied by a shift of molecular levels, which lowers the hole injection barrier ( $\Delta_h$ ) at the organic/metal interface by 0.5 eV. In literature, shifts of this order of magnitude at lying/standing interfaces have been assigned to different intermolecular polarization efficiency for the different molecular crystal phases [22–24]. It will be shown that in contrast to common believe the upper limit of such polarization effects is only 0.15 eV. It will be demonstrated that the molecular orbital shift can be assigned to an orientation dependent ionization energy of molecular crystals. This idea is similar to the concept of different work functions of different orientations in metal single crystals. However, it has not been employed in the context of van der Waals crystals before. Furthermore, the influence of the substrate on molecular growth will be discussed in detail.

In the following part, I will present an approach to lower  $\Delta_h$  at organic/metal interfaces. For this purpose, strong electron accepting molecules are used, which undergo a charge transfer with metal substrates. It will be demonstrated that this charge transfer leads to an interface dipole at the organic/metal interface. This dipole increases the effective substrate work function. The molecular orbitals of subsequently deposited COMs are aligned to this new work function and therefore the hole injection barrier is lowered. With this novel concept the hole injection barrier of virtually any COM can be lowered by up to 1.2 eV. Furthermore, the hole injection barrier can be



tuned in the same energy range by controlling the acceptor pre-coverage.

The combination of the energy level tuning concept with the lying/standing transition of DH6T leads to a detailed insight into the energy level alignment mechanisms at organic/organic homo-interfaces. Depending on the acceptor pre-coverage of the metal substrate a transition from vacuum level alignment to Fermi-level pinning can be observed at the lying/standing interface of DH6T. Fermi-level pinning is related with a thermodynamically driven charge transfer across a hexyl layer, which was thought to exhibit insulating properties before [25].

I will discuss the bonding distance of COMs on metals and demonstrate that bonding distances are directly correlated with the interfacial electronic structure of chemisorbed molecules. Measuring the bending of molecules on metals (i.e. adsorption-induced conformation changes) allows to determine the strength of adsorption induced intramolecular dipoles. This is important, since these dipoles have to be considered for an appropriate description of the energy level alignment at organic/metal interfaces.

The results of this work shed light on the complex phenomena at organic/metal interfaces. The correlation of different effects like interface dipoles, charge transfer, bonding distance or molecular orientation is necessary, since all these effects contribute to the energy level alignment at organic/metal interfaces. This correlation is made possible by the combination of a number of experimental techniques like photoelectron spectroscopy, metastable atom electron spectroscopy, X-ray diffraction and X-ray standing waves. The results allow an improved control of interface properties and may lead to better organic device performance in the near future.

# Chapter 2

## Fundamentals

This chapter provides a motivation for the experimental work in more detail. The charge injection as a key issue for organic device performance is highlighted and an introduction to related topics is presented. Then the experimental techniques used within this work are described.

### 2.1 Organic/metal interfaces

In this section the importance of organic/metal interfaces is highlighted and basic physics at such interfaces, including charge injection, energy level alignment and structural properties, are described in more detail.

#### 2.1.1 Charge injection

In order to properly understand the organic/metal interface energetics and the charge injection across such interfaces, some fundamental aspects of organic solid state physics [15–17, 26, 27] will be highlighted. The electronic structure of typical organic molecules consists of  $\pi$ - and  $\sigma$ -bonds. In conjugated organic molecules –mainly treated in this work–  $\pi$ -electrons are delocalized over a molecule. This closed shell structure leads to rather weak intermolecular interactions and molecular crystals are typically governed by van der Waals interactions. Due to the anisotropic shape of most COMs, also most physical properties in molecular crystals exhibit high anisotropy. The weak intermolecular interactions lead to a low density of free charge carriers, that are delocalized over the whole structure, compared to their inorganic counterparts [17, 28]. In addition, the charge carrier mobility in most organic crystals is very low. Thus, the mean free path of the charge carriers is often in the order of the intermolecular distances. Therefore no or only

low distinct band dispersion [29–31] exists. Charge is mainly transported by hopping transport [32–34], i.e. by a tunneling based process. In the Bässler-model [35] the charge transport is described by hopping of charge carriers induced by an external electric field to neighbour molecules with slightly larger or smaller energy. Moreover, since the space charge region at organic/metal or organic/organic interfaces is inversely proportional to the space charge density [12], usually no band bending occurs in organic thin films at organic/metal or organic/organic interfaces. However, all transport properties in organic crystals and organic thin films strongly depend on the degree of order and the density of defects of the organic assembly. For example the temperature dependence of the charge carrier mobility  $\mu$  is ranging from a band-like  $\mu \propto T^{-1}$  dependence for highly ordered molecular crystals to a hopping-like  $\mu \propto T$  dependence for relatively unordered organic thin films [15]. Therefore, the description of the electronic structure of organic solids with “bands” is often not useful. The characterization of energy levels is mainly done in the picture of (un)occupied molecular orbitals. The energetic position of the HOMO (highest occupied molecular orbital) and the LUMO (lowest unoccupied molecular orbital) levels are most useful for the description of interface properties, because these are the transport levels. For the description of the transport levels, polarization effects in organic materials have to be considered. In general, a charged particle polarizes the surrounding matter [36], i.e. in the case of an organic solid a charged molecule polarizes its neighbours. The polarization follows the charged molecule quasi instantaneously [15]. The positive polarization energy ( $P_h$ ) is given by the difference of the ionization energy of the free molecule ( $IE_M$ ) and of the molecular crystal (or generally the molecular solid state) ( $IE_C$ ) [15]:

$$P_h = IE_M - IE_C. \quad (2.1)$$

The negative polarization energy ( $P_e$ ) is given analogously by the differences of the electron affinities ( $A_i$ ):

$$P_e = A_C - A_M. \quad (2.2)$$

The transport levels are shifted by  $P_h$  ( $P_e$ ) with respect to the gas phase ground state.

In COM based devices often the injection limited current regime is observed when current flows [37, 38], i.e. the current density in the device is only determined by the charge carrier injection barriers at the interfaces. In this case the current density across an organic/metal interface can be approximated by the Richardson-Schottky-formula [12]:

$$j = AT^2 \exp\left(-\frac{\Delta_h}{k_B T}\right) \left[ \exp\left(\frac{qU}{k_B T}\right) - 1 \right] \quad (2.3)$$

( $j$  denotes the current density,  $A$  the Richardson-constant,  $\Delta_h$  the hole injection barrier,  $T$  temperature,  $k_B$  the Boltzmann-constant,  $q$  the elementary charge and  $U$  the bias voltage). This equation shows the enormous impact of  $\Delta_h$  on device performance, since the dependence between the current density and the hole injection barrier is exponential. Small changes in  $\Delta_h$  can therefore change the current density across the interface by orders of magnitudes. For low injection barriers the situation can change to the space charge limited current (SCLC) regime, where the current density across an organic layer is given by the Mott-Gurney-formula [15]:

$$j = \frac{9}{8} \varepsilon \varepsilon_0 \mu \frac{U^2}{d^3} \quad (2.4)$$

( $j$  denotes the current density,  $\varepsilon$  dielectric constant,  $\varepsilon_0$  vacuum permittivity,  $\mu$  mobility,  $U$  bias voltage and  $d$  layer thickness). In this case desirable for applications, which can usually only be achieved for very low  $\Delta_h$ , the current density is independent of  $\Delta_h$ . The magnitude of  $\Delta_h$  is determined by the position of the HOMO level at the organic/metal interface, therefore the energy level alignment at organic/metal interfaces must be discussed in more detail.

## 2.1.2 Energy level alignment

### Vacuum alignment vs. Fermi-level pinning

The energy level alignment at organic/metal interfaces is a key issue for the performance of devices in the field of organic electronics [18, 19]. Two rather simple models are often employed as energy level alignment mechanism to estimate  $\Delta_h$ : (i) the *Schottky-Mott limit*, where the energetic positions of the molecular levels are strictly determined by the work function of the metal substrate involving vacuum level alignment, and (ii) *Fermi-level pinning*, where the energetic positions of the molecular levels are pinned relative to the Fermi-level ( $E_F$ ) of the metal by charge transfer between the substrate and adsorbate [39, 40]. However, these models do not incorporate the complex processes determining the energy level alignment at organic/metal interfaces, like the chemical interaction between substrate and adsorbate [41], the electron push-back effect [18, 42–44], interface dipoles [18, 45, 46], or the adsorption-induced geometry change of the molecules [47–49].

To satisfactorily describe the energy level alignment at organic/metal interfaces, modified models that are well developed for inorganic semiconductor/metal interfaces can be used as a first step, taking into account the comparably weak adsorption of organic molecules on metal substrates and

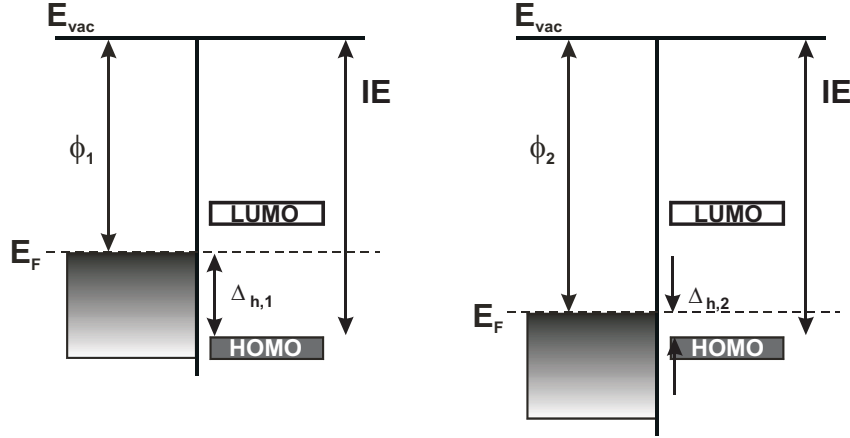


Figure 2.1: Schematic energy level diagram of interfaces between metals with two different work functions ( $\phi_i$ ) and a COM in the Schottky-Mott-limit, leading to different hole injection barriers ( $\Delta_{h,i}$ ).

the absence of free charge carriers in most organic semiconductors, which inhibits band bending.

First, the case of strict vacuum level ( $E_{vac}$ ) alignment of energy levels will be considered. In this case  $\Delta_h$ , which is defined as energy difference between the Fermi-level of the metal and the HOMO onset of the COM, is given by the difference between the work function ( $\phi$ )<sup>1</sup> of the metal and the ionization energy (IE) of the COM:

$$\Delta_h = IE - \phi. \quad (2.5)$$

Therefore, high work function electrodes lead to low hole injection barriers at the organic/metal interface [Fig. 2.1].

However, strict vacuum level alignment is rather the exception than the rule. For physisorbed molecules on metal surfaces the *electron push-back effect* [18, 19, 43] has to be considered. The metal work function is the sum of a bulk part, which is determined by the bulk chemical potential and a surface part, which is determined by the electron density distribution on the surface compared with the bulk, resulting in a surface dipole [36, 50]. Physisorbed molecules on metal surfaces push back the metal electron density spilling out of the pristine metal surface. Therefore, the part of the metal work function consisting of the surface dipoles is decreased and the vacuum level exhibits a shift ( $\Delta_{vac}$ ) [Fig. 2.2] upon deposition of a molecular layer. The value of

<sup>1</sup>In this work as usual in *organic electronics* “ $\phi$ ” represents energy values in contrast to potential values. Moreover, sometimes  $\phi$  is used for a COM, which is adsorbed on a metal substrate system, although strictly spoken,  $\phi$  of a semiconductor is not defined. In such a case,  $\phi$  is defined as difference between substrate  $E_F$  and adsorbate  $E_{vac}$ .

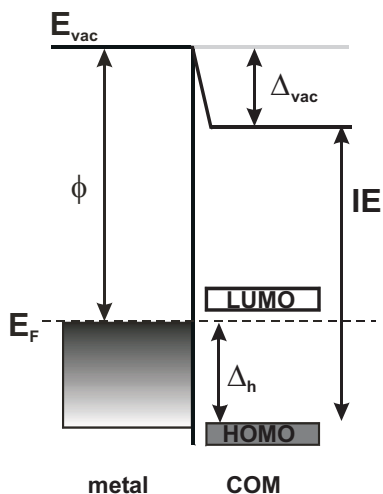


Figure 2.2: Interface energetics between a metal and a COM including the interface dipole, which is causing the shift in the vacuum level  $\Delta_{vac}$ .

$\Delta_{vac}$  can be larger than 1 eV [18, 43, 51, 52] and differs for each particular metal/COM pair. Although  $\Delta_{vac}$  increases  $\Delta_h$ , the principle of high work function electrodes causing low hole injection barriers is still valid if the push-back effect is considered. In literature the decrease of  $E_{vac}$  caused by the push-back effect is often termed “interface dipole”, although an existing dipole is decreased by the adsorption of the molecules.

Vacuum level alignment is one of the two simple energy level alignment mechanisms at organic/metal interfaces. The second is Fermi-level pinning. In the case of Fermi-level pinning one has to deal with charged molecules, so called polarons. The additional charge in a molecule leads to changes in the molecular conformation and the intramolecular binding lengths [53, 54]. These changes consequently lead to a rearrangement of the molecular energy levels [Fig. 2.3]. For both positive and negative polarons, the rearrangement reduces the energy gap compared to the neutral state. The energy difference between neutral and polaron state is the polaron relaxation energy. The values of the polaron relaxation energies for organic thin films are in the range of several hundred meV [39, 55].

The polaron relaxation energy has high impact on the energy level alignment at organic/metal interfaces. Considering a COM with a given IE vacuum level aligned on different metals, with increasing metal  $\phi$ ,  $\Delta_h$  will first decrease. But if the IE of the COM minus its positive polaron relaxation energy is in the range of the metal  $\phi$ , the polaron level reaches an energetic position just below  $E_F$ . For a further increase in  $\phi$  the polaron level cannot move above the Fermi-level, since charge can flow across the organic/metal interface driven by thermodynamics. In this case the HOMO is slightly positively charged and the polaron level near  $E_F$  is partially occupied. This new occupied state pins the molecular levels with respect to  $E_F$  [39, 40, 55].

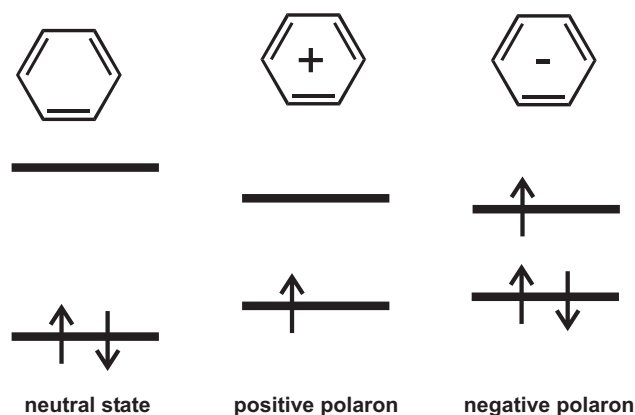


Figure 2.3: Schematic energy level diagram for a molecule in the neutral state and in positively or negatively charged states, respectively.

An interface dipole is formed as consequence of the charge transfer and the vacuum level is lowered.  $\Delta_h$  becomes independent of  $E_{vac}$  and cannot be lowered furthermore by the use of electrodes with higher work functions. Fig. 2.4 demonstrates the situation at an organic/metal interface in the case of Fermi-level pinning for metals with different work functions. In opposite to vacuum level alignment [Fig. 2.1] an increase in  $\phi$  leaves  $\Delta_h$  undisturbed, but leads to an increase in  $\Delta_{vac}$ .

Thus, in thermodynamic equilibrium the positive polaron relaxation energy

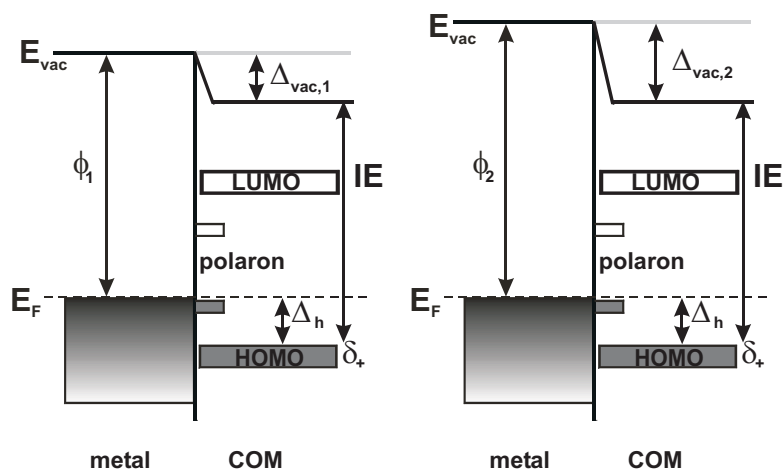


Figure 2.4: Organic/metal interface energetics in the case of Fermi-level pinning for metals with two different work functions. “polaron” symbolizes the polaron level near  $E_F$  existing just directly at the interface.

of a COM on a metal surface gives the smallest  $\Delta_h$  that can be achieved independent of the specific mechanism of energy level alignment [39, 55, 56]. So far the choice of a high work function electrode was the only option to achieve this lowermost hole injection barrier for a particular COM. But in organic electronics additional electrode parameters like surface roughness, processing features or stability play crucial roles. Therefore mechanisms are to be found that allow to achieve the smallest possible  $\Delta_h$  value also for metals with low  $\phi$ .

### Tuning the hole injection barrier

One approach to lower  $\Delta_h$  of a given metal/COM pair is the pre-coverage of the metal surface with a strong electron accepting molecule, which undergoes a charge transfer (CT) with the metal and therefore varies the surface potential of the substrate. The molecular orbital levels of a subsequently deposited COM may be aligned to the modified vacuum level leading to a lowering of the hole injection barrier.

CT between different COMs is a well known phenomenon and resulting charge transfer complexes (CTC) have been widely studied [57–61]. CT occurs, if the electron affinity of the electron accepting molecule is larger than the ionization energy of the electron donating molecule. In this case electrons can be transferred from the donor to the acceptor. The amount of transferred charge ranges from an elementary charge per molecule for charge transfer salts to small fractions of a elementary charge per molecule for systems where a hybridization of donor and acceptor levels takes place [62]. Similar to a polaron a CT also leads to a rearrangement of the molecular levels. In Fig. 2.5 the schematic electronic structure of the acceptor is shown. The neutral acceptor LUMO is - at least partially - filled with negative charge. The former LUMO (now the HOMO of the charged molecule) is shifted to higher binding energies. In addition to the stabilization of the LUMO, the CT causes also an energetic relaxation of the HOMO due to a change of the molecular conformation. The CT leads also to the buildup of a dipole between the negatively charged acceptor and the positively charged donor.

In recent works [63–69] such organic-organic CT was claimed to be responsible for different observations. Co-evaporation of acceptors with electron donor molecular species to form hole transport layers improved device performance [63, 64] in organic light emitting devices significantly. This was attributed to a reduction of  $\Delta_h$  due to the formation of a narrow space charge region (several nm) near the metal contact facilitated by charge transfer between the acceptor and the organic donor matrix [65–67]. The conductivity in thin doped films increased by several orders of magnitude, both for



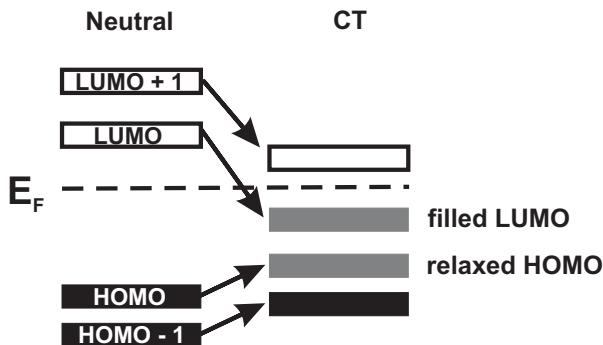


Figure 2.5: Schematic energy diagram of HOMO and HOMO-1 as well as LUMO and LUMO+1 of a neutral electron accepting molecule (left side) and a negatively charged acceptor (right side) with the Fermi-level ( $E_F$ ) serving as the energy reference. The arrows indicate the origin of the newly distributed levels in the negatively charged acceptor.

crystalline (vanadyl-[68] and zinc-phthalocyanine; ZnPc [65, 69]) and amorphous (ZnPc[69], and N,N'-bis-(1-naphthyl)-N,N'-diphenyl-1,1-biphenyl-4,4'-diamine;  $\alpha$ -NPD[67]) samples. Another important issue is the space-charge region formation mechanism in doped organic systems in the absence of an electric field and the associated energy-level bending [65–67]. However, due to the polaronic effects in organic materials, the explanation of these effects by “doping” has to be treated with caution. Doping requires free charge carriers, which can overcome the mutual Coulomb attraction in doped systems. This assumption is, particularly in disordered systems, no longer valid [70]. The observed phenomena may therefore not be due CTC formation between electron accepting and donating molecules, but due to electrode interface modifications via the accepting molecule. These modifications and the resulting changes in the energy level alignment have not yet been investigated in detail.

Strong electron accepting molecules may undergo a CT with metals. In this case a thin layer of acceptors in the monolayer range on the metal surface may lead to an interface dipole moment pointing towards to the surface. The impact of this interface dipole on the work function can be approximated by the Helmholtz equation:

$$\Delta\phi = \frac{q \cdot n_D \cdot \mu_{\perp}}{\varepsilon\varepsilon_0} \quad (2.6)$$

(  $\Delta\phi$ : change in the work function,  $q$ : elementary charge,  $n_D$ : dipole surface density,  $\mu_{\perp}$ : dipole moment perpendicular to the surface,  $\varepsilon$ : dielectric constant,  $\varepsilon_0$ : vacuum permittivity). The Helmholtz equation does not include the interaction of the dipoles with external electric fields, such as those due

to dipoles of other molecules. Therefore, the Helmholtz equation is valid only for very small acceptor-coverages, where the dipole-dipole interaction can be neglected. Otherwise the polarizability of the molecules leads to a decrease of the net-dipole moment. In this case the Topping-model [71] has to be applied, which includes the effect of depolarization; or an effective, coverage dependent dielectric constant can be used, which yields the same results [72]. However, for prototypical organic monolayers of molecules with a permanent dipole the depolarization effect is only in the range of 100 meV [72, 73]. Thus, the Helmholtz equation can be regarded as a good approximation to estimate the impact of CT-induced dipoles on the substrate work function.

The energy levels of subsequently deposited COMs are aligned to the modified work function and the hole injection barrier of the COM on the acceptor pre-covered metal substrate is lowered. Thus, the effects described in Refs. [63–69] mentioned above are influenced by a metal-organic CT. Furthermore, the linear relationship between  $\Delta\phi$  and  $n_D$  can enable a simple tuning of  $\Delta_h$  of virtually every COM at any metal surface by varying the acceptor pre-coverage. This tuning is independent of the ability to form CTC between the acceptor and the subsequently deposited COM. In Section 4.2 the energy level tuning approach will be described with several acceptors and different overlayer COMs. It will be demonstrated that  $\Delta_h$  can be lowered by up to 1.2 eV.

### 2.1.3 Structural properties

Electronic properties at organic/metal interfaces strongly depend on the structural arrangement of organic molecules in thin films on the metal substrates [42, 74–78]. Therefore, molecular growth and order has to be considered, to get a comprehensive understanding of the energy level alignment at organic/metal interfaces.

#### Vacuum sublimed thin films

Organic thin films can be deposited by solution based processes or vacuum sublimation. Since no solvent is involved in the adsorption process of vapor grown thin films, the growth behavior only depends on the substrate-adsorbate and the adsorbate-adsorbate interaction strength as well as on the environment of thin film preparation. In this work only vacuum sublimed organic thin films are investigated, since they allow to study the intrinsic material properties. Ultrahigh vacuum conditions are necessary in order to guarantee a well defined substrate for COM deposition. Under ambient conditions surfaces are covered with undefined adsorbates, particularly water and

organic composites. Also the adsorbed COMs themselves are influenced by ambient conditions, especially by immediate oxidation. The growth of vacuum sublimed organic thin films is well investigated [79–83]. However, due to the extraordinary diversity of the physical properties crucial for thin film growth, like molecular shape, weight or intramolecular charge distribution (intrinsic multipoles), it is difficult to point out general rules.

One has to distinguish between physisorbed (physically adsorbed) and chemisorbed (chemically adsorbed) molecules. Although the transition is still under discussion and fluent [84] a common denominator is that physisorbed molecules are weakly bound and the molecular as well as the electronic structure stays undisturbed after adsorption, whereas chemisorbed molecules develop covalent or ionic bonds with the substrate. The gain in enthalpy upon adsorption for physisorbed molecules is in the order of 20 kJ/mol, whereas for chemisorbed molecules this gain is about a magnitude higher [84]. Most COMs physisorb on noble metals within this definition, but one has still to look with care on this nominally physisorbed systems. “Weak chemisorption” should be a better term to describe this interaction, since also nominally physisorbed molecules are slightly distorted compared with gas-phase molecules. But of course, depending on the properties of the molecule also strong chemisorption can be observed: Molecules with large ionization energies or low electron affinities can even hybridize with the metal substrate. The dominant substrate/molecule interaction for physisorbed molecules is the van der Waals force. The resulting potential  $V$  between a surface and an adsorbing molecule can be described with the Lennard-Jones-Potential [84]:

$$V = -4V_0 \left[ \left( \frac{\sigma}{r} \right)^6 - \left( \frac{\sigma}{r} \right)^{12} \right] \quad (2.7)$$

( $V_0$  is the minimal potential energy,  $\sigma$  an effective molecular diameter and  $r$  the surface-molecule distance). The  $(1/r)^6$  term includes the attractive van der Waals forces and the  $(1/r)^{12}$  term the repulsive forces due to the Pauli principle and the increased Coulomb repulsion due to less sufficient screening of the nuclei [84]. This potential favors an overlap of molecular  $\pi$ -orbitals with delocalized metal bands leading often to a planar adsorption geometry of ring-shaped aromats like benzenes or thiophenes. For rodlike oligomers based on these building blocks an analogous orientation was observed, leading to *lying* molecules on metal surfaces, i.e. molecules with their long-axes and molecular plane parallel to the substrate. These molecules undergo often a gradual transition from lying to almost standing molecules as a function of several hundred layers [85–87]. On weakly interacting substrates like  $\text{SiO}_2$  rodlike molecules usually prefer to grow in an almost standing orientation from initial crystal growth, since this orientation allows better overlap of

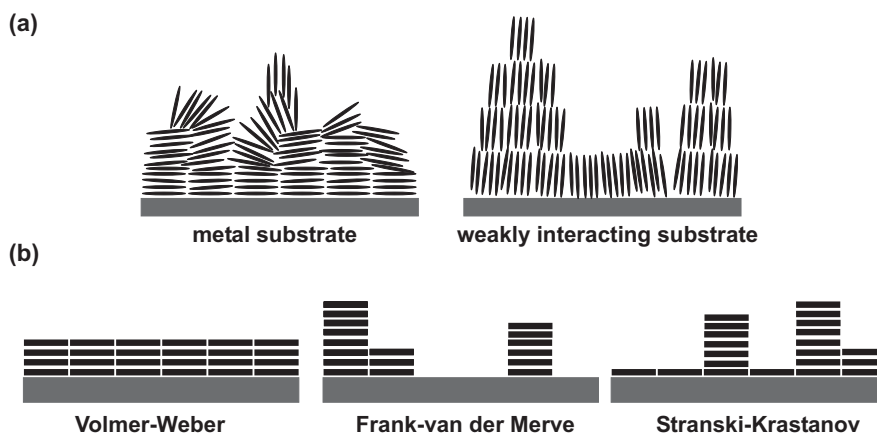


Figure 2.6: (a) In each case one of many possible schematic growth scenarios for rodlike molecules on a metal (left) or a weakly interacting (right) substrate. (b) The three well known typical growth modes.

the molecular  $\pi$ -systems [79, 82]. Two sketches illustrating the scenarios are shown in Fig. 2.6 (a).

The growth mode depends on the balance of adhesion energy at the interface and cohesion energy in the bulk. Three typical growth modes can be distinguished: Volmer-Weber (layer by layer), Frank-van der Merve (island) and Stranski-Krastanov (islands on wetting layer) [Fig. 2.6 (b)]. However, since diffusion on different timescales –ranging from diffusion during adsorption to diffusion on a timescale of months– is also possible, an organic thin film can change between the different growth modes with time, e.g. dewetting of the substrate is observed in certain cases [88]. In addition, polymorphism is rather the rule than the exception [89, 90].

### Molecular orientation

Due to the structural anisotropy of many organic molecules nearly all physical properties of organic thin films depend on the molecular orientation relative to the substrate [42, 74–78]. Some of these properties, like charge injection, photoluminescence or transport properties directly impact the efficiency of devices in organic electronics. It has been found that the current density across organic/metal interfaces in model devices is much higher for standing rodlike COMs than for lying rodlike COMs, which was explained by a decreased hole injection barrier [42, 91]. Therefore, in this work one focus lies on the interplay of molecular orientation and electronic structure. It is known that different molecular orientations affect the electronic structure of organic thin films [22–24]. Various intermolecular interactions have been suggested

to be the reason for these changes. Especially the shift of molecular orbitals towards  $E_F$  for standing molecules compared to films with a almost lying orientation has been explained through a change in the polarization ability by surrounding molecules [22–24]. However, the effect of polarization may be overestimated. In this work a general concept is presented to explain this effect with an orientation dependent ionization energy of molecular crystals.

### Bonding distance

Another structural parameter that has to be considered for the energy level alignment is the bonding distance ( $d_h$ ) of adsorbates on substrates [Fig. 2.7].

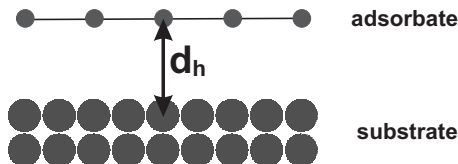


Figure 2.7: Bonding distance ( $d_h$ ) of an adsorbate molecule upon a substrate surface.

A strong correlation between  $d_h$  and the bonding type of the adsorbate to the substrate is expected. In weakly interacting systems (physisorption) the bonding distance is expected to be rather large and small variations of  $d_h$  do not significantly affect the interfacial electronic structure [92]. In contrast, for strongly interacting systems  $d_h$  is expected to decrease and strongly depends on the bonding type [47, 48, 93, 94]. In particular for charge transfer systems it is expected that a strong correlation between the interfacial charge transfer and the bonding distance exists, which again depends on the reactivity of the metal substrate.

Not only the distance between adsorbate and substrate, but also (adsorption induced) conformation changes of molecules on metal substrates influence the energy level alignment, since they can lead to intramolecular dipole moments, which have to be considered in the energy level alignment. For molecules with an intrinsic dipole [95] and for the case of strongly interacting systems, where it is obvious that dipoles can be induced by adsorption [48, 49], bending induced dipole moments have been reported in literature. However, the role of conformation change induced dipoles in the case of initially planar molecules on weakly interacting substrates have so far not been explored. It can be assumed that also in this case adsorption induced dipoles exist, which have to be considered in energy level alignment considerations of such systems.

## 2.2 Methods

To obtain the information that is needed for a comprehensive understanding of organic/metal interfaces a broad experimental approach is necessary. Since this work is focused on the electronic structure, the most frequently used experimental technique was ultraviolet photoelectron spectroscopy, which directly probes the valence electronic structure of the sample. As pointed out in the previous chapter, the electronic structure is closely related to structural properties; therefore, in selected cases a combination of ultraviolet photoelectron spectroscopy investigations with techniques probing the structural arrangement of the sample, like metastable atom electron spectroscopy and X-ray diffraction, has been performed. To assess information about the bonding distances X-ray standing wave measurements were performed. In this section the main principles of these techniques are described.

### 2.2.1 Photoelectron spectroscopy

Photoelectron spectroscopy (PES) is a widely used technique to study the electronic properties of conjugated organic material [18, 41, 96, 97], a detailed

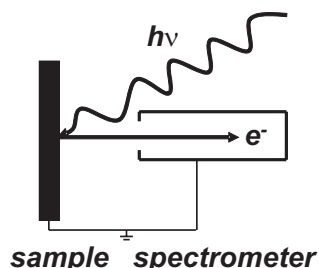


Figure 2.8: Scheme of the fundamental photoemission process.

description of the photoemission process can be found in various textbooks [98–100]. As PES yields direct information on the density of occupied states, the electronic structures of samples can be monitored in detail. Moreover, information about chemical bonding, morphology and intermolecular interactions, to give just some examples, can be obtained.

In Figure 2.8 the basic process of PES is sketched. Depending on the excitation energy PES is commonly divided into ultraviolet photoelectron spectroscopy (UPS) and X-ray photoelectron spectroscopy (XPS). The basic principle is the same: the sample is excited by irradiation with monochromatic light with the energy  $h\nu$  and photoelectrons ( $e^-$ ) are produced via the photoelectric effect. The kinetic energy of these electrons is measured with a spectrometer.

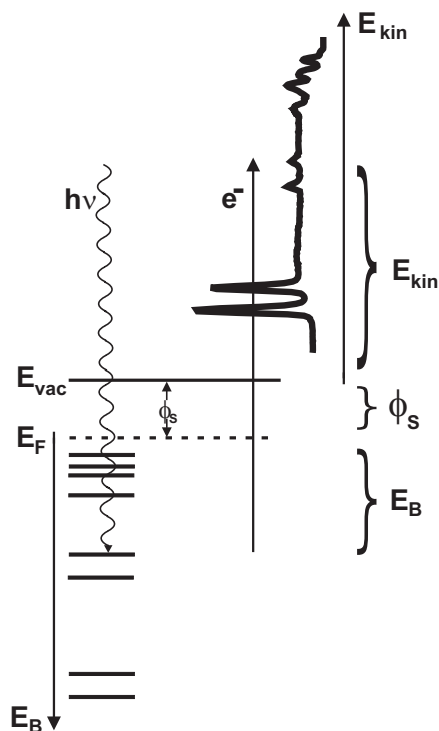


Figure 2.9: Energy level diagram of PES, the left side symbolizes the molecular energy levels of an organic semiconductor, the right side the corresponding photoemission spectrum.  $h\nu$  means photon energy of the exciting radiation,  $e^-$  excited electron,  $E_{vac}$  the vacuum level,  $E_F$  the Fermi level,  $E_B$  binding energy,  $E_{kin}$  kinetic energy and  $\phi_S$  sample work function.

The information depth of PES is determined by the elastic mean free path of the photoelectrons, which depends on their kinetic energy. In this work excitation energies of  $h\nu$  of about 20 eV for UPS and in the range from 400 eV to 1500 eV for XPS have been used. This corresponds to an information depth of about one molecular layer in organic thin film samples for UPS and a few layers for XPS. Thus PES and especially UPS is a very surface sensitive technique. Via the investigation of thickness series of organic thin films on metal substrates, i.e. a step by step deposition of the organic layer, the electronic structure at the organic/metal interface as well as in the bulk of the organic layer can be monitored and coverage dependent energy level diagrams can be derived.

Figure 2.9 displays an energetic diagram of the PES process. The energy of an exciting photon is transferred to an electron. If the photoelectron leaves the sample without elastic scattering, the energy of the exciting photon  $h\nu$  is divided into three parts:

$$h\nu = E_{kin} + \phi_S + E_B \quad (2.8)$$

( $E_{kin}$ : kinetic energy of the photoelectron,  $\phi_S$ : sample work function,  $E_B$ : binding energy). For practical data analysis the position of  $E_F$  of a metal substrate serves as reference for  $E_B$  and  $\phi$  does not have to be known, for a calculation of the binding energy.

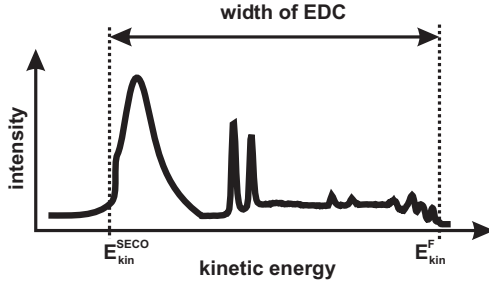


Figure 2.10: Energy distribution curve (EDC) with the SECO ( $E_{kin}^{SECO}$ ) and the Fermi-level ( $E_{kin}^F$ ) marked.

In the low kinetic energy region close to zero kinetic energy secondary electrons are emitted, which have been already elastically scattered in the solid on their way to the sample surface. During the scattering processes these electrons have lost the information about their initial state. With decreasing kinetic energy the intensity of the secondary electrons is increasing but at a certain value the kinetic energy is not sufficient to overcome the work function of the sample and the intensity drops to zero [Fig. 2.10]. This secondary electron cutoff (SECO) allows the sample work function ( $\phi_S$ ) to be determined.  $\phi_S$  is the difference of the photon energy ( $h\nu$ ) and the width of the energy distribution curve (EDC) [Fig. 2.10]:

$$\phi_S = h\nu - (E_{kin}^F - E_{kin}^{SECO}) \quad (2.9)$$

( $E_{kin}^F$ : kinetic energy of electrons excited from the Fermi-level,  $E_{kin}^{SECO}$ : kinetic energy of the SECO).

The sample work function is the energy difference between  $E_F$  and  $E_{vac}$  [Fig. 2.11 (a)].  $E_{vac}$  is essentially constant in close proximity to the surface, but can vary significantly for differently terminated surfaces. In general, a surface has an inhomogeneous distribution of positive (atomic nuclei) and negative (electrons) charges along the surface normal, forming a surface dipole layer that contributes to  $E_{vac}$  [19, 97, 101]. In Fig. 2.11 (b) the impact of such a dipole with length  $L$  on the potential  $\Xi$  is shown. For very small distances from the surface  $x \ll L$ , the dipole layer can be regarded as infinitely extended and  $\Xi$  is independent of  $x$ . For larger distances  $x \gg L$  the dipole layer can be regarded as a point dipole and the potential is proportional to  $x^{-2}$  [19, 101]. Obviously, in an usual PES experiment sample and spectrometer have a macroscopic distance and it would be expected that the surface dipole does not contribute to the measured work function. However, sample and spectrometer are electrically connected [Fig. 2.11 (a)] and the total energy of the photoelectrons is conserved in vacuum. Thus, irrespective of the



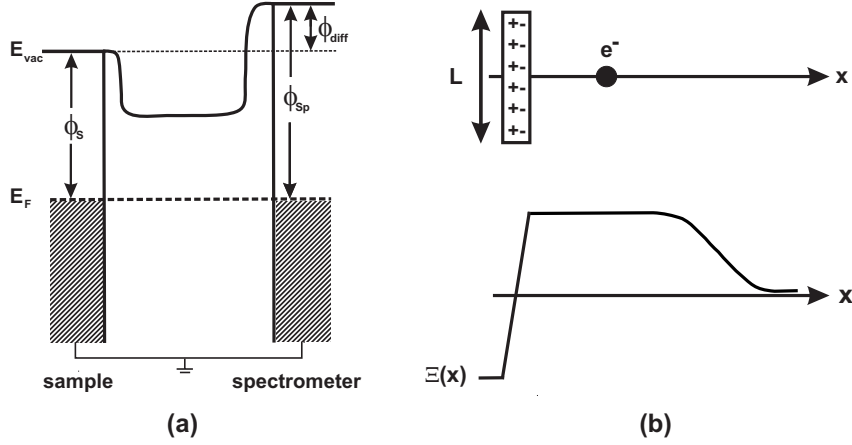


Figure 2.11: (a) Energy level scheme of electrically connected sample and spectrometer: sample work function ( $\phi_S$ ), spectrometer work function ( $\phi_{Sp}$ ) and their difference ( $\phi_{diff}$ ). (b) Impact of a surface dipole layer with length  $L$  on the potential ( $\Xi$ ).  $e^-$  marks the position, where the kinetic energy of the photoelectron is measured.

developing of the vacuum level between sample and spectrometer, the kinetic energy of the photoelectron equal to the moment after just having left the sample is measured [Fig. 2.11 (b)] [19, 97, 101]. The spectrometer itself also has a work function ( $\phi_{Sp}$ ). In most experimental setups  $\phi_{Sp}$  is larger than  $\phi_S$  of a common organic thin film sample<sup>2</sup>, hence  $\phi_{diff}$  is a barrier for the photoelectrons, which cannot be overcome by electrons in the SECO region [Fig. 2.11 (a)]. To allow these low energy electrons to overcome  $\phi_{diff}$ , usually a negative bias voltage ( $V_{bias}$ ) is applied to the sample. Then the position of the SECO is given by:

$$E_{kin}^{SECO} = \underbrace{\phi_S - \phi_{Sp}}_{\phi_{diff}} + qV_{bias} \quad (2.10)$$

( $q$ : elementary charge), and the position of  $E_{kin}^F$  is determined by the photon energy and the spectrometer work function:

$$E_{kin}^F = h\nu - \phi_{Sp} + qV_{bias}. \quad (2.11)$$

The combination of these two equations leads to Equ. 2.9.

It should be noted that PES cannot measure the electronic structure of an undisturbed sample, since the photo-hole itself interacts with the the

<sup>2</sup> $\phi_{Sp}$  does not denote a classical metal work function, but the effective work function of the whole spectrometer depending on parameters like lens voltages or pass energy.

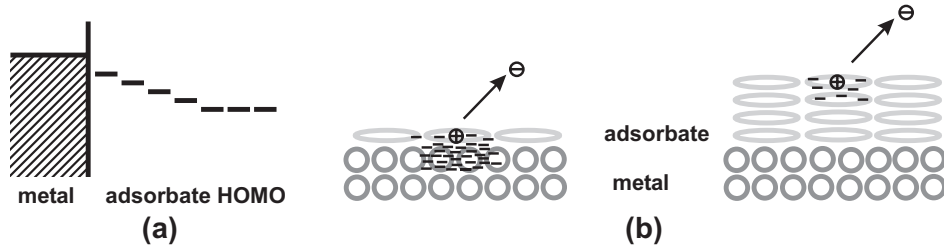


Figure 2.12: (a) Schematic energy level diagram of the HOMO level evolution of an organic adsorbate on a metal substrate as function of film thickness. (b) Sketch of the screening effect by the metal substrate on an organic monolayer and multilayer.

electronic structure of the sample, i.e. final and initial state are different. The initial state is a  $N$  electron state and the final state a  $N-1$  electron state. The transition probability  $w$  for the photoexcitation of an electron is given in the first Born approximation by Fermi's Golden Rule [98, 100]:

$$w \propto \frac{2\pi}{\hbar} |\langle \Psi_f | H | \Psi_i \rangle|^2 \delta(E_f - E_i - h\nu), \quad (2.12)$$

in this equation  $\Psi_f$  corresponds to the final and  $\Psi_i$  to the initial state wave function,  $H$  is the Hamiltonian and  $E_f$  and  $E_i$  are the energies of final and initial states, respectively. Even in the simplest approximation –a one electron view for initial and final state wave functions– the transfer integral can just be calculated to

$$\langle \Psi_f | H | \Psi_i \rangle = \langle \phi_{f,Ekin} | H | \phi_{i,k} \rangle \langle \Psi_{f,R}^k(N-1) | \Psi_{i,R}^k(N-1) \rangle. \quad (2.13)$$

In this equation  $\phi_{f,Ekin}$  means the wave function of the photoemitted electron,  $\phi_{i,k}$  the wave function of the orbital from which the electron is excited and  $\Psi_{i,R}^k(N-1)$  and  $\Psi_{f,R}^k(N-1)$  the wave functions of remaining initial and final state electrons, respectively. This simplified equation can only be solved using *Koopmans' theorem* [98, 100], which neglects the impact of the photo-hole on the wave function of the remaining electrons. With this approximation the overlap integral in Eq. 2.13 becomes unity and the transition matrix element simplifies to a one-electron matrix element. Only in this case the measured binding energy corresponds to the binding energy of the undisturbed system.

In this context, the effect of the screening of the photo-hole by the surrounding matter has to be closer considered, since it is a commonly observed phenomenon in PES, in particular for organic thin films on metal substrates. The ejected electron is slowed down by the Coulomb attraction of the remaining photo-hole, leading to a decrease of the measured kinetic energy.

This decrease of  $E_{kin}$  is reduced by the screening of the photo-hole by the polarization of the surrounding matter (i.e. the higher the polarization, the higher  $E_{kin}$ ). It was found that in general the energy levels of multilayers occur at higher binding energies than the energy levels of (sub-)monolayers [Fig. 2.12 (a)]; the differences are up to 0.4 eV [18, 19, 102]. This was explained by a higher polarizability of metals compared to the polarizability of COMs [18, 19, 102]. In the case of a (sub-)monolayer of a COM on a metal surface the screening is mainly facilitated by the metal of the half space underneath the adsorbate. For increasing coverage of the organic film the influence of the metal substrate decreases [Fig. 2.12 (b)].

### Ultraviolet Photoelectron Spectroscopy

The onset of the photoelectron emission of organic thin film samples in the high kinetic energy region due to emission from the HOMO allows the determination of the hole injection barriers. In the valence electron region the density of occupied states is probed and molecular levels can be assigned. The SECO in the low kinetic energy region is used to determine the position of  $E_{vac}$ , which allows to derive the sample work function. With  $\Delta_h$  and  $\phi$ , the ionization energy can be calculated as the sum of these two values. Thus, UPS is the experimental method of choice for tracking the energy levels at organic/metal interfaces as a function of the film thickness.

In addition to the energetic position of spectral features, also their shape contains precious information. As an example, a high resolution UPS spectrum of the HOMO region of a pentacene (PEN) monolayer on Au(111) is shown in Fig. 2.13. The HOMO peak can be fitted well with four Voigt peaks, which correspond to the HOMO and its first three vibrational progressions of PEN on Au(111) [103]. The interaction strength of the hole-vibrational coupling is given by the Huang-Rhys factor  $S$  [53, 103–105], which can be calculated from the intensity of the vibrational progressions:

$$I_n = \frac{S^n}{n!} e^{-S} \quad (2.14)$$

where  $I_n$  is the intensity of the  $n$ -th vibrational band [104]. With  $S$  and the energy of the vibrational modes  $h\nu$ , which couples strongly to the photoemission process, the charge reorganization  $\lambda$  can be calculated:

$$\lambda = \sum_m S_m h\nu_m \quad (2.15)$$

where  $\nu_m$  is the vibrational frequency of the  $m$ -th vibrational mode [104].  $\lambda$  corresponds to the sum of the relaxation energy which is necessary for

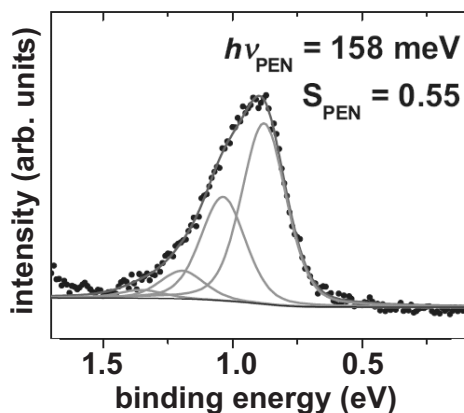


Figure 2.13: UPS HOMO region for a monolayer of PEN on Au(111). Dots are experimental points; grey lines correspond to results from fitting with four Voigt functions. For details see text. This plot is taken from Ref. [103].

the conformational transition of the molecule from the neutral state to the charged state. In addition to this molecular information that is contained in UPS spectra, information about intermolecular and adsorbate-substrate interaction can be obtained by comparing spectra of adsorbed molecules with their gas-phase spectra, since strong interactions may lead to a further broadening of the spectral features. However, in all cases the low binding energy *onset* of the HOMO peak is the crucial parameter for the transport properties of the organic thin film, because this onset represents the manifold of available charge transport states.

Since UPS is a surface sensitive method it can also provide information on the growth mode. Depending on the growth mode the suppression of substrate features, like emission from the metal Fermi-edge or metal bands occurs at different nominal coverages. Substrate features are rapidly suppressed for low molecular coverages if molecules grow in the Volmer-Weber mode. Depending on the dimension of the molecule and the orientation on the substrate one or two nominal layers are usually enough to suppress substrate features totally. For Frank-van der Merve or Stranski-Krastanov growth mode however twenty or more nominal layers are not even capable to totally suppress substrate features. Also XPS can be used to probe the growth mode in a similar way by investigating the substrate core level intensities. However, due to the larger information depth in XPS, the coverage, which is necessary to suppress substrate features, is higher.

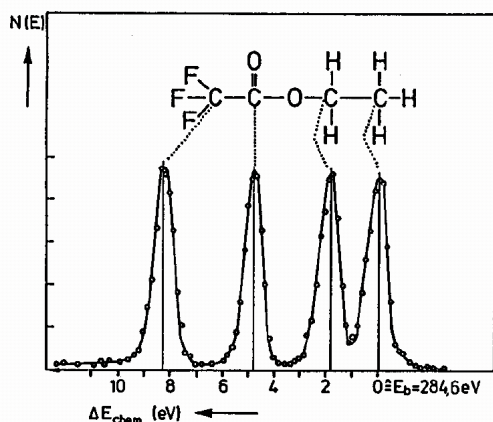


Figure 2.14: XPS spectrum of the C(1s) peak of ethylfluoroacetate. This plot (taken from Ref. [36]) demonstrates the influence of the chemical environment on the binding energy of core levels.

### X-ray Photoelectron Spectroscopy

With XPS the atomic core levels can be investigated. A wide range XPS spectrum contains information about the elements which are present in the sample. Taking different atomic cross sections for photoemission into account, the intensity ratio of peaks derived from different elements gives the elemental composition of the sample. Thus, XPS can be used to identify contaminations on pristine substrates and impurities in adsorbed molecules. XPS can also be used to check whether molecules have been adsorbed intact, because often damage (due to heating during evaporation) leads to a decomposition of the molecule and the elemental ratio of the adsorbate is changed.

The binding energy of core levels depends significantly on the bonding of the respective atom to neighboring atoms in the molecule. These *chemical shifts* of core levels can be in the range of up to 10 eV [Fig. 2.14]. A close inspection of core levels can therefore be useful to obtain information on atoms in different chemical environments. This again is a good tool to test if the investigated molecules adsorb intact. Chemical reactions with the surface can lead to additional shifts in the core level spectra.

Commonly observed additional features in XPS are *shake-up* and *shake-off* lines [36, 100]. These additional lines result from two-electron processes where a valence electron is excited by the emission of a core level photoelectron. The valence electron can either be emitted as well (shake-off) or stay in the solid (shake-up) [Fig. 2.15]. In organic thin films shake-ups and

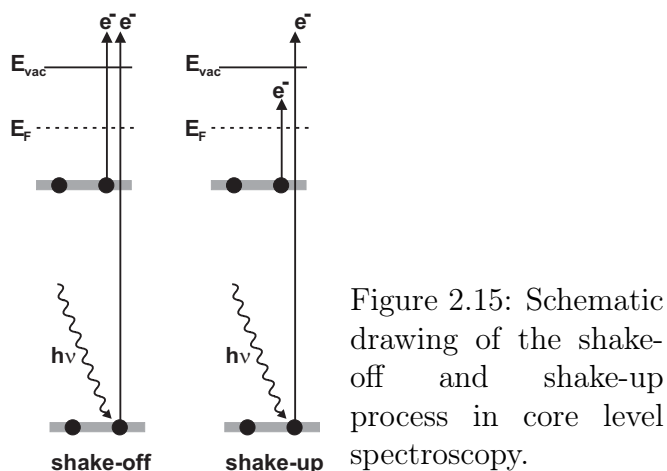


Figure 2.15: Schematic drawing of the shake-off and shake-up process in core level spectroscopy.

shake-offs lead to broad peaks shifted by several eV in binding energy with respect to the original peak.

## 2.2.2 Metastable atom electron spectroscopy

Metastable atom electron spectroscopy (MAES) [106, 107] is closely related to UPS. The sample is excited and the kinetic energy distribution of emitted electrons is measured. In contrast to UPS, the excitation of the sample occurs via metastable atoms, mostly  $\text{He}^*$ . In UPS the limiting factor for the information depth is the elastic mean free path of the photoelectrons. MAES is even more surface sensitive than UPS, since  $\text{He}^*$  atoms do not penetrate the surface and therefore only the outermost orbitals of the adsorbed molecules are probed. Obviously, for different orientations of molecules forming the adsorbed film, different molecular orbitals are exposed on the surface of the film. In Fig. 2.16 the situation of  $\text{He}^*$  atoms approaching an organic thin film is sketched for two different molecular orientations. If quantum chemical calculations allow to assign the spectral features to molecular orbitals located on different parts of the molecule, the molecular orientation can be determined. Therefore, MAES is the technique of choice to gain both, information about the electronic structure *and* molecular orientation in one experiment.

Metastable atoms are usually produced by electron bombardment or cold or hot cathode discharge type sources. In this processes both, singlet  $\text{He}^*(2^1\text{S})$  and triplet  $\text{He}^*(2^3\text{S})$  are produced.  $\text{He}^*(2^1\text{S})$  can be experimentally suppressed by the use of a quenching lamp to get rid of satellites in the resulting MAES spectrum.  $\text{He}^*(2^3\text{S})$  atoms have thermal velocity and are deexcited when reaching the sample surface. Depending on the elec-

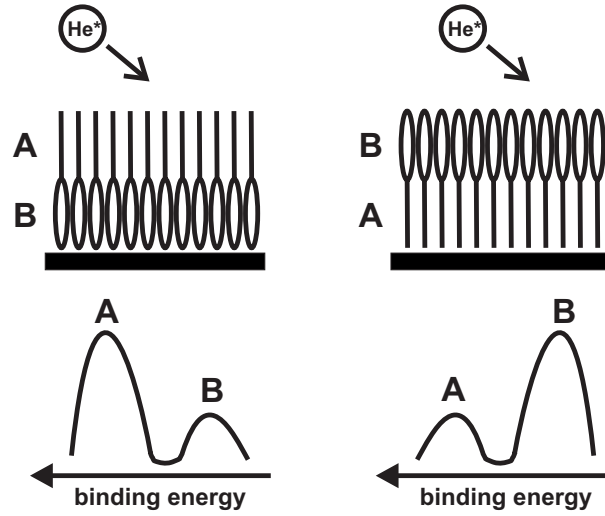
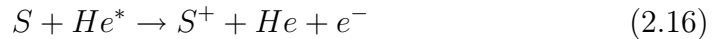


Figure 2.16: Organic thin films with two different orientations and corresponding MAES spectra. In the spectra the emission corresponding to molecular orbitals located in the part of the film near to the surface dominates.

tronic structure of the sample, different deexcitation channels of  $\text{He}^*(2^3\text{S})$  are possible. For organic thin film samples without a continuous density of unoccupied states above  $E_F$  the dominating process is penning ionization of the molecules [Fig. 2.17 (a)]. The underlying process of penning ionization is:



where S means sample. An electron from an occupied molecular orbital of the sample is transferred to the 1s level of the  $\text{He}^*$  atom. Simultaneously, the electron from the 2s level in  $\text{He}^*$  is ejected. Since this is a single electron process in the sample, the resulting spectrum corresponds to the occupied states in the detected region. For metal samples, i.e. for samples with a continuous density of unoccupied states above  $E_F$ , the situation is different: The dominating deexcitation process is resonance ionization:



followed by Auger neutralization:

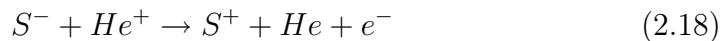


[Fig. 2.17 (b)]. An electron can resonantly tunnel from the excited  $\text{He}^*$  2s level into an empty state in the sample. The now positively charged sample is

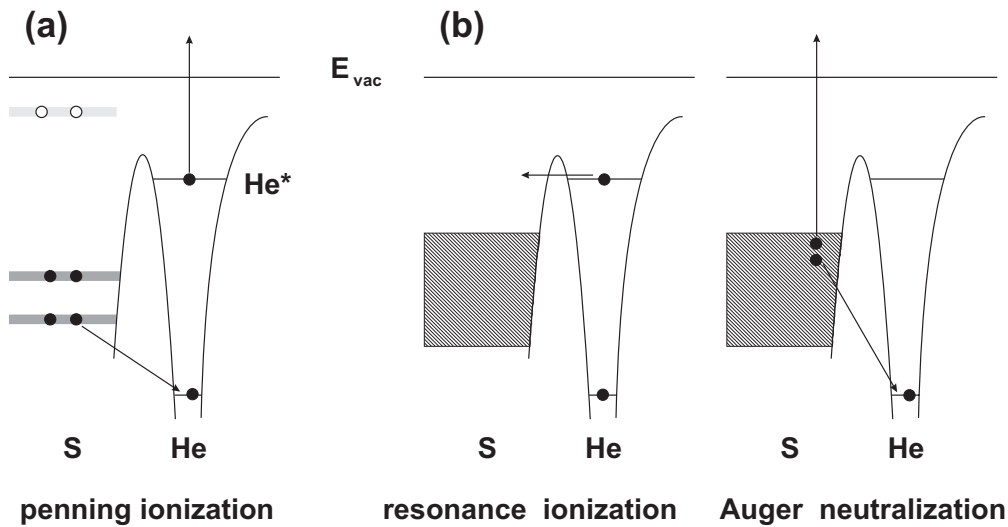


Figure 2.17: Deexcitation modes of metastable atoms in contact with a solid surfaces. (a) Semiconducting sample and (b) metal sample.

then neutralized by an Auger process. In this process an electron in the metal fills the vacant position in the  $\text{He}^*$  1s level and a further electron is ejected from the metal. The spectrum of this multi-electron process is smeared out and contains only little structure.

### 2.2.3 X-ray diffraction

X-ray diffraction (XRD) is a technique, which is widely used in many fields of science and is well documented in literature [108–110]. However, a brief description of XRD is given in the following.

In XRD measurements the diffraction of X-ray radiation at the crystal net-planes is used. The Bragg-equation:

$$n\lambda = 2d_{hkl} \sin(\Theta_B) \quad (2.19)$$

relates the lattice spacing ( $d_{hkl}$ ) of a set of net planes with Miller indices ( $hkl$ ) to the scattering angle ( $\Theta_B$ ) for a certain X-ray wavelength ( $\lambda$ ). Depending on the measurement geometry the structural order of thin organic films perpendicular and parallel to the film surface can be investigated with XRD [Fig. 2.18]. Specular XRD, usually referred to as X-ray reflectivity (XRR) for small diffraction angles, allows to determine the out-of-plane lattice spacings and grazing incidence diffraction (GID) the in-plane lattice spacings. The investigation of interference phenomena (Kiessig fringes) [111], due to differences in the electron densities of stacked layers, at low scattering angles in



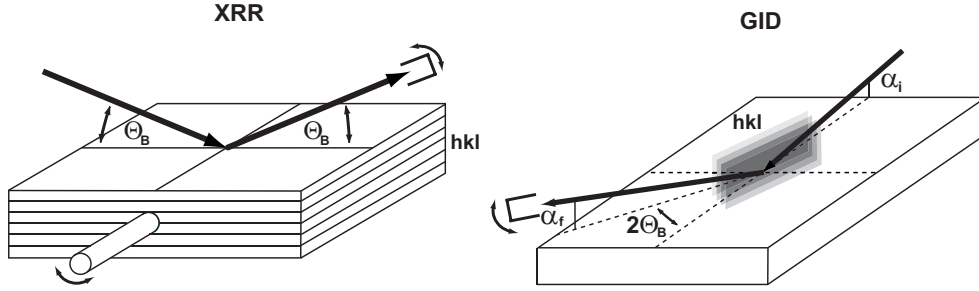


Figure 2.18: Geometry for X-ray reflectivity (XRR) and grazing incidence diffraction (GID) measurements. In XRR both, the sample and the detector are rotated, in GID the rotation of the sample is not necessary, if fibre textured structures are measured.  $\alpha_i$  denotes the incident angle of the primary beam and  $\alpha_f$  the exit angle above the sample plane in the GID geometry.

specular XRD allows to accurately determine film thicknesses and interface roughnesses.

#### 2.2.4 X-ray standing waves

X-ray standing waves (XSW) [112–114] is a technique based on a combination of a diffraction approach with a spectroscopic method. XSW is a powerful tool to obtain molecular bonding distances on a single crystalline substrate. The basic principle is to measure XPS spectra of organic monolayers with an X-ray standing wave produced by Bragg-reflection [Equ. 2.19] on a single crystalline substrate. By slightly varying the excitation photon energy the nodes and antinodes of the standing wave map the space parallel to the substrate surface. The intensity of excitation energy dependent XPS signals is varied depending on the bonding distance of the atom [Fig. 2.19]. With this technique bonding distances with an accuracy as good as  $0.1 \text{ \AA}$  can be determined [93].

The normalized spatial intensity of the XSW field  $I^{SW}(\vec{r})$  is given by the superposition of the incoming plane wave with the electrical field vector ( $\vec{E}_0$ ) and the Bragg-reflected wave ( $\vec{E}_H$ ):

$$I^{SW}(\vec{r}) = \frac{|\vec{E}_0 + \vec{E}_H|^2}{|E_0|^2} = 1 + R + 2C\sqrt{R}\cos(\nu - 2\pi\vec{H} \cdot \vec{r}) \quad (2.20)$$

( $R = |E_H/E_0|^2$ : reflectivity;  $\nu$ : phase of the complex amplitude ratio:  $E_H/E_0 = \sqrt{R}\exp(i\nu)$ ;  $\vec{H}$ : reciprocal lattice vector; C: polarization factor). The C factor equals 1 for  $\sigma$ -polarization and  $\cos(2\Theta_B)$  for  $\pi$ -polarization. R

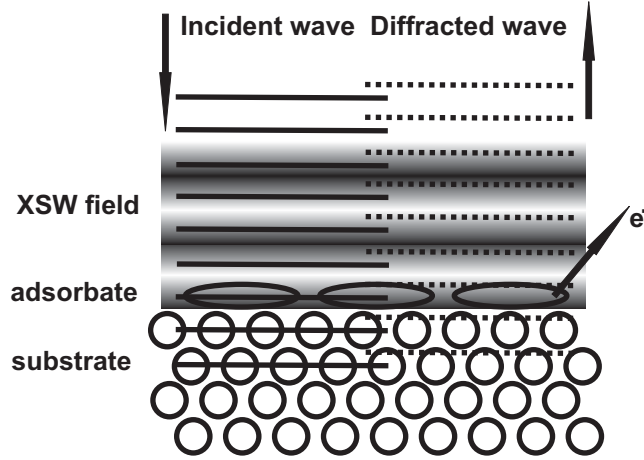


Figure 2.19: Principle of the XSW technique. The XSW field is the coherent superposition of incident and diffracted wave. Bright parts correspond to the antinodes and dark parts to the nodes of the standing X-ray wave in which the XPS intensity ( $e^-$ ) of the adsorbate is measured.

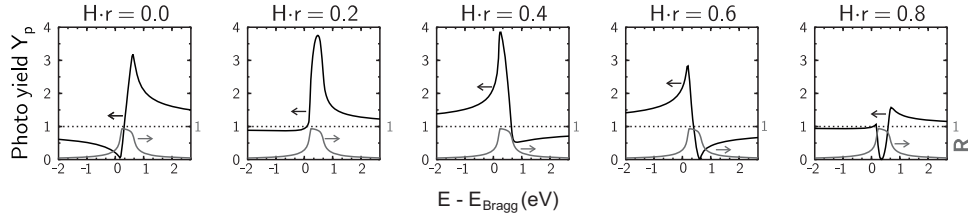


Figure 2.20: XSW yield  $Y_p$  and reflectivity  $R$  as function of excitation energy relative to the Bragg energy ( $E_{Bragg}$ ) for different coherent adsorption positions  $\vec{H} \cdot \vec{r}$ . This figure is taken from Ref. [112].

and  $\nu$  can be calculated in the framework of the dynamical diffraction theory [112]. The XSW field is used as excitation source for photoemission of the adsorbate, i.e. the XPS signal of the adsorbate is measured in  $I^{SW}$ . In the dipole approximation the yield of a spectroscopic signal ( $Y_p$ ) of an adsorbate is proportional to the electric field at the center of the atoms and thus proportional to  $I^{SW}$ . This proportionality is only valid in the ideal coherent case, i.e. all atoms of the adsorbate have the same adsorption position. The effect of different adsorption positions on  $Y_p$  is illustrated in Fig. 2.20. The signal of the reflectivity  $R$  solely originates from the metal substrate. In an experiment the mean half width of  $R$  provides information about the crystal quality and mosaicity.  $Y_p$  only depends on the coherent position of the adsorbate, which is expressed in terms of fractions of the reciprocal lattice

vector  $\vec{H}$  of the substrate in Fig. 2.20. In order to obtain a  $Y_p$  curve, the XPS intensity at several photon energies close to the Bragg energy ( $E-E_{Bragg}$ ) has to be measured.

Practically, no system reaches perfect coherence and a normalized distribution function  $n(\vec{r})$  describing the spread of atoms around their average position has to be introduced:

$$Y_p = \int Y_p(\vec{r})n(\vec{r})d\vec{r} = 1 + R + 2C\sqrt{R} \int n(\vec{r}) \cos(\nu - 2\pi\vec{H} \cdot \vec{r})d\vec{r}. \quad (2.21)$$

In usual this equation is rewritten by the introduction of two parameters, the coherent position  $P_H = \vec{H} \cdot \vec{r}$  and the coherent fraction  $f_H$ :

$$Y_p = 1 + R + 2C\sqrt{R}f_H \cos(\nu - 2\pi P_H). \quad (2.22)$$

Both values ( $P_H$  and  $f_H$ ) range between 0 and 1 and contain the information of interest in an XSW experiment.  $P_H$  gives the position of the adsorbate atoms in fractions of  $\vec{H}$  and  $f_H$  provides information about the structural order of the adsorbate.  $f_H = 0$  corresponds to a totally disordered system with randomly distributed atoms and  $f_H = 1$  to a perfectly ordered adlayer with all atoms having the same bonding distance to the substrate surface atoms.

# Chapter 3

## Materials and Experimental Setups

In the following chapter the investigated molecules and the used substrates are introduced and experimental details are given.

### 3.1 Materials

This section motivates the choice of the specific investigated organic molecules and the substrates; their properties necessary for the understanding of the experimental results are given in Chapter 4. For detailed information literature citations are provided.

#### 3.1.1 Organic Adsorbates

An overview of the chemical structures of the investigated molecules is given in Fig. 3.1. In Table 3.1 the acronyms of the compound names are given together with references to the synthesis or to the suppliers. In order to clarify organic/metal interface properties with its complex correlation of various physical properties it is necessary to investigate several different molecules, well chosen due to their distinct physical properties. Ideally, the molecules combine application relevant properties with properties helpful to test novel concepts of fundamental physics.

In order to investigate the interplay of molecular orientation and electronic structure it is necessary to study molecules which exhibit a different electronic structure for different orientations. In addition, an orientational transition on metal substrates should occur at a thickness scale of a few organic layers. 6T and its hexyl chain substituted derivative DH6T have been

acronym	compound name	source
6T	$\alpha$ -sexithiophene	Aldrich
DH6T	$\alpha,\omega$ -dihexylsexithiophene	H. C. Starck
F4-TCNQ	2,3,5,6-tetrafluoro- 7,7,8,8-tetracyanoquinodimethane	Fluka
FAQ	octafluoroanthraquinone	[124]
TCAQ	11,11,12,12-tetracyano- 9,10-anthraquinodimethane	[125]
PEN	pentacene	Aldrich
PFP	perfluoropentacene	[7]
PTCDA	3,4,9,10-perylene tetracarboxylic dianhydride	Aldrich
6P	p-sexiphenyl	TCI Europe
$\alpha$ -NPD	N,N'-bis-(1-naphthyl)-N,N'-diphenyl- 1,1-biphenyl-4,4'-diamine	Aldrich
TTC	tetratetracontane	Fluka

Table 3.1: Overview of investigated molecules.

chosen for this purpose. The organic semiconductor 6T is widely investigated and can exhibit good device performance as active material in OFETs [115–118]. It can be regarded as a prototype for a rodlike COM. It has been reported that the addition of hexyl chains enhances charge carrier mobilities and the on/off current ratio in OFETs [119–122]. As functional side groups can significantly influence the growth behavior [79, 83, 121, 123], the increase in device performance may be correlated with a change in the molecular orientation of thin films based on DH6T. Therefore, these molecules are perfect candidates for a fundamental study on the interplay of electronic structure and molecular orientation.

For energy level tuning strong electron accepting molecules are necessary. One of the strongest known organic electron acceptors is F4-TCNQ [63–65] and therefore an appropriate candidate to undergo a CT with noble metals. The acceptors FAQ and TCAQ have the advantage of higher molecular weight compared to F4-TCNQ. This may lead to easier handling in device processing.

Regarding the correlation of bonding distance and interfacial electronic structure, weak and strong interacting systems are expected to exhibit pronounced differences. Therefore, in order to find resilient correlations between the interfacial electronic structure and the bonding distance, it is necessary to study at least two systems. PTCDA was chosen as a prototype of a strong reactive molecule, which adsorbs structurally well defined on a vari-

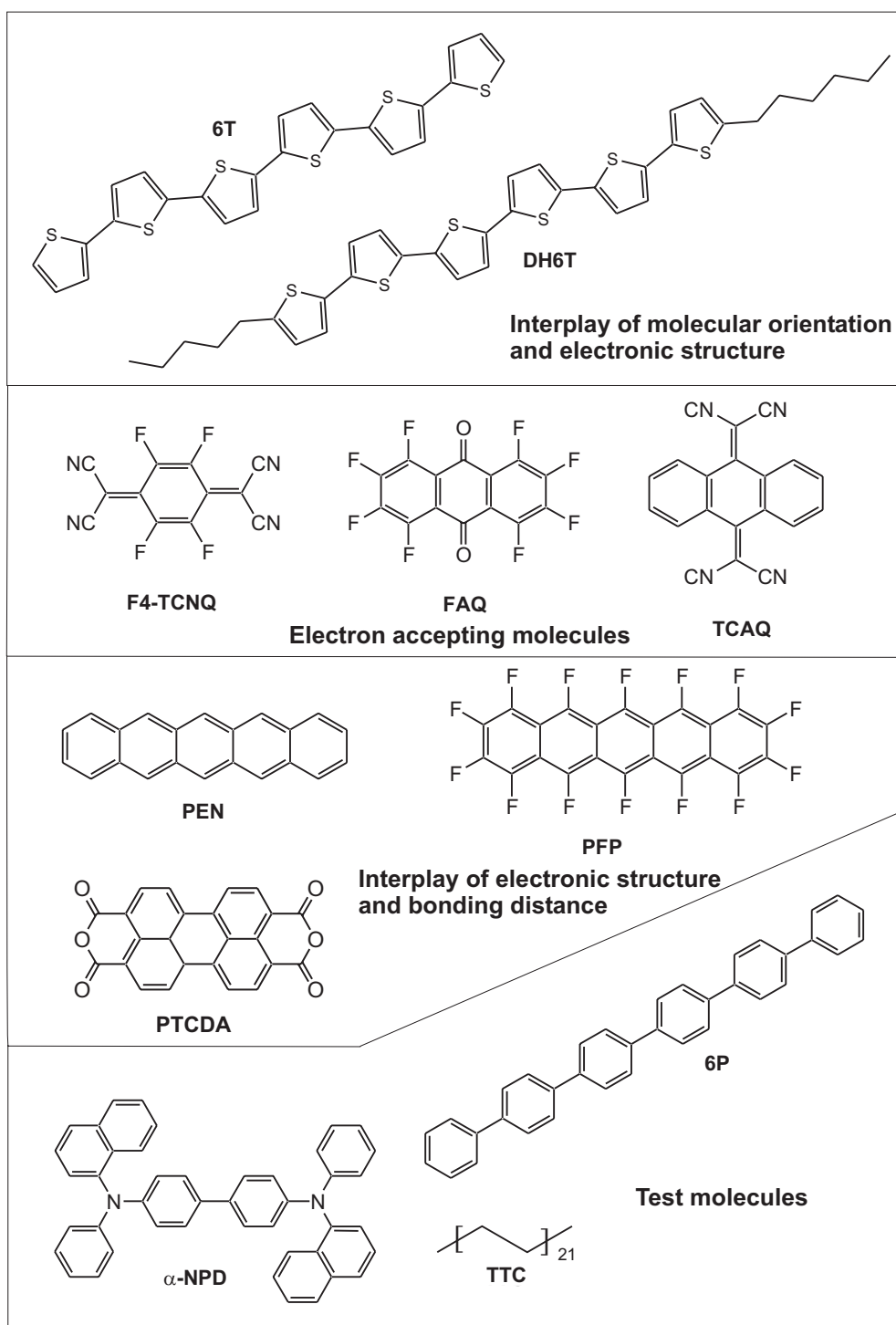


Figure 3.1: Chemical structure of the investigated molecules, for more details see Table 3.1.

ety of metal substrates [47–49]. PFP, in contrast, is only weakly bound on metal substrates [103] and can therefore act as complement to PTCDA as a prototype for a weakly interacting system. Moreover, the fluorination of PEN, another important material in organic electronics [126–129], leads to an increase in device performance of n-type OFETs [7, 130].

In some experiments additional molecules have been necessary. Obviously, the concept of energy level tuning with acceptors requires COMs which are deposited on top of the acceptor pre-covered metal substrates. For this purpose  $\alpha$ -NPD, which forms amorphous films on a variety of substrates [18, 67] and 6P, a COM with a high IE [60, 131], were used. In order to study the mechanisms of organic thin film growth it is helpful to alter the substrate properties in a defined way. TTC (a long alkyl chain) forms highly ordered monolayers on various metal substrates [132–134] and was chosen to pre-pattern metal surfaces.

### 3.1.2 Substrates

Experiments have been performed on a variety of different substrates. As model systems the metal single crystals Ag(111), Au(111), and Cu(111) were chosen, since they are structurally well defined. The (111)-orientation was chosen because of its stability and its wide spread use in experiments. These three metals cover a wide range of surface reactivity and work functions, which are properties that have strong influence on both, the molecular orientation and the electronic structure of adsorbed COMs. To investigate molecules in an application relevant context also polycrystalline Au was chosen as substrate, since it is a commonly used electrode in the field of organic electronics. To study the influence of substrate/adsorbate interaction strength on the molecular orientation highly oriented pyrolytic graphite (HOPG), a semimetal, was chosen as additional substrate.

## 3.2 Experimental Setups and Data Analysis

In this section the experimental setups used within this work and the experimental procedures are described.

### Organic thin film preparation

Sample preparation and measurements were done as follows: The single crystals were cleaned by repeated Ar-ion ( $E_{kin} = 600$  eV) sputtering and annealing cycles (up to 550 °C) until a clear low electron energy diffraction (LEED)

pattern was observed. The polycrystalline Au substrates were evaporated *in-situ* onto a Cu-foil with a thickness of at least 400 Å. Afterwards they were Ar-ion sputtered. HOPG (ZYA grade) was cleaved in air just before loading into the preparation chamber and cleaned by *in-situ* heating at 400 °C for 15 h. Molecules were evaporated using resistively heated pinhole sources (consisting of ca. 0.5×1 cm large bags, made of 0.025 mm thick Ta-foil), at evaporation rates of about 1 Å/min. The film mass-thickness was monitored with a quartz crystal microbalance (QCM). No corrections were made for possible different sticking coefficients on the microbalance and the substrate. The mass density of all molecules was estimated to 1.35 g/cm<sup>3</sup>. The low sublimation temperatures of the used molecules (ranging from 80 °C to 350 °C), the low evaporation rates and the material saving design of the evaporation sources let the pressure during evaporation remain low (typically about  $5 \times 10^{-9}$  mbar). All preparation steps and measurements were performed with the substrate at room temperature and under ultrahigh vacuum (UHV) conditions.

## UPS at HASYLAB

Unless explicitly noted, UPS experiments were performed at the FLIPPER II end-station at the synchrotron radiation source HASYLAB (Hamburg, Germany) [135]. The experimental setup is shown in Fig. 3.2; it consisted of four interconnected UHV chambers, which allowed sample transfer without breaking UHV conditions. All chambers could be separated from each other by valves and could be pumped separately. Organic chambers I and II (base pressure  $2 \times 10^{-9}$  mbar) were each equipped with a QCM mounted on a linear feedtrough and a flange for organic evaporators. The two separated organic evaporation chambers allowed to prepare organic/organic heterostructures without cross-contamination during evaporation. The preparation chamber (base pressure  $1 \times 10^{-10}$  mbar) was equipped with a heatable manipulator, an ion source for sputtering, a QCM and three metal evaporators. In the analysis chamber (base pressure  $2 \times 10^{-10}$  mbar) the electron analyzer and a LEED system were mounted. In addition, the end-station provided a sample magazine for the storage of up to eight samples and a fast entry load lock.

Spectra were recorded with a double-pass cylindrical mirror analyzer with the energy resolution set to 150 meV (measured as 80% to 20% intensity drop at a metal Fermi-edge). The photon energy was 22 eV unless otherwise noted. The angle between incident synchrotron radiation and the analyzer entrance was fixed to 90°, spectra were recorded angle-integrated (analyzer acceptance angle 12° - 24° and 56° - 68°) with the angle between detector and surface normal of the sample set to 50°. The SECOs (for determination of  $\phi$  and



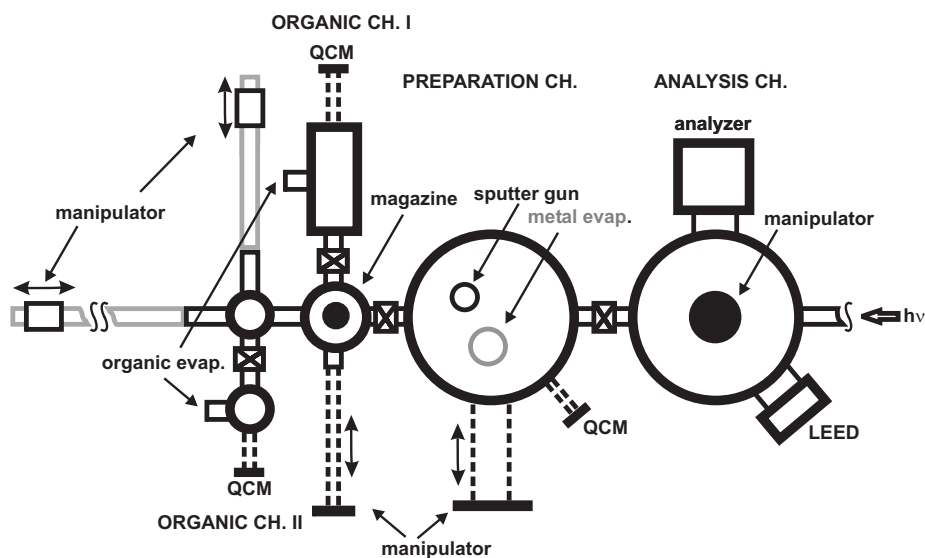


Figure 3.2: Top view of the FLIPPER II end-station at HASYLAB. For better clearness fast entry load lock, pumping systems and less important details are not included. “CH.” stands for chamber, “evp.” for evaporator and “QCM” for quartz crystal microbalance.

IE) were measured with the sample biased at voltages ranging from  $-3.00\text{ V}$  to  $-7.00\text{ V}$ . To avoid sample charging during the photoemission experiments on multilayer DH6T films, these spectra were recorded with an Al-foil in the photon beam, reducing the photon flux by a factor of seven.

### UPS and XPS at BESSY

Most of the XPS experiments and some of the UPS experiments were performed at the end-station SurICat (beamline PM4) at the synchrotron light source BESSY (Berlin, Germany) [136]. The UHV system consists of interconnected sample preparation (base pressure:  $5 \times 10^{-9}\text{ mbar}$ ) and analysis (base pressure:  $1 \times 10^{-10}\text{ mbar}$ ) chambers. The spectra were collected with a hemispherical electron energy analyzer (Scienta SES 100) with 120 meV energy resolution. Excitation energies were 400 eV and 630 eV for XPS and 32 eV for UPS experiments.

### MAES and UPS at Chiba University

MAES and some of the UPS measurements were performed in the laboratories of Prof. Nobuo Ueno at Chiba University (Japan) [137]. The interconnected sample preparation chambers (base pressure  $3 \times 10^{-10}\text{ mbar}$ )

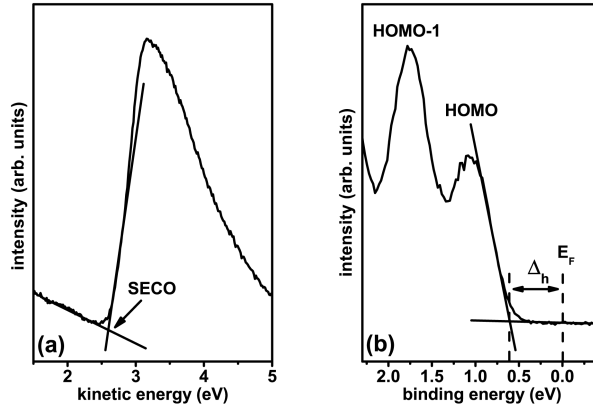


Figure 3.3: Example for fitting routine of (a) the secondary electron cutoff (SECO) and (b) the hole injection barrier ( $\Delta_h$ ).

and analysis chamber (base pressure  $2 \times 10^{-10}$  mbar) allowed sample transfer without breaking UHV conditions. Spectra were recorded with a hemispherical electron energy analyzer (VG-CLAM4). UPS spectra were measured using p-polarized He I radiation, the angle between incident photons and detected photoelectrons was fixed to  $45^\circ$  with an acceptance angle of  $\pm 12^\circ$ . The spectra were measured at photoelectron take-off angles ( $\theta_e$ ) of  $0^\circ$  (normal emission) and  $45^\circ$  (off-normal emission). The energy resolution was set to 70 meV. MAES spectra were recorded using He\* ( $2^3S$ ; 19.82 eV). All spectra were measured with the sample biased at -5.00 V.

### XPS at Humboldt University

Additional XPS measurements were performed at Humboldt University in a custom UHV-system (base pressure preparation chamber:  $3 \times 10^{-9}$  mbar and base pressure analysis chamber:  $1 \times 10^{-10}$  mbar) with a non monochromated Al  $K_\alpha$  source and a hemispherical analyzer (Specs, PHOIBOS-100).

### Data Analysis of spectroscopic results

For analysis of UPS spectra the computer-program *Origin 7.0* was used. The secondary electron cutoff in the low kinetic energy region of the spectra was determined by the intersection of linear fits of the cutoff and the background [Fig. 3.3 (a)]. In the high kinetic energy region the position of the Fermi-level was identified using a metal Fermi-edge. Binding energies ( $E_B$ ) were referred

to  $E_F$ :

$$E_B = E_{kin}^{E_F} - E_{kin} \quad (3.1)$$

( $E_{kin}$ : kinetic energy,  $E_{kin}^{E_F}$ : kinetic energy of  $E_F$ ). In UPS spectra of COMs the hole injection barrier was determined by the difference between  $E_F$  and the onset of the HOMO emission [Fig. 3.3 (b)]. The HOMO onset was determined as intersection of a linear background and linear fit of the low BE side of the HOMO. The ionization energy was calculated as follows:

$$IE = h\nu - (E_{kin}^{\Delta_h} - E_{kin}^{SECO} + qV_{bias}) \quad (3.2)$$

(IE: ionization energy,  $h\nu$ : excitation photon energy,  $E_{kin}^{\Delta_h}$ : kinetic energy of the hole injection barrier,  $E_{kin}^{SECO}$ : kinetic energy of the secondary electron cutoff,  $q$  elementary charge,  $V_{bias}$ : bias voltage). For calculating the work function  $\phi$ ,  $E_{kin}^{\Delta_h}$  must be replaced by  $E_{kin}^{E_F}$  in formula 3.2. If not stated otherwise the error of all given IE and  $\phi$  values is  $\pm 0.05$  eV, estimated as sum of the error for measurements at different sample spots and of the statistical error of reading accuracy. To obtain the pure molecule spectra from spectra still containing substrate contributions, spectra were normalized to the intensity at  $E_F$  and the substrate spectrum was subtracted [102, 138].

The energy calibration of the XPS spectra was done with a metal substrate core level as reference. Data fitting (Voigt peaks and Shirley background) was performed using the program WINSPEC, developed at Namur University (Belgium).

The analysis of MAES data was done using `Origin 7.0` by comparison (i) of the different experimental spectra, (ii) of the experimental spectra to simulated spectra and (iii) of the experimental spectra to spectra taken from literature.

## XRD at HASYLAB

XRR (X-ray reflectivity) and GID (grazing incidence diffraction) measurements have been performed at the beamline W1.1 [139] at HASYLAB under ambient conditions. The wavelength was set to 1.1808 Å. In the GID experiment an incident angle of the primary beam of  $\alpha_i = 0.15^\circ$  was chosen, the exit angle above the sample plane  $\alpha_f$  was set to  $0.5^\circ$ , the acceptance angle defined by the detector slits was less than  $0.3^\circ$ . Films have been prepared at FLIPPER II directly before the measurements. The data analysis was done according to Equ. 2.19 using `Origin 7.0`.

## XSW at ESRF

XSW measurements were done at beamline ID 32 at the European Synchrotron Radiation Facility (ESRF, Grenoble, France) [93]. The UHV system consists of a combined preparation and analysis chamber (base pressure:  $3 \times 10^{-10}$  mbar). XPS spectra were recorded with a hemispherical electron analyzer (Physical Electronics) at an angle of  $45^\circ$  relative to the incoming X-ray beam. X-ray reflectivity was measured with a photodiode mounted at a small angle relative to the incoming beam.

Fitting of XSW spectra was done using the programs `xps2dare` and `dare`, both developed at ESRF, following Equ. 2.22. However, this equation is only valid in the dipole approximation. Since higher order terms contributing to the photoemission yield cannot be neglected for low  $Z$  elements and photon energies of several keV, the values given by the fit for the coherent fraction and position ( $f_{eff}$  and  $p_{eff}$ ) have to be corrected in order to get the corrected values  $f_H$  and  $p_H$ . The correction was done using:

$$f_{eff} = |S_I|f_H \quad \text{and} \quad P_{eff} = P_H - \frac{\Psi}{2\pi} \quad (3.3)$$

( $S_I$  and  $\Psi$ : non-dipolar correction terms:  $f_H$ : coherent fraction and  $P_H$ : coherent position). The values for the correction terms are given in Table 3.2.

	C(1s)	F(1s)
$S_I$	1.382	1.365
$\psi$	-0.055	-0.067

Table 3.2: Non-dipolar correction terms for the C(1s) and F(1s) core levels of an adsorbate on a Cu(111) substrate. These values are taken from Ref. [93].

The bonding distance ( $d_H$ ) was calculated using:

$$d_H = d_0(1 + P_H) \quad (3.4)$$

with  $d_0 = 2.084$  Å being the lattice spacing of Cu(111).

## Calculation of theoretical spectra

The theoretical spectra are the superposition of the Gaussian-broadened energy eigenvalues of molecules, calculated with density functional theory using `Gaussian03` (Program Package `Gaussian03` (B3LYP/6-31 G\*) [140]. Calculations were carried out by Hirohiko Fukagawa (DH6T) or Jürgen Klankermayer (FAQ), respectively.

# Chapter 4

## Results and Discussion

In this chapter the experimental results are described and discussed. First, the molecular orientation of DH6T and 6T is treated in detail. A novel concept of face dependent intramolecular dipoles is presented. In the following part organic/metal charge transfer complexes, which enable energy level tuning are described. The next section deals with energy level alignment mechanisms at organic/metal and organic/organic interfaces. In the last part the interplay of bonding distances and electronic structure at organic/metal interfaces will be discussed.

### 4.1 Molecular Orientation

In this section the impact of the molecular orientation on the electronic structure at organic/metal interfaces is discussed. The focus lies on the impact of alkyl substitution of 6T on thin film growth and electronic structure. Experiments were performed for DH6T on different substrates and on organic heterostructures of DH6T and other organic molecules. Actually, one may not expect significant changes in the organic/metal interface electronic properties due to simple addition of alkyl chains (compared to the unsubstituted oligomer), because of the insulating nature of the saturated alkyls. In fact,  $\beta, \beta'$ -dihexylsexithiophene exhibits essentially the same energetics at interfaces to Au as 6T [141]. However, the growth of molecules may be substantially changed by alkyl chain addition [121, 123]. Consequently, the electronic structure of a molecular film, and also its interface electronic properties depends on different molecular organization [142]. For DH6T on metals the electronic structure changes by an orientational transition from lying monolayer to standing multilayer. In addition, a new concept of an orientation dependent IE in molecular crystals is presented.

Most of the results of this section are published in Refs. [143] (lying monolayer/standing multilayer), [144] (orientation dependent IE) and [145] (interplay of substrate and growth). The XRD measurements were performed with the help of Ingo Salzmann. The calculations concerning the IE of lying and standing DH6T were done by Georg Heimel.

### 4.1.1 Lying monolayer/standing multilayer

The molecular orientation and the electronic structure of DH6T on Ag(111) was explored in detail using the experimental techniques UPS, XPS, and MAES, since DH6T/Ag(111) is a prototype system for a lying monolayer/standing multilayer transition, as found in the present work.

#### UPS

UPS measurements on DH6T/Ag(111) were performed with synchrotron radiation at the FLIPPER II end station and with He I radiation at Chiba University. Since the results differ slightly both experimental results are presented.

First the DH6T spectra measured at FLIPPER II are compared with the spectra of the unsubstituted 6T. The overall shape of the photoemission spectra of ca. a monolayer (nominal mass thickness  $4 \text{ \AA}$ ) of 6T and DH6T on Ag(111) was very similar [see Fig. 4.1 (a)], since the conjugated moieties of both molecules are the same. However, the DH6T spectrum was rigidly shifted towards lower binding energy. In the DH6T monolayer spectrum the peak centered at 1.60 eV BE was assigned to the HOMO and the peak centered at 2.20 eV BE to the HOMO-1. Close inspection reveals that the hole injection barrier was 0.15 eV smaller for a monolayer of DH6T compared to a monolayer of 6T. The same energy difference was found for the ionization energies of the two thin film samples ( $IE_{6T} = 5.00 \text{ eV}$  and  $IE_{DH6T} = 4.85 \text{ eV}$ ). The lower observed value for both  $\Delta_h$  and IE of DH6T can be explained by increased intramolecular screening due to the additionally available electron density on the hexyl chains, which are absent for 6T. The similarity of 6T and DH6T photoemission spectra and electronic properties is consistent with flat lying molecules in a monolayer DH6T.

In contrast to other organic rodlike molecules, such as PEN, 6P, or 6T [18, 19, 102] the photoemission spectra of multilayer DH6T films on Ag(111) [bottom curve in Fig. 4.1 (a)] were shifted towards *lower* BE compared to the monolayer (L1). In order to investigate the origin of that unusual shift, coverage-dependent photoemission spectra of DH6T on Ag(111) [Fig. 4.1 (b)] were recorded. Notably, there was no gradual shift of DH6T features, but

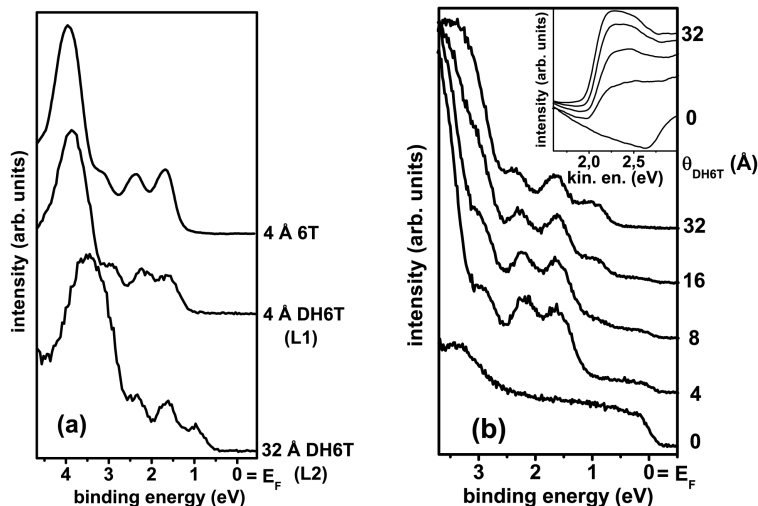


Figure 4.1: (a) UPS spectra of 4 Å 6T/Ag(111) (top), 4 Å DH6T/Ag(111) (middle), and 32 Å DH6T/Ag(111) (bottom). The contribution from the Ag substrate was subtracted from both 4 Å films. (b) Low BE range photoemission spectra for increasing DH6T coverage ( $\theta_{DH6T}$ ) on Ag(111). The inset shows the secondary electron cutoff, “kin. en.” means kinetic energy.

for coverages larger than 4 Å a new emission feature appeared at the low BE side of the monolayer HOMO (centered at ca. 0.90 eV BE), and remained at constant BE for increasing coverage. With increasing DH6T thickness the intensity of the new peak was also increasing. This new peak was therefore assigned to the HOMO of the second layer (L2) DH6T. For L2 not only the HOMO was located at lower binding energies, but the whole DH6T spectrum was shifted rigidly to lower BE. The intensity ratio of HOMO and HOMO-1 changed from nearly 1:1 in L1 to 1:2 in L2. As evident from a comparison of the 4 Å and the 32 Å DH6T/Ag(111) spectra, the HOMO of L1 DH6T coincidentally appeared at the same BE as the HOMO-1 of L2 DH6T. The new HOMO position for L2 DH6T lowered  $\Delta_h$  by 0.50 eV compared to L1. Noteworthy, no further change in the sample work function after the initial  $\phi$  reduction due to the electron push back effect during L1 formation [see inset of Fig. 4.1 (b)] could be observed.

For DH6T/Ag(111)  $\Delta_h$  is reduced with increasing coverage, but in general,  $\Delta_h$  for organic materials deposited on metal substrates increases slightly (a few tenths of an eV) as a function of film thickness [18, 19] e.g., from 1.23 eV for a monolayer 6T/Ag(111) to 1.38 eV for multilayers [102]. A reduction of  $\Delta_h$  has only been reported on a larger thickness scale (in the order of sev-

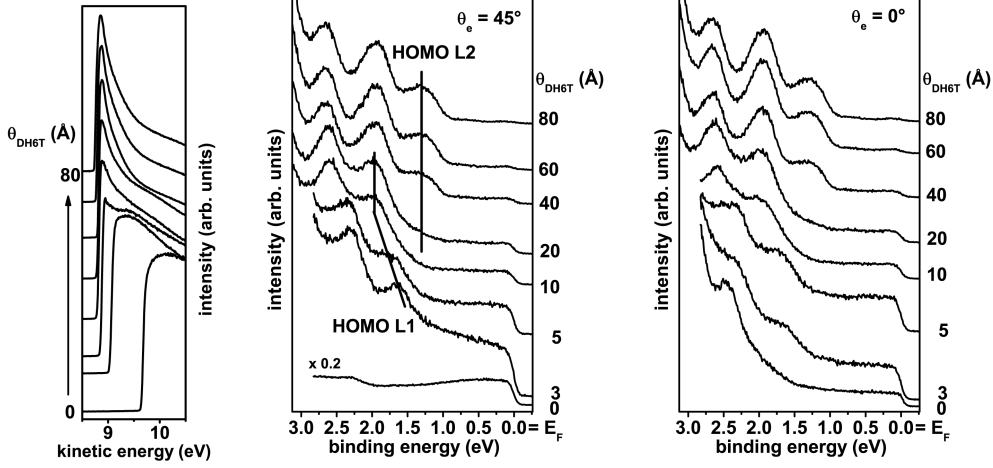


Figure 4.2: UPS results of the thickness series of DH6T/Ag(111).  $\theta_{DH6T}$  denotes the DH6T coverage and  $\theta_e$  the photoelectron take-off angle.

eral organic layers) for PEN [22, 23]. This behavior has been attributed to a transition from lying to standing PEN. In analogy, the  $\Delta_h$  shift of 0.50 eV between L1 and L2 is attributed to a transition from flat lying DH6T to standing DH6T. This assumption has been proofed by means of atomic force microscopy, where distinct step heights of 35 Å of multilayer island have been found [143], corresponding to nearly upright standing DH6T with a length in the all-trans conformation of 38.1 Å [121]. The lying monolayer/standing multilayer growth model will be also confirmed by complementary experimental techniques later in this section, but for reasons of coherence the He I UPS results will be discussed first.

The UPS spectra of DH6T/Ag(111) measured with He I [Fig. 4.2] are similar to the FLIPPER II data, but exhibit some differences. The main difference was the first appearance of the L2 photoemission features at higher DH6T coverages in the He I experiments. Up to a coverage of 5 Å the spectra were very similar to the FLIPPER II data with the HOMO centered at 1.60 eV BE, but increasing the DH6T coverage to 10 Å did not result in a new photoemission feature at the low binding energy side of the HOMO, but shifted the spectrum to higher binding energies. This behavior can be explained by screening by the metal substrate. However, in this set of experiments the formation of the standing phase did not start after a nominal monolayer coverage. Just for coverages higher 10 Å the formation of standing multilayer began. The shift between the L1 HOMO (10 Å DH6T) and the L2 HOMO (80 Å DH6T) was again 0.50 eV. The SECO did not exhibit a shift



after monolayer formation. The ionization energy was 5.05 eV for lying and 4.55 eV for standing DH6T, i.e. slightly larger than the IEs of the FLIPPER II samples. In the case of measurements with He I coverages of up to 80 Å could be measured, whereas with synchrotron light for coverages higher than 40 Å the sample exhibited charging. In addition to these differences, which can be attributed to different growth modes in the two sets of experiments, also the different excitation mechanisms (synchrotron light vs. He I radiation) impacts the results. In the He I measurements the transition from lying to standing DH6T did not result in different intensity contributions to HOMO and HOMO-1 (compare the 10 Å and the 80 Å spectra). Thus, the additional tool of the intensity contribution to distinguish between lying and standing DH6T is only provided by the FLIPPER II data.

Although the used Ag(111) single crystal substrates were nominally equal, slight differences in surface properties like varying terrace sizes or step edge densities can have enormous impact on organic thin film growth [79, 82]. The crystals have been cleaned in the same way (by repeated sputter and annealing cycles) and in both cases a clear LEED pattern could be observed. However, it is probable, that the both crystals did not exhibit exactly the same surface properties. This is corroborated by the slightly different work functions of the pristine crystals ( $\phi_{FLIPPER II} = 4.40$  eV and  $\phi_{Chiba} = 4.55$  eV). Also the preparation conditions of the organic thin film may differ in the two experimental setups. Especially the substrate temperature during film growth can impact the growth of organic thin films heavily [115, 146, 147]. The substrate surface temperature could not be controlled in both laboratories, therefore it could not be confirmed, that the substrate cooled down to room temperature before the evaporation of the organic film. The given thickness values corresponds to the mass thickness given by the quartz crystal microbalance. The evaporation geometries in the UHV-chambers may cause a mismatch between the measured thickness value on the microbalance and the real thickness on the sample. However, in both experimental setups the microbalance was very close to the sample and the distance from the evaporator to the sample rather large. Moreover, in many other experiments in both preparation chambers the correct thickness assignment has been confirmed. Thus, the impact of a wrong tooling factor cannot explain the mismatch in the experimental findings in a simple way. However, the entirety of the slightly different substrates and growth conditions may lead to the observed variation of the critical coverage for the orientational transition and the slightly different IEs of the DH6T films in the two laboratories.

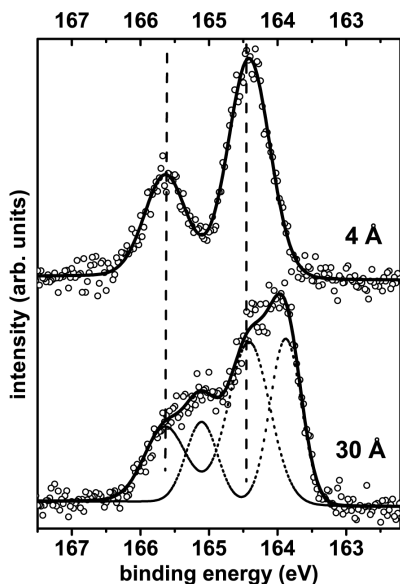


Figure 4.3: XPS spectra of S(2p) core levels of 4 Å and 30 Å DH6T films on Ag(111). Straight lines represent the resulting fits, dashed lines are the fits of L1 and L2 contribution to the 30 Å film peak.

## XPS

It is interesting, whether also the core levels were involved in the shift of the valence orbital levels at the L1/L2 interface. For this reason XPS measurements were performed on DH6T/Ag(111) films. Fig. 4.3 displays the spectra of the S(2p) core levels of DH6T on Ag(111). For monolayer coverage (4 Å) the peaks were centered at 164.40 eV BE [S(2p<sub>1/2</sub>)] and 165.65 eV [S(2p<sub>3/2</sub>)], respectively. For multilayer coverage (30 Å) new photoemission features appeared at the low BE sides of the peaks. Fitting the data with fixed L1 peak positions and additional L2 peaks resulted in L2 peaks shifted 0.55 eV to lower BE. This shift corresponded well with the shift in the valence electron region between L1 and L2 of DH6T/Ag(111) of 0.50 eV. Also the C(1s) peak shifted from monolayer to multilayer coverage to lower binding energies, but due to the presence of C in six different chemical environments in DH6T the peak was very broad even for monolayer coverage and does not allow for unambiguous feature assignment.

## MAES

In order to get a more direct information on the molecular orientation of DH6T/Ag(111) and to confirm our assignments based on UPS (see above), MAES spectra were recorded. The analysis of these spectra requires knowledge about the molecular orbitals of DH6T. In Fig. 4.4 the results of calcula-

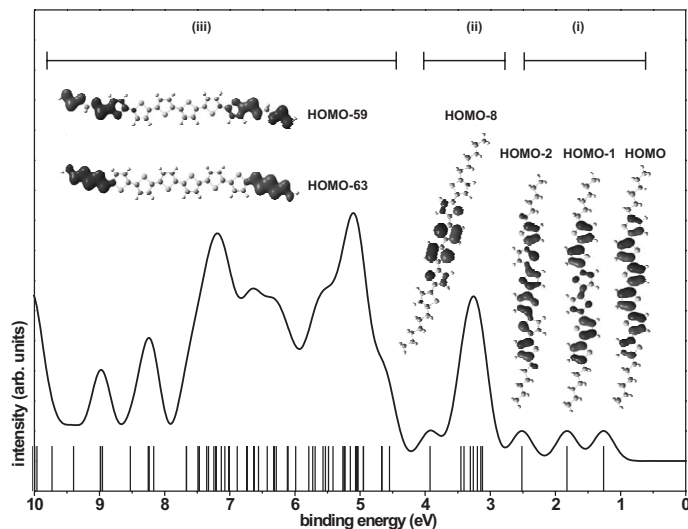


Figure 4.4: Energy eigenvalues and simulated gaussian broadened spectrum of DH6T. The values are vertically shifted and extended. Some exemplary molecular orbital states are displayed for the regions discussed in the text: (i) HOMO, HOMO-1 and HOMO-2, (ii) HOMO-8 as representative for the localized  $\pi$ -states and (iii) HOMO-59 and HOMO-63 as typical representatives for the hexyl dominated orbitals in the higher binding energy region.

tions of the molecular orbitals of DH6T and a simulated Gaussian broadened DH6T spectrum are shown. The spectrum can be divided into three characteristic regions [see Fig. 4.4]: part (i) at low binding energies is assigned to delocalized  $\pi$ -orbitals of the conjugated 6T core, consisting of HOMO, HOMO-1 and HOMO-2. Part (ii) is dominated by six narrowly spaced localized  $\pi$ -states and part (iii) on the higher binding energy side is dominated by  $\sigma$ -states localized mainly on the alkyl chains of DH6T.

In the MAES spectra [Fig. 4.5], the deposition of up to 10 Å DH6T on Ag(111) suppressed the metal derived features and features attributed to the organic molecules appeared. HOMO, HOMO-1 and HOMO-2 were hardly resolvable even for the thicker DH6T films, however the localized  $\pi$ -peak centered around 5.30 eV BE was clearly visible. In the higher binding energy region several alkyl chain derived peaks appeared. With increasing DH6T coverage the intensity of the 5.30 eV BE peak increased to a maximum at a film thickness of 10 Å and decreased again for higher coverages.

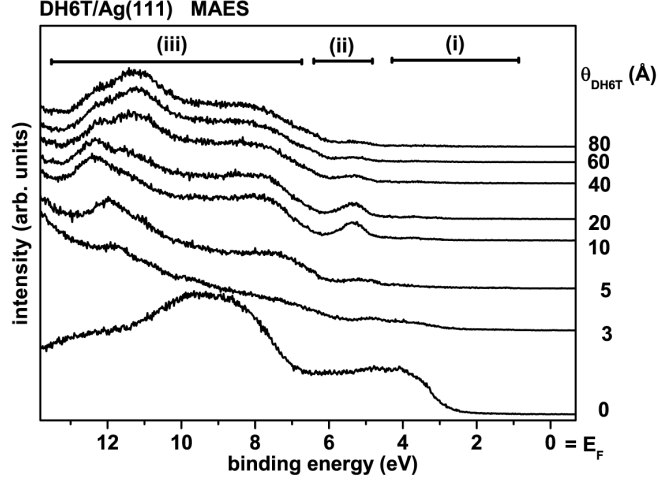


Figure 4.5: MAES results of the thickness series of DH6T/Ag(111).  $\theta_{DH6T}$  denotes the DH6T coverage. The regions where emission from the conjugated backbones (i and ii) and from the hexyl chains (iii) dominates the spectra are marked by lines.

For the discussion of the molecular orientation of DH6T/Ag(111) the peak of the six narrowly spaced localized  $\pi$ -states around 5.30 eV BE in the MAES spectra is of importance. In this binding energy region no alkyl chain derived states are expected from the calculations. For lying DH6T both the alkyl chains and the conjugated backbone are accessible for MAES. However, for standing DH6T, with the alkyl chains forming the outermost surface of the film, the  $\pi$ -states of the conjugated part are not accessible. Therefore, the intensity of this peak can be used to gather information about the composition of the layer surface. For comparison, in case of the DH6T related polymer poly(3-hexylthiophene) (P3HT), the P3HT HOMO is totally suppressed in the MAES spectra if P3HT is in edge-on orientation with the hexyl chains on top. If P3HT is in face-on orientation the P3HT HOMO could be observed [25]. The reduction of the intensity of the localized  $\pi$ -state with increasing DH6T coverage in the MAES spectra supports the lying monolayer/standing multilayer model. In contradiction to P3HT the peak is not suppressed totally even for 80 Å DH6T coverage. This behavior can be explained with island growth of standing DH6T, so that also for nominal multilayer coverage part of the monolayer is still accessible for MAES.

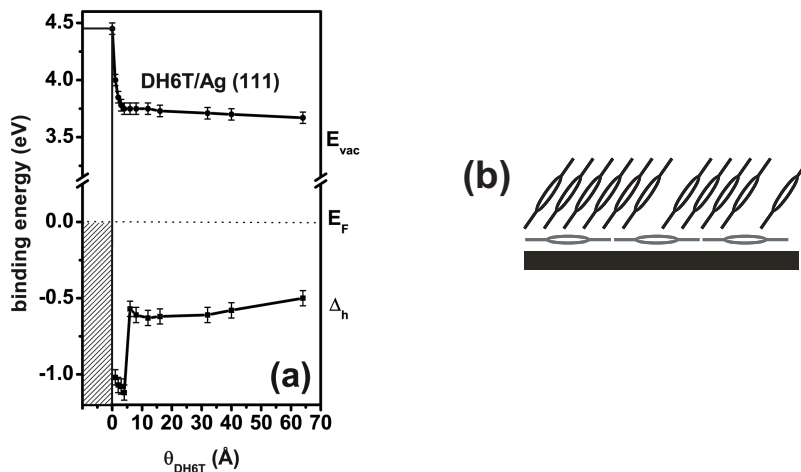


Figure 4.6: (a) Schematic energy level diagram for DH6T on Ag(111).  $\theta_{DH6T}$  denotes the DH6T thickness,  $E_{vac}$  the vacuum level, and  $\Delta_h$  the hole injection barrier (HOMO-onset),  $E_F$  is the Fermi-level of the metal substrate (b) Sketch of proposed growth model of DH6T/Ag(111).

### Summary of DH6T/Ag(111)

The results on growth and electronic structure are summarized in Fig. 4.6 (a), where an energy level diagram derived from UPS measurements at FLIPPER II is given and in Fig. 4.6 (b), where the corresponding growth model is shown. The abrupt change in the molecular orientation from lying monolayer to standing multilayer is directly reflected in the electronic structure of the DH6T/Ag(111) sample. The orientational transition leads to a lowering of the hole injection barrier by 0.50 eV. The vacuum level stays constant at the L1/L2 interface, therefore also the ionization energy is lowered for standing DH6T compared with lying DH6T. The UPS results with He I yielded slightly different results, but for the discussion it is not of relevance, if the lying phase consists of one or two nominal layers. Note, that for DH6T/metals in this work “L1” is used as acronym for the lying phase and “L2” as acronym for the standing phase. For clarification of the reason for the change in the electronic structure by the orientational transition, further experiments have been performed.

### 4.1.2 Upper limit for orientation induced polarization effects

For other organic systems where shifts of energy levels in the order of 0.50 eV have also been observed depending on the orientation of the molecules, different polarization energies for lying and standing molecules has been claimed out to explain the energy level shifts [22–24, 148, 149]. Closely related to this approach is the “screening” effect [Section 2.2.1], i.e. the observation in PES that the energy levels of an organic adsorbate on metals occurs at up to 0.40 eV higher binding energies for multilayers than for monolayers, which is originated in the different polarization energies of metals and COMs. However, it seems unlikely that the anisotropic polarizability of organic films should lead to an effect of larger magnitude than the screening of the metal substrate.

In order to obtain an upper limit for the difference in photo-hole screening by differently oriented neighboring molecules, the following scenario is considered: A photo-hole created in the topmost organic layer is screened only by the lower half-space of surrounding molecules (and, possibly, the metal substrate). A photo-hole created on a molecule deeper in the organic film is screened by a lower *and* upper half-space of surrounding molecules. Clearly, the presence or absence of neighboring molecules in the upper half-space must have a more pronounced effect on the polarization energy (and thus the measured IE) than differences in the orientation of the neighboring molecules. The S(2p) XPS signal of a 20 Å 6T film on Ag(111) that was buried by subsequently deposited layers of  $\alpha$ -NPD was measured, which exhibits an amorphous growth mode and does not contain sulfur itself.

Fig. 4.7 shows that, for the pristine 6T layer, the stronger S(2p<sub>3/2</sub>) peak was centered at a binding energy of 164.58 eV. Upon subsequent deposition of 20 Å  $\alpha$ -NPD, the peak shifted by 0.14 eV towards lower binding energy, i.e., to 164.44 eV. Upon further deposition of  $\alpha$ -NPD, the peak energy stayed constant to within 0.05 eV. It is thus established that the presence or absence of a half-space of  $\pi$ -conjugated molecules contributes a maximum of ca. 0.15 eV to the polarization energy of the photo-hole, consistent with similar results in Refs. [150, 151]. Also, re-examining the XPS data in Figure 4.3 leads to similar result: The binding energy of the S(2p) peaks attributed to the first (lying) layer of DH6T does not change upon deposition of subsequent layers of DH6T. Consequently, the effect of different orientation of neighboring molecules can be expected to be less than 0.15 eV.

It is more difficult to demonstrate the influence of capping layers on the UPS spectrum of underlying layers than on the XPS spectrum, because of the larger information depth and the straight-forward peak assignment in

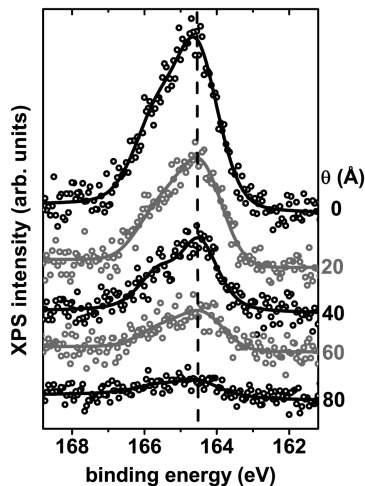


Figure 4.7: Al  $K_{\alpha}$  XPS spectra of the sulfur 2p region of 20 Å of 6T/Ag(111) subsequently covered with  $\alpha$ -NPD as function of  $\alpha$ -NPD thickness ( $\theta$ ) and corresponding fits. The dashed line is a guide for the eye.

XPS. However, it was reported that the UPS spectra of Xe and Kr adsorbed on Pd(001) are hardly affected by the adsorption of Ar as top layer [152]. Because of the short lifetime of core holes [153], which are filled very rapidly by electrons from the valence region [154], screening should be the same in XPS and UPS; indeed, no substantial differences could be observed for screening by the metal substrates for rare-gas multilayers in XPS and UPS [152].

Clearly, with the upper limit for orientation induced changes in the polarizability of COMs of 0.15 eV, the change of 0.50 eV between L1 and L2 DH6T/Ag(111) cannot be explained by different polarization energies of L1 and L2 alone. The question arises, why molecular crystals should not have an orientation dependent IE, similar to  $\phi$  of metal single crystals, which depend on the orientation of the crystal.

### 4.1.3 Orientation dependent IE of COMs

It is well established that the work function of metals depends on the crystal face [50, 155, 156].  $\phi$  is defined as the energy difference between  $E_F$  and the electrostatic potential in the vacuum above the sample. For, e.g., copper,  $\phi$  of the (100), (110), and (111) surfaces is spread over a range of 0.50 eV [155, 156]. As  $E_F$  is constant, this observation has been explained by the difference

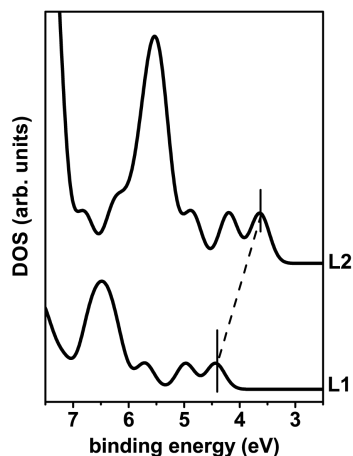


Figure 4.8: Calculated spectra of DH6T in the lying (L1) and the standing (L2) phase. The spectra are referenced to  $E_{vac}$ . This plot is taken from Ref. [144].

in the intrinsic “surface dipole”: Differences in the surface geometric and, consequently, electronic structure cause a different amount of the electron cloud to spill out of the bulk into vacuum [50, 157]. The resulting dipoles raise  $E_{vac}$  to a larger or smaller extent and thus impact  $\phi$  [157, 158]. Note that this effect can only be observed for laterally extended surfaces, as the spatial region above the sample where  $E_{vac}$  is raised reaches farther away from the surface with increasing sample size (i.e., area of the exposed surface) [19, 101]; small metal nanoparticles with multiple facets of different crystal orientations have only one well-defined ionization potential [159, 160].

For non-covalent (i.e., van der Waals) crystals, surface dipoles and work-function anisotropy have not yet been explored. While variations of several tenths of an eV in the ionization energy depending on the molecular orientation on a surface have been reported before [22, 23, 149], no consistent picture has emerged. For the case of DH6T/Ag(111) DFT calculations were performed in order to see if the 0.50 eV offset between lying and standing DH6T can be explained by a phenomena similar to the metallic case.

The occupied density-of-states (DOS) calculated with DFT [144] for a lying and standing layer of DH6T is shown in Fig. 4.8. In addition to good qualitative agreement with the experimental UPS spectra [Fig. 4.1 and Fig 4.2], we find that indeed, all molecular levels are closer to  $E_{vac}$  for the lying DH6T compared to the standing DH6T, i.e., the IE is lower for standing molecules.

A simple electrostatic model demonstrates the impact of intramolecular dipoles on IE of a molecule. Since the saturated hexyl chains do not have an intramolecular dipole, they can be neglected. The  $\pi$ -electron system above and below each thiophene ring is clearly negatively charged; these negative charges are compensated by point charges in the plane of the molecule



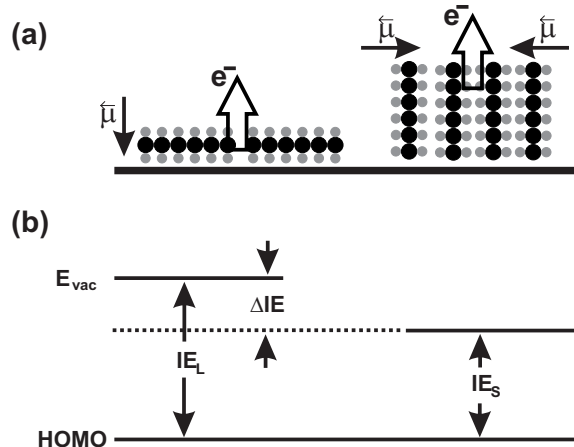


Figure 4.9: (a) Electrostatic modeling of the orientation-dependent ionization energy of 6T. Gray circles correspond to the negatively charged  $\pi$ -system above and below each thiophene ring. Black circles are the positive charge in the plane of the molecule.  $\vec{\mu}$  means the interface dipole moment. (b) Impact of  $\vec{\mu}$  on IE.  $IE_L$  is the ionization energy of lying and  $IE_S$  of standing molecules.  $\Delta IE$  is the surface dipole induced difference in IE.

[Fig. 4.9]. Even for a single molecule this inhomogeneous charge distribution leads to an inhomogeneous electrical potential around the molecule. But this potential converges extremely rapidly, so that no orientation dependent IE can be measured. The situation changes for molecular crystals as soon as the lateral extent of the supra-molecular structure is large compared to a single molecule. Now intermolecular dipole-dipole and quadrupole-quadrupole interaction leads to a slower convergency of the inhomogeneous potential. Thus, an interface dipole arises with its dipole moment perpendicular to the molecular long axis [Fig. 4.9 (a)]. The IE for electrons ejected along such a dipole is larger than for electrons ejected perpendicular to the dipole [Fig. 4.9 (b)]. This behavior explains the measured IE difference for lying and standing DH6T. Note that, while the surface dipole of metals can be pushed back upon adsorption of molecules, these intramolecular surface dipoles are not changed upon establishing contact to either the (metal) substrate or another organic layer (in the absence of chemical reactions). For macroscopic samples in UPS experiments the orientation of the crystal to the substrate and *not* the angle between detector and sample is relevant for IE.

The qualitative considerations presented above have been rationalized quantitatively in Ref. [144] with two models. One simple electrostatic model is similar to Fig. 4.9 (a) with 6T modeled by point charges. From this model an infinite molecular 6T-crystal was built. In a second model the 6T crystals

were calculated with DFT. Both models reveal similar results fitting well to the experimental values.

#### 4.1.4 Influence of substrate on molecular growth

At this point the question why standing DH6T molecules exhibit an electronic structure different to lying DH6T could be answered. But still the driving force for DH6T to stand up is unknown. In order to elucidate this issue, DH6T and 6T have been investigated on a variety of substrates with different experimental techniques. Since DH6T/Ag(111) acts as a reference case, XRD measurements were performed, allowing the determination of the unit cell. DH6T was measured on Au(111) and polycrystalline Au to test the generality of the concept of lying L1/standing L2 on metals. HOPG as substrate acts as a reference case of a weakly interacting system. Ag(111) pre-covered with TTC tests the role of alkyl chains in the standing up process. Furthermore experiments on 6T/DH6T heterostructures were performed that demonstrate the ability of DH6T to change the growth mode of 6T.

#### XRD

X-ray diffraction measurements were performed on DH6T films of 48 Å nominal thickness on Ag(111), the results are summarized in Fig. 4.10. The XRR spectrum exhibited Kiessig-fringes [111] at low values of momentum trans-

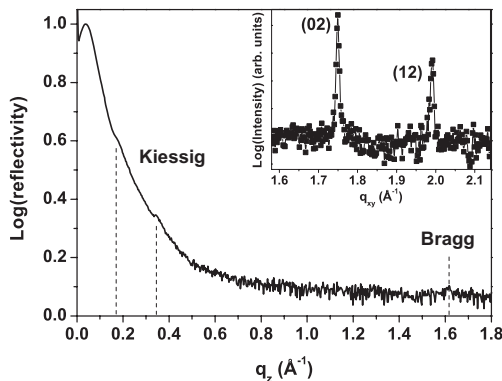


Figure 4.10: XRR and GID (inset) spectra of a nominally 48 Å thick DH6T film on Ag(111). XRR exhibits Kiessig fringes at low  $q_z$  values and a weak indication of a Bragg peak at high  $q_z$ , both features are marked with lines.

fer ( $q_z$ ) that can be attributed to a smooth DH6T film of 36.5 Å thickness. A weak Bragg peak corresponding to a lattice spacing of 3.9 Å was found. In the GID spectrum two pronounced peaks at  $q_z$  values of 1.749 Å<sup>-1</sup> and



Figure 4.11: Example of a herringbone motif.

$1.990 \text{ \AA}^{-1}$  could be observed corresponding to lattice planes perpendicular to the sample surface, which was confirmed by out-of plane scans along the exit angle  $\alpha_f$ . These in-plane reflections correspond to lattice spacings of  $3.59 \text{ \AA}$  and  $3.16 \text{ \AA}$ , which can not be explained by the structures of DH6T reported up to now [117, 121]. However, from our findings a unit cell for DH6T/Ag(111) can be modeled if a structure of the 6T-backbone similar to pristine 6T is proposed.

The vertical thickness of  $36.5 \text{ \AA}$  derived from the Kiessig fringes in XRR is slightly larger than the reported diffraction spacing of  $35.5 \text{ \AA}$  for a DH6T film on  $\text{SiO}_2$  composed of molecules tilted by  $16^\circ$  with respect to the substrate normal [121]. Moreover, the reported unit cell cannot be used to explain the present GID results. The XRD results of DH6T/Ag(111) are not sufficient to derive the unit cell of DH6T without further assumptions, since only two in-plane peaks could be observed.<sup>1</sup> However, it is reasonable to assume that the 6T backbone of DH6T adopts a similar packing motif as in all reported cases in various environments [117, 161–163], i.e. a monoclinic unit cell with a herringbone motif [Fig 4.11]. The two 6T polymorphs for which a unit cell could be determined [117, 163] exhibit rather different unit cell dimensions but almost the same unit cell volume (difference  $< 1\%$ ), a fact which can also be confirmed for other rodlike organic molecules like pentacene [164, 165], where the unit cell volumes of all known polymorphs differs by less than  $5\%$ . Therefore, the following approach is reasonable: (i) fix the unit cell volume in the model for the DH6T backbone structure in the vicinity of the reported values for pristine 6T, (ii) find unit cell dimensions  $a$  and  $b$  that allow to index the GID peaks with lowermost indices  $(hk0)$  by permutation of  $h, k$  and that is most similar to one of the known structures of 6T. Following this approach allows to propose the following unit cell for the 6T backbone of DH6T:  $a = 6.631 \text{ \AA}$ ,  $b = 7.180 \text{ \AA}$ ,  $c = 22.35 \text{ \AA}$ ,  $\beta = (90 \pm 1)^\circ$ , which is

<sup>1</sup>It can be excluded that the reflections found in GID stem from lying DH6T molecules, since the corresponding lattice spacings are far below the extensions of the DH6T molecule, no peak at low momentum transfer could be observed and textured growth of lying DH6T on the single crystal substrate has to be expected, which is highly unlikely to be observed without azimuthal sample rotation (not performed due to experimental limitations).

	a (Å)	b (Å)	c (Å)	$\beta$	Z	V (Å <sup>3</sup> )
Horowitz et al.[117]	6.029	7.851	44.708	89.24°	4	2116
6T backbone	6.631	7.180	22.25	(90 ± 1)°	2	1059
DH6T	6.631	7.180	36.5	(90 ± 1)°	2	1738

Table 4.1: Unit cell dimensions of the 6T crystal structure reported by Horowitz et al. [117] (transformed to ascending axis dimensions), of the standing phase of the DH6T conjugated backbone and of DH6T/Ag(111). Z denotes the number of molecules in the unit cell, V is cell volume. The tilt angle between backbone and hexyl-chains in the latter case was determined to 28°.

similar to the unit cell reported by Horowitz et al. [117]. The two GID peaks can then be assigned to the (020) and (120) reflections. Taking into account the film thickness of 36.5 Å derived from the oscillations in the XRR spectrum, the unit cell dimensions of *standing* DH6T on *lying* DH6T can now be modeled. The small Bragg peak in the XRR spectrum that corresponds to a lattice spacing of 3.9 Å, is an indication of a lying DH6T layer consisting of at least two layers, since one single layer cannot cause Bragg diffraction. This finding together with a comparison to the recently reported structure of  $\alpha,\omega$ -dihexylquaterthiophene (DH4T) [166], allows to rule out that the thickness oscillations stem from the overall film thickness. This would lead to an unreasonably high mass density of  $> 1.3 \text{ g cm}^{-3}$  for the hexyl-chains of the standing molecules (DH4T:  $0.78 \text{ g cm}^{-3}$ ) as well as to a tilt angle of  $> 60^\circ$  (DH4T is fully extended). Therefore the spacing of 36.5 Å is proposed to correspond to the (001) lattice spacing ( $d_{001}$ ) of the DH6T structure, which leads to the following unit cell dimensions of the standing DH6T monolayer:  $a = 6.631 \text{ Å}$ ,  $b = 7.180$ ,  $c = 36.5 \text{ Å}$ ,  $\beta = (90 \pm 1)^\circ$ . The low tilt angle of the alkyl chains of 28°, as well as a mass density of ca.  $0.7 \text{ g cm}^{-3}$  for the volume occupied by the alkyl chains fit well to the DH4T values. The unit cell dimensions are summarized in Table 4.1.

This result for DH6T on Ag(111) supports the growth model of an abrupt change in molecular orientation in thin DH6T films on Ag(111).

### DH6T/Au

To show that the results for DH6T/Ag(111) are relevant for other metal substrates as well, UPS measurements of DH6T on the model substrate Au(111) and the application relevant substrate polycrystalline Au were performed. Thickness dependent spectra are shown in Fig. 4.12. For 4 Å DH6T on Au(111) [Fig. 4.12 (a)] the peaks at the lower BE side of the localized  $\pi$ -

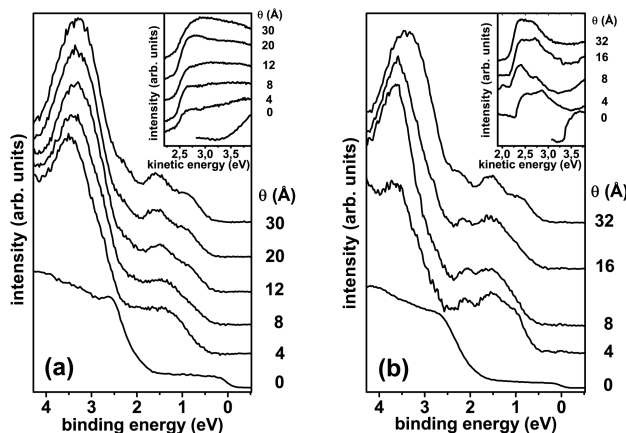


Figure 4.12: Thickness dependent UPS spectra of DH6T on the substrates (a) Au(111) and (b) polycrystalline Au. In all spectra the substrate contribution is subtracted.  $\theta$  means DH6T layer thickness. The insets display the secondary electron cutoff.

electron peak centered at 3.50 eV were smeared out and not clearly distinguishable. The hole injection barrier was 0.50 eV and IE 4.70 eV. Increasing the film thickness up to 12 Å resulted in a shift of molecular levels by 0.20 eV towards lower binding energies. Increasing the thickness further led to the development of three clearly distinguishable peaks between  $E_F$  and the 3.50 eV peak. These peaks were assigned as HOMO, HOMO-1 and HOMO-2. Increasing the film thickness did not change the vacuum level, so multilayer DH6T on Au(111) had an IE of 4.50 eV. DH6T on polycrystalline Au exhibited a similar behavior, but the slightly lower substrate  $\phi$  [5.10 eV, compared to 5.20 eV of Au(111)] led to a different energy level alignment. L1 DH6T/Au had a  $\Delta_h$  of 0.60 eV and an IE of 4.55 eV, L2 DH6T/Au a  $\Delta_h$  of 0.45 eV and an IE of 4.30 eV. For DH6T on polycrystalline Au, even for monolayer coverage HOMO and HOMO-1 could be resolved separately.

As for DH6T/Ag(111) also for DH6T on both, the poly- and single crystalline Au, going from monolayer to multilayer coverage changed the intensity contribution to HOMO and HOMO-1 and shifted the spectra to lower binding energies. These changes are again interpreted as change in DH6T morphology from lying molecules in the monolayer to inclined molecules in multilayer. But due to the different chemical interaction between DH6T and Ag on the one hand and DH6T and Au on the other hand, especially in the monolayer regime some differences existed. On both Au substrates the shift of molecular levels set on beyond the nominal monolayer coverage and was

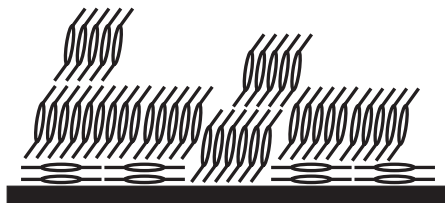


Figure 4.13: Possible growth model of DH6T/Au.

smaller compared to the shift of DH6T on Ag(111). These observations suggest different adsorptions mechanisms on the different metals. It is possible that a part of the molecules is inclined also in the submonolayer coverage range on Au [Fig. 4.13], leading to a superposition of the emission from lying and inclined molecules.

These results underline that the effect of lying L1/standing L2 is rather general for DH6T on metals. As long as the first DH6T layer grows lying on the surface, which is likely to occur on a variety of metals due to the relatively strong interaction between the  $\pi$ -system of the COM and metal bands, a similar situation will be encountered.

### DH6T/HOPG

In the case of DH6T/HOPG [Fig. 4.14] the UPS spectra appeared to be qualitatively similar to DH6T/Ag(111) up to a coverage of 20 Å, but the absolute energy positions of the peaks were different: 1.25 eV BE and 1.80 eV BE for HOMO and HOMO-1, respectively. At 20 Å coverage the peak-width increased, however without a substantial change of the peak maxima position. Therefore the hole injection barrier was reduced from 1.00 eV in the monolayer region to 0.60 eV in the multilayer. The vacuum level stayed essentially constant throughout the deposition of DH6T on HOPG, i.e. the ionization energy was reduced from 5.50 eV (L1) to 5.05 eV (L2). In MAES the feature at 13.1 eV BE is assigned to a final state structure originated in the  $\sigma^*$  band [167, 168]. This feature was visible up to a coverage of 20 Å. The adsorbate exhibited clear features in the alkyl chain region as well as in the conjugated backbone region for all investigated coverage values. Opposite to DH6T/Ag(111) the intensity of the peak of the localized  $\pi$ -states was not decreased by increasing the DH6T coverage.

### DH6T/TTC/Ag(111)

The experiments on DH6T/TTC/Ag(111) were conducted in order to test the role of the alkyl chains in the observed process of the orientational transition

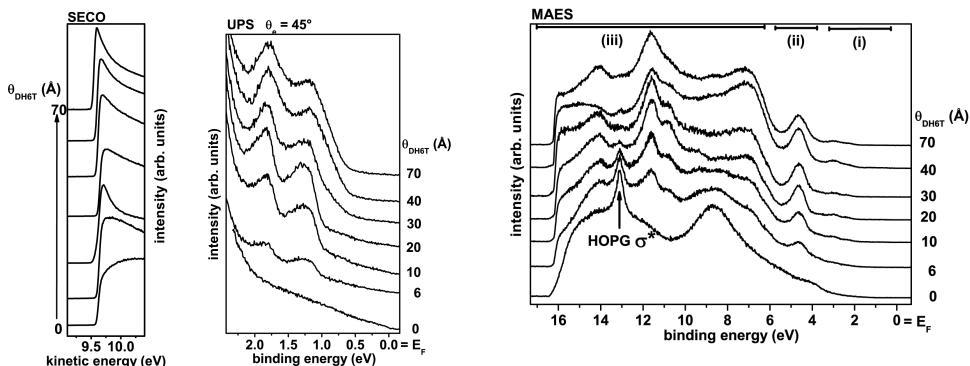


Figure 4.14: UPS and MAES results of the thickness series of DH6T on HOPG. From left to right the secondary electron region and the valence electron region of the UPS spectra and the MAES spectra are displayed.  $\theta_{DH6T}$  denotes the DH6T coverage and  $\theta_e$  the photoelectron take-off angle. UPS was additionally measured with  $\theta_e = 0^\circ$  yielding essentially the same results as for  $\theta_e = 45^\circ$ . In the MAES spectra the regions where emission from the conjugated backbones (i and ii) and from the hexyl chains (iii) dominates the spectra are marked. All these spectra were measured at Chiba University.

of DH6T on Ag(111). TTC is a long alkane which forms highly ordered lying monolayers on various metal substrates [132–134].

In the case of DH6T/TTC/Ag(111) [Fig. 4.15] the substrate pre-coverage by 4 Å TTC decreased  $\phi$  by 0.55 eV. In the valence region of the UPS spectra the metal derived features were suppressed, but no features of the saturated TTC could be measured. In MAES all Ag(111) derived features were suppressed upon TTC deposition. The spectrum was similar to a reported monolayer TTC spectrum on Ag [44]. Therefore, it can be concluded, that this TTC coverage corresponds to a closed and well ordered monolayer of TTC on Ag(111). Depositing up to 8 Å DH6T on the TTC pre-covered Ag(111) substrate resulted in molecule derived features in the UPS spectra that were very similar to DH6T on pristine Ag(111), with HOMO and HOMO-1 peaks centered at 1.85 eV BE and 2.50 eV BE, respectively. In this case, the work function was decreased to 3.75 eV. The IE was 5.05 eV. The deposition of multilayer DH6T on TTC/Ag(111) did not result in a new peak at the low binding energy side of the former HOMO, like for DH6T on pristine Ag(111). In MAES, neither the localized  $\pi$ -peak nor the delocalized  $\pi$ -orbitals of DH6T could be observed in the low binding energy region for all DH6T coverages. However, in the higher BE region alkyl chain derived emission could be observed.

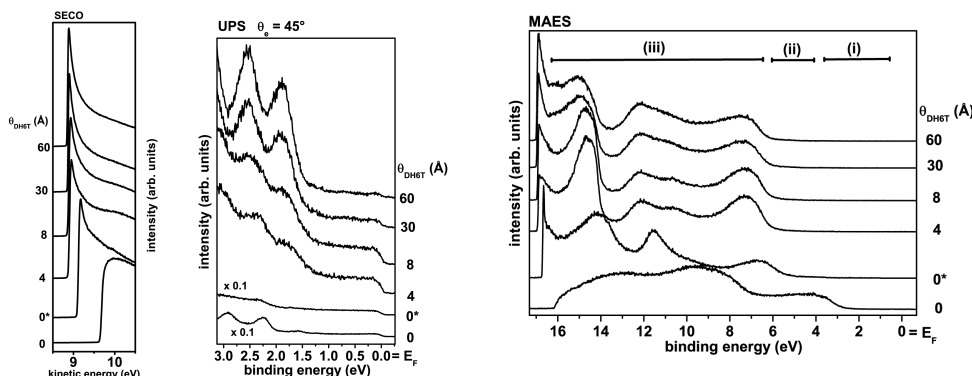


Figure 4.15: UPS and MAES results of the thickness series of DH6T on TTC/Ag(111).  $\theta_{DH6T}$  denotes the DH6T coverage and  $\theta_e$  the photoelectron take-off angle. UPS was additionally measured with  $\theta_e = 0^\circ$  yielding essentially the same results as for  $\theta_e = 45^\circ$ . The label  $0^*$  means Ag(111) pre-covered with a monolayer TTC. In the MAES spectra the three different emission regimes are marked. All these spectra were measured at Chiba University.

### Summary of DH6T growth

For the discussion of the electron spectroscopic results with respect to the molecular orientation two main parameters have to be considered in analogy to the results of DH6T/Ag(111): (i) The ionization energy given by the UPS results. The IE strongly depends on the orientation of the 6T core of DH6T and thus provides information about the orientation of the conjugated backbone of the molecule. And (ii) the existence of the peak of the six narrowly spaced localized  $\pi$ -states around 5 eV BE in the MAES spectra which is only accessible for lying molecules. In Table 4.2 the ionization energies found for mono- and multilayer DH6T on the respective substrates are summarized. In this table for the IEs of DH6T/Ag(111) the values from the measurements at Chiba University are taken. Also in the discussion of growth modes the model with two lying layers is considered, since this growth mode was also observed in XRD measurements.

A growth model of DH6T/Ag(111) is given in Fig. 4.16. For the L2 orientation the unit cell established with XRR and GID is being used. Island growth mode of multilayers is concluded from the MAES spectra, where the peak of the localized  $\pi$ -states does not vanish totally even for thick films. In case of layer by layer or Stranski-Krastanov growth of L2, the observation of this peak would be hindered by the alkyl chains. The exact L1 structure



	Ag(111)	HOPG	TTC/Ag(111)
L1	5.05	5.50	5.05
L2	4.55	5.05	5.15

Table 4.2: Ionization energies in eV of monolayer (L1) and multilayer (L2) coverage of DH6T on the respective substrates.

is unknown, but the Chiba UPS results and X-ray diffraction results point to (at least) two lying layers. The top view structure of the lying phase was determined for DH6T on Au(111) by scanning tunneling microscopy (STM) [169]. An analogous orientation on Ag(111) can be expected, since the UPS spectra of DH6T on Ag(111) and on Au are very similar.

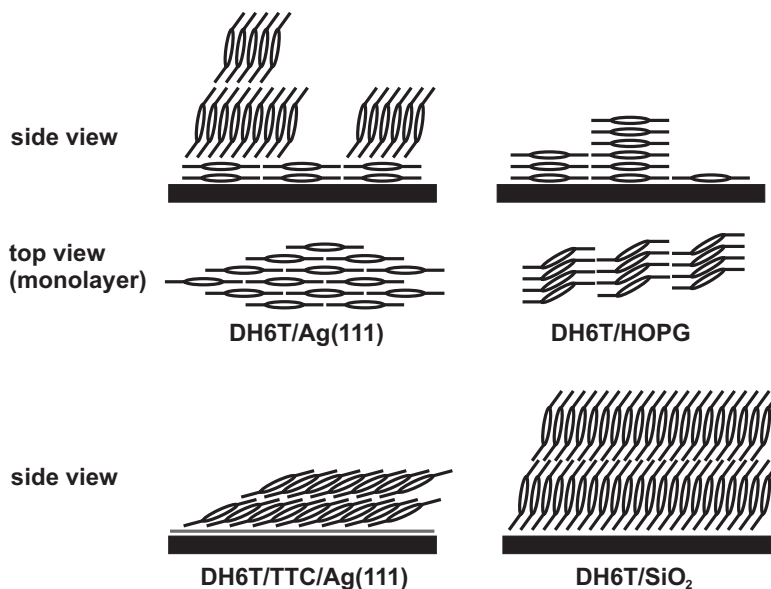


Figure 4.16: Proposed growth models of DH6T on the investigated substrates. The structure of DH6T/TTC/Ag(111) is one specific of several possible models. The top views for DH6T/Ag(111) [169] and DH6T/HOPG [170] are taken from literature. For the sake of completeness also the structure of DH6T/SiO<sub>2</sub> is shown, taken from Ref. [121].

In the case of DH6T on HOPG, no substantial changes could be observed between L1 and L2 coverage in both UPS as MAES spectra. The IE is reduced by this transition, but no shift of the HOMO and HOMO-1 peak maxima was observed. Therefore changes in the molecular orientation between mono- and multilayer are unlikely. The structure of the lying phase of DH6T/HOPG measured with STM in solution [170] resembles the bulk phase

of DH6T [121] (DH6T/SiO<sub>2</sub> in Fig. 4.16), merely the orientation with respect to the substrate surface plane is changed. Thus, DH6T can grow undisturbed in its bulk phase from monolayer coverage onwards on HOPG. A suggested growth model of DH6T/HOPG is shown in Fig. 4.16, where the orientation and conformation is taken from literature [121, 170]. Growth in the Stranski-Krastanov mode can be concluded from MAES, where up to a coverage of 20 Å (which is clearly more than a nominal lying monolayer) the HOPG  $\sigma^*$  signal can be observed; it vanishes for higher coverages. HOPG is known as substrate that allows growth of highly ordered organic thin films, which can exhibit band structures like in the case of PEN/HOPG [30]. Therefore it may be that also DH6T exhibits a significant band width on HOPG which could explain the observed broadening of HOMO and HOMO-1 without structural changes. Because the broadening of the HOMO causes a change in the IE, in the case of band dispersion the IE values cannot be used to make assumptions about the molecular orientation. The detailed analysis of electron band dispersion of DH6T, however, requires refined measurements.

At first glance, a contradiction between our UPS and MAES results in case of DH6T/TTC/Ag(111) exists. The ionization energy clearly points to a lying orientation of the molecules, but in MAES no peaks originating from the conjugated part of the molecules are being observed. Our XRR and GID results as well as literature data [121, 166] clearly show that the tilt angle between the alkyl chains and the conjugated backbone is flexible, i.e. DH6T cannot only change its orientation but also its conformation. A close inspection of the L2 films of DH6T on Ag(111) and on TTC/Ag(111) reveals differences in the specific part of MAES spectra, which is attributed to emission from the alkyl chains [Figs. 4.5 and 4.15]. In literature the influence of alkane orientation on MAES spectra has been discussed in detail [171, 172]. The hesitant increase in the hexyl derived emission on the low BE range (around 6 eV BE) for DH6T/Ag(111) is typical for almost standing alkyls [172], (as corroborated by XRR and GID). Whereas the fast increase of the hexyl emission intensity in the same part of the spectra of multilayers DH6T/TTC/Ag(111) points to almost lying alkyls [171]. At this point for DH6T/TTC/Ag(111) can be assumed: (i) lying 6T backbones, (ii) lying alkyl chains and (iii) only alkyl chains in the uppermost layer. It is impossible to find a growth model that fulfills all the prerequisites. But small deviations of the proposed orientations are possible, since the spectroscopic methods UPS and MAES only give molecular orientations with low accuracy. And indeed, little tilt angles of the DH6T components can lead to a possible growth model which satisfies all assumptions [Fig. 4.16].

Interestingly, the molecular orientation and conformation of the DH6T multilayer on Ag(111) and of DH6T/TTC/Ag(111) is very different. This

finding leads to deeper insight in driving forces for molecules to change their orientation. Since unsubstituted 6T on metals does not change its orientation at the L1/L2 interface, the transition of DH6T at this interface has to be related with the alkyl chains. Therefore DH6T on the pure alkyl chains of TTC/Ag(111) was expected to grow in the standing phase even for monolayer DH6T coverage. This is obviously not the case. Thus, it is demonstrated that the balanced interplay of alkyl chain and backbone influence impacts the molecular orientation and conformation in a crucial way. Even the position of the alkyl chains on the backbone has to be considered, since  $\beta, \beta'$  hexyl substituted 6T on Au does not change its orientation at the L1/L2 interface [141]. As expected from this observations, on HOPG the orientation and conformation is again different. In this case, the weakly interacting substrate allows DH6T to grow in the bulk phase from beginning.

### 6T/DH6T/metal

Opposite to DH6T, unsubstituted 6T does not exhibit an orientational transition at the L1/L2 interface [86, 87]. Since 6T is a promising candidate for organic field effect transistors [75, 116] it would be of great interest also to change the 6T orientation and thus  $\Delta_h$ . One approach is to deposit 6T on DH6T pre-patterned metal substrates.

UPS results of 6T/DH6T heterostructures are shown in Fig. 4.17 (a) and (b). Multilayer 6T on monolayer DH6T/Ag(111) [Fig. 4.17 (a)] had a  $\Delta_h$  of 1.25 eV and a IE of 4.85 eV, HOMO and HOMO-1 had an intensity ratio of 1:1. For multilayer 6T on multilayer DH6T the spectrum was shifted, it had a lower  $\Delta_h$  (0.85 eV) and IE (4.50 eV) and an intensity ratio of HOMO and HOMO-1 of almost 1:2. In both cases depositing 6T on DH6T did not change the SECO position essentially, the shift of 0.1 eV between 4 Å DH6T/Ag(111) and 100 Å 6T/4 Å DH6T/Ag(111) can be attributed to the formation of an interface dipole at the metal/organic interface due to the electron push back effect. Using polycrystalline Au as substrates yielded quantitatively the same results [Fig. 4.17 (b)]. The hole injection barrier of multilayer 6T changed from 1.00 eV to 0.70 eV and the IE from 4.60 eV to 4.35 eV by changing the DH6T pre-coverage thickness from 4 Å to 20 Å.

6T spectra on L1 DH6T pre-covered metals had the same peak positions and peak intensity contributions as the 6T spectra on pristine metals [Fig. 4.19]. The changes in 6T spectra by going to L2 DH6T pre-coverage were the same as the changes in DH6T spectra on pristine metals by the transition L1 to L2. Therefore a growth model as sketched in Fig. 4.18 (a) and (b) can be proposed. On the lying molecules of L1 DH6T also 6T is lying flat, like 6T direct on metals. But on the standing molecules of L2 DH6T

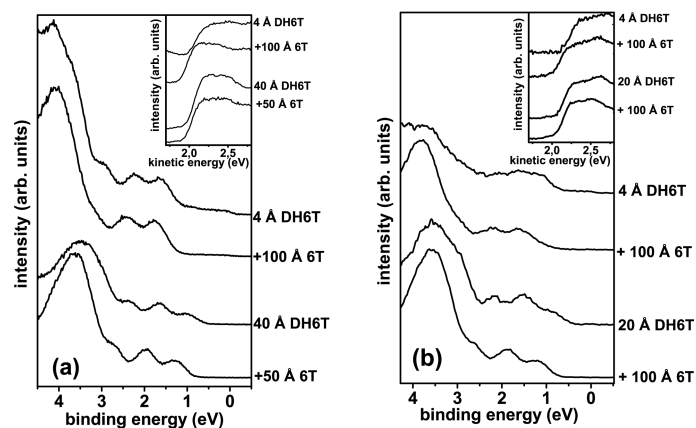


Figure 4.17: UPS spectra of 6T on L1 DH6T (upper plots) and on L2 DH6T (bottom plots) on the substrates (a) Ag(111) and (b) polycrystalline Au. In (b) all spectra are substrate subtracted. The insets display the secondary electron cutoff.

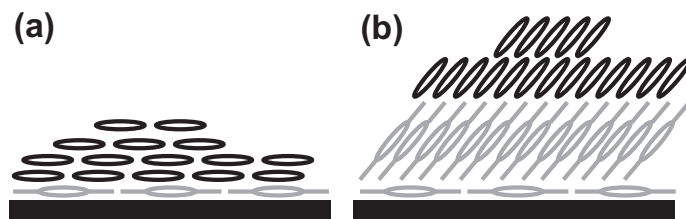


Figure 4.18: Growth model of 6T on (a) monolayer DH6T and (b) multilayer DH6T on a metal substrate.

also 6T is standing as it happens for 6T on pristine metals only for thicker films. Therefore, 6T could be forced to grow in two different orientations by different DH6T pre-coverage thicknesses. For both, application and fundamental physics, it is interesting that the length scale of the process leading from lying to standing 6T could be reduced from hundreds of layers on pristine substrates [86, 87] to just two layers by pre-patterning the substrate with DH6T. But without exact knowledge about the driving force of DH6T to obtain inclined multilayer the discussion about the driving force of 6T on multilayer DH6T to obtain inclined molecules must be very speculative. One may only notice generally that either the inclined phase of DH6T's conjugated backbones or the saturated alkyl chains are responsible for enabling 6T to adopt its bulk phase.

### DH6T/6T/metal

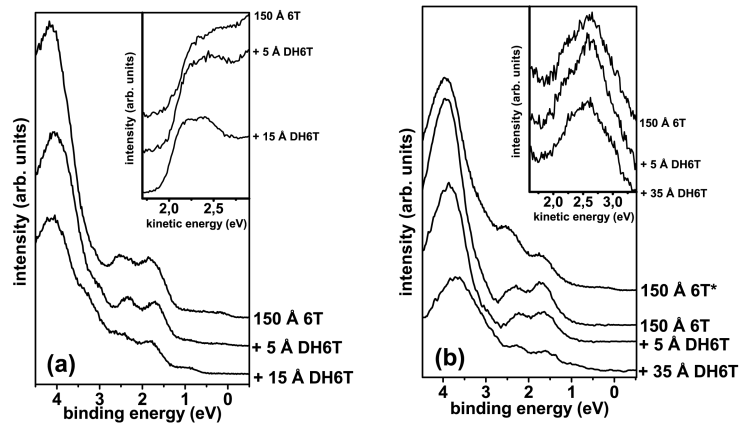


Figure 4.19: UPS spectra of DH6T on multilayer 6T on the substrates (a) Ag(111) and (b) polycrystalline Au. In (b) all spectra except the spectrum labeled 150 Å 6T\* are substrate subtracted. The insets display the secondary electron cutoff.

The investigation of the reversed deposition sequence in order to investigate whether also DH6T exhibited a different growth mode on 6T/metal as on pristine substrates is complicated due to the pronounced island growth of 6T on the used metal substrates. 6T in the nominal monolayer thickness had such large uncovered substrate patches that it was in this particular case senseless to measure this heterostructure. But even a nominal 150 Å 6T film did not lead to a closed organic layer as can be seen in substrate contributions to the 6T spectra in Fig. 4.19 (a) and (b). However, depositing

5 Å DH6T on 150 Å 6T/Ag(111) resulted in a new small peak centered at 0.85 eV BE. This peak is shifted 0.95 eV with respect to 6T HOMO, thus more than the usual difference of 6T and DH6T levels in the same orientation and is so that attributed as the HOMO of standing DH6T molecules. Depositing more DH6T on 150 Å 6T/Ag(111) increased the 0.85 eV peak. For 5 Å DH6T/150 Å 6T/Au no new peak at the low BE side of the 6T HOMO can be resolved, but for higher DH6T coverage standing molecule's features appeared. In all cases the SECO was not changed. These results may lead to the conclusion that DH6T adsorbed on 6T from beginning on in the standing orientation. The HOMO feature of inclined DH6T of 5 Å DH6T/150 Å 6T/Au may be too small for the instrument's resolution or may get lost in the substrate subtracting process. But it can be also the case, that DH6T was adsorbing on pristine substrate patches between the 6T islands. In this case nominal 5 Å DH6T coverage concentrated on free substrate patches were a much higher effective coverage. On the free patches DH6T could grow in the usual lying L1 inclined L2 scheme and the small peak of the 5 Å DH6T/150 Å 6T/Ag(111) was the DH6T L2 peak. Unfortunately, with the data available it is not possible to decide onto a single scenario.

### Discussion of substrate influence

The measurements of DH6T on a variety of substrates have demonstrated that the DH6T conformation and orientation strongly depends on the substrate. At least three polymorphs exist on the five investigated substrates. X-ray diffraction experiments allowed to estimate the unit cell parameters of standing DH6T on lying DH6T on Ag(111). The totally different molecular orientation and conformation on the five substrates with the lying monolayer/standing multilayer mode at metals, the bulk phase on HOPG and a complete altered growth on TTC/Ag(111), allowed to shed light on the interplay of conjugated and unconjugated parts of organic molecules in the growth process on various substrates.

Since molecular growth is a very delicate issue [79–83] it is hard to link cause and impact for a specific growth mode. But some general considerations could be confirmed by the experimental work. The favorable overlap of  $\pi$ -molecular orbitals with metal d-bands could be demonstrated for the lying monolayer of DH6T on metals. The standing orientation dominates for stronger intermolecular  $\pi$ - $\pi$ -overlap, however it could not be clarified why the alkyl substitution of 6T leads to such an abrupt transition. On well defined, weakly interacting substrates, highly ordered organic structures are likely, which could be demonstrated with the assumed band-like behavior of

DH6T/HOPG. But also rather unexpected observations were made: (i) it was expected that DH6T on TTC grows similar to L2 DH6T/Ag(111), (ii) the difference in the amount of lying DH6T layers on the nominally equal Ag(111) crystals surprises. These examples show that the dominant mechanisms of molecular growth, with a huge number of degrees of freedom like orientation, conformation or abrupt changes in growth mode, cannot be resolved easily. However, in the context of molecular growth, in addition to the specific findings concerning DH6T like the unit cell on Ag(111) and the growth modes on the other substrates, some general useful findings were made. An upper limit (0.15 eV) for orientation dependent changes in the polarization energy for organics was found. An explanation for orientation dependent IEs of van der Waals crystals was found. And an approach to control the growth mode of COMs by pre-patterning the substrates with other COMs was demonstrated.

## 4.2 Charge Transfer Complexes

In this section the experimental results of measurements on charge transfer complexes are presented. The section is organized in the following way: First the ability of F4-TCNQ to react with Au surfaces and to pin the energy levels of subsequently deposited organic materials at the interface is demonstrated. By comparing organic materials that form charge transfer complexes with F4-TCNQ (6T and  $\alpha$ -NPD) with one that does not (6P), a dependence of the pinning-behavior on charge transfer complex formation between the organic molecules and the acceptor is excluded. Afterwards results of the weaker acceptors FAQ and TCAQ are discussed in the same context. Norbert Koch took lead in the data analysis for F4-TCNQ and TCAQ. Most data of this section is published in Refs. [173] (F4-TCNQ), [124] (FAQ) and [125] (TCAQ).

### 4.2.1 F4-TCNQ

#### CT between Au and F4-TCNQ

First, the ability of F4-TCNQ to form a CTC with Au is demonstrated. UPS spectra of F4-TCNQ on polycrystalline Au are shown in Fig. 4.20. Depositing 5 Å F4-TCNQ on Au increased  $\phi$  from 5.25 eV (pristine Au) to 5.6 eV (5 Å F4-TCNQ/Au) as revealed by the shift of the secondary electron cutoff shown in Fig. 4.20 (a). In the valence electron region near the Fermi-level [Fig. 4.20 (b)] two new photoemission features appeared after the deposition of 5 Å F4-TCNQ. These are indicated by the shaded areas

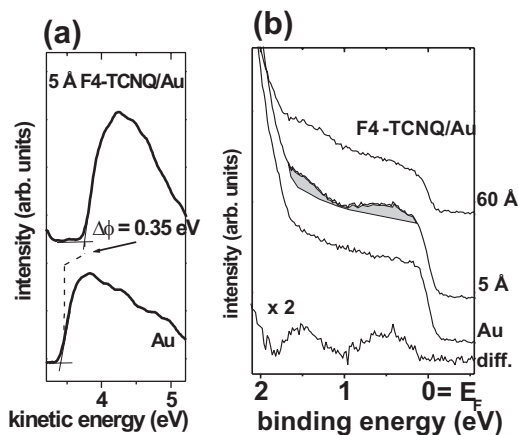


Figure 4.20: (a) SECO region of UPS spectra for pristine Au (bottom) and 5 Å F4-TCNQ/Au (top). (b) Near  $E_F$ -region of UPS spectra of F4-TCNQ/Au; the shaded area indicated the new photoemission features induced by F4-TCNQ. Bottom spectrum (labeled “diff.”) is the difference between 5 Å F4-TCNQ/Au and pristine Au (scaled to the intensity at  $E_F$ ). These UPS spectra were measured at BESSY.

centered at 0.45 eV and 1.45 eV, according to the difference spectrum in Fig. 4.20 (b) where the Au-contribution was subtracted. Further deposition of F4-TCNQ (60 Å) decreased the intensity of these two peaks as the intensity of the metal Fermi-edge. XPS measurements for 5 Å F4-TCNQ/Au [Fig. 4.21] exhibited two peaks in the N(1s) region at 397.8 eV and 399.15 eV BE, both  $\pm 0.05$  eV. Further deposition of F4-TCNQ (60 Å) led to an intensity increase in the higher BE component in the N(1s) spectrum. In addition to these spectroscopic measurements, scanning tunneling microscopy experiments of F4-TCNQ on Au(111) [174] confirm that the acceptor molecules remain intact when adsorbed on Au and adsorb in a planar conformation.

All measured features can be explained by a significant charge transfer between Au and F4-TCNQ. Starting the discussion with the XPS data, the higher BE N(1s) peak is assigned to neutral F4-TCNQ and the lower BE peak to the anion species. This interpretation follows the general rule that negatively charged molecules will exhibit lower binding energies in the core levels than neutral molecules. In previous reports of the unfluorinated parent molecule TCNQ [175, 176] a similar shift occurred in the XPS peaks and was explained in the same way. The third broad component centered at  $400.5 \pm 0.05$  eV BE is attributed to shake-up processes [175, 176]. The dominance of the peak attributed to the charged F4-TCNQ for monolayer coverage



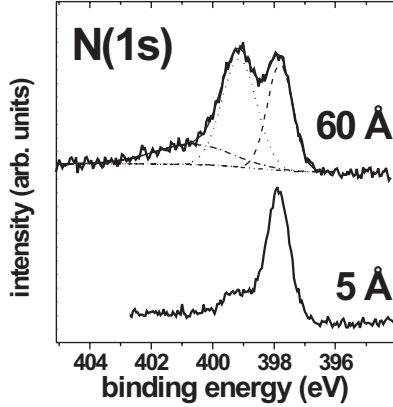


Figure 4.21: N(1s) XPS spectra (photon energy: 630 eV) of 5 Å F4-TCNQ/Au, and 60 Å F4-TCNQ/Au (with peak components and background obtained by the fitting routine).

and the increase of the peak intensity of the neutral F4-TCNQ by increasing the film thickness is consistent with the CT-model: only F4-TCNQ in direct contact with the metal undergoes a CT. The lower BE peak did not vanish for multilayer coverage because of pronounced island growth of F4-TCNQ on Au.

The proposed electron transfer is fully consistent with the appearance of two new peaks close to  $E_F$  in the UPS spectra [Fig. 4.20 (b)]. These peaks are derived from the relaxed HOMO (higher BE) and the stabilized - now (partially) filled - LUMO (lower BE) [28, 60] of the pristine molecule [Fig. 2.5]. After deposition of F4-TCNQ multilayers, in which the molecules are in their neutral state (as also suggested by XPS results), the intensity of these two peaks is reduced [top spectrum in Fig. 4.20 (b)]. Also the shift in the SECO after F4-TCNQ deposition [Fig. 4.20 (a)] points to a CT-type reaction between Au and F4-TCNQ.

For physisorbed molecules a *decrease* in the work function of a metal after molecule deposition is the rule [18, 19]. But in the case of F4-TCNQ  $\phi$  *increased* by 0.35 eV for 5 Å F4-TCNQ coverage. An electron transfer from Au to the organic molecule will lead to negatively charged F4-TCNQ on top of the Au-surface and positive mirror charges in the Au substrate. The result is a dipole with the dipole moment ( $\vec{\mu}$ ) pointing towards the metal surface [Fig. 4.22]. The relation of dipole moment and work function is given by the Helmholtz equation [Eq. 2.6] which is repeated here:

$$\Delta\phi = \frac{q \cdot n_D \cdot \mu_{\perp}}{\varepsilon\varepsilon_0} \quad (4.1)$$

(  $\Delta\phi$ : change in the work function,  $q$ : elementary charge,  $n_D$ : dipole surface density;  $\mu_{\perp}$ : dipole moment perpendicular to the surface,  $\varepsilon$ : dielectric

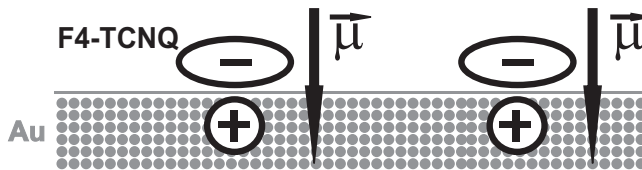


Figure 4.22: Interface dipole ( $\vec{\mu}$ ) established by the CT between F4-TCNQ and Au substrate.

constant,  $\epsilon_0$ : vacuum permittivity). This equation demonstrate that an interface dipole pointing towards the metal surface will increase the substrate work function.

### Energy level tuning with F4-TCNQ

Having established that F4-TCNQ forms a charge transfer complex on the surface of Au, now the influence of different F4-TCNQ pre-coverages ( $\theta_{F4-TCNQ}$ ) on the interface energetics when another organic molecular material is deposited afterwards can be discussed. The first one that is discussed is 6T. Charge transfer complex formation between oligothiophenes and F4-TCNQ is known [177, 178], therefore, this material pair is of direct relevance for testing the concept of energy level bending within the framework of organic electrical doping [65–67].

In Fig. 4.23 (a) the impact of pre-covering Au with 0.15 Å F4-TCNQ on subsequently deposited 150 Å 6T is displayed. In comparison with 6T on pristine Au the spectrum was shifted rigidly to lower binding energies by 0.15 eV. This shift included the peaks originated in the delocalized molecular orbitals HOMO, HOMO-1 and HOMO-2 as the peak attributed to the localized  $\pi$ -electron peak in the 3.5 eV BE region.  $\Delta_h$  for 150 Å 6T/Au was 0.95 eV and for 150 Å 6T/0.15 Å F4-TCNQ/Au 0.80 eV. Increasing  $\theta_{F4-TCNQ}$  up to 5 Å, increased also the rigid shift of molecular levels towards lower BE and led to a hole injection barrier of the 6T overlayer of just 0.30 eV [Fig. 4.23 (b)]. This appears to be the lowest value of  $\Delta_h$  possible for 6T on F4-TCNQ pre-covered Au (at room temperature), as can be inferred from the data summary [Fig. 4.24 (a)]. There also values for the vacuum level shift (relative to the pristine Au surface; i.e., sample work function change)  $\Delta_{vac}$  are shown as function of F4-TCNQ pre-coverage thickness. Both values had a nearly linear dependency on  $\theta_{F4-TCNQ}$  for low pre-coverages (up to 0.5 Å) and stayed (within the error bars) constant for higher F4-TCNQ pre-coverages. Mind that the correlation coefficient between  $\theta_{F4-TCNQ}$  and  $\Delta_h$  on the one side and  $\theta_{F4-TCNQ}$  and  $\Delta_{vac}$  on the other side is not the same.

To elucidate whether charge transfer between F4-TCNQ and the subse-

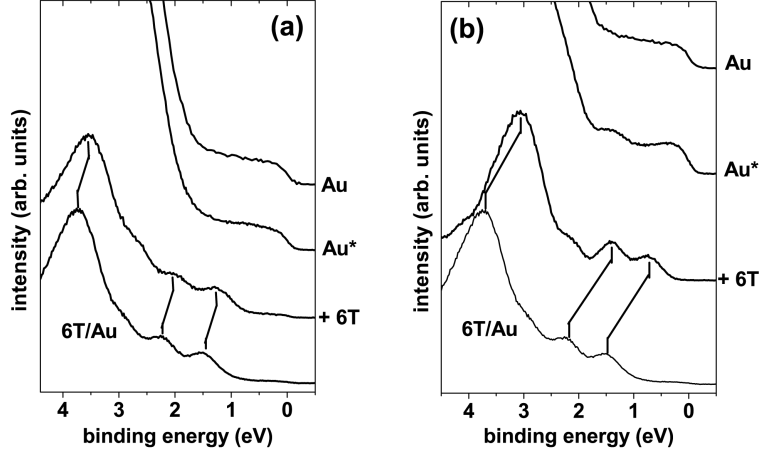


Figure 4.23: (a) UPS spectra of 150 Å 6T on with 0.15 Å F4-TCNQ pre-covered Au, including pristine Au spectrum and F4-TCNQ pre-covered substrate spectrum (spectrum labeled “Au\*”). The spectrum of 150 Å 6T/Au acts as reference. (b) Same as (a) for 5 Å F4-TCNQ pre-coverage.

quently deposited organic material is the dominant mechanism for the observed lowering of  $\Delta_h$  corresponding experiments on 6P have been performed. Charge transfer can be ruled out in this case because of the large ionization energy of 6P of ca. 5.9 eV [18, 19, 60] whereas the electron affinity of F4-TCNQ is only 5.24 eV [67]. However,  $\Delta_h$  was significantly reduced for 6P when F4-TCNQ was pre-adsorbed on Au. The minimum  $\Delta_h = 0.6$  eV was achieved with only 1.5 Å F4-TCNQ/Au [Fig. 4.24 (b)]. Larger F4-TCNQ did not lead to a further decrease of the hole-injection barrier [Fig. 4.24 (b)]. Therefore, the huge reduction of  $\Delta_h$  by 1.2 eV was not due to the formation of an organic charge transfer complex, or electrical doping, but was simply due to the modification of the Au surface by the strong electron acceptor F4-TCNQ.

Results from a third example ( $\alpha$ -NPD) are summarized in Fig. 4.24 (c). This can be seen as an intermediate case, where weaker charge transfer between the two organic materials has been claimed [67], due to the similarity of  $\alpha$ -NPD ionization energy (5.3 eV [18, 67]) and F4-TCNQ electron affinity (5.24 eV). Nevertheless, the dependence of  $\Delta_h$  on F4-TCNQ follows the same trend as for 6P.  $\Delta_h$  decreases from 1.2 eV (pristine Au) to 0.55 eV ( $> 0.6$  Å F4-TCNQ) for  $\alpha$ -NPD films of 50 Å thickness (and remains unchanged for thicker films). This is in between the values of 0.62 eV for 0.5%- and 0.36 eV for 30%-F4-TCNQ-doped  $\alpha$ -NPD [67].

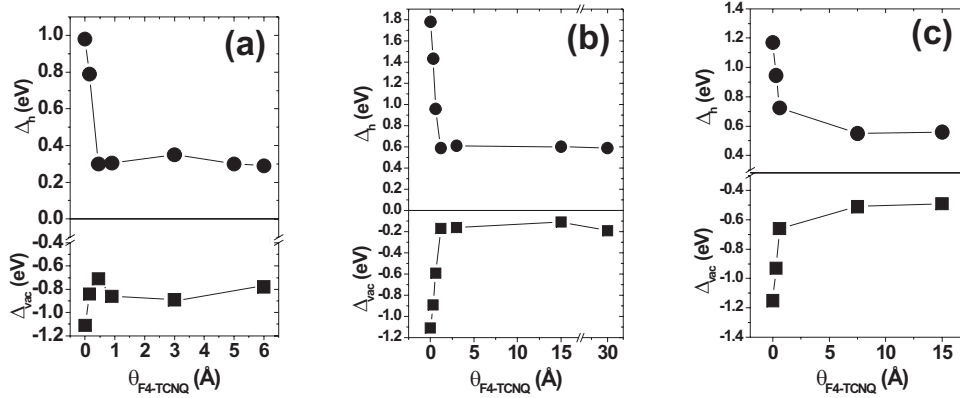


Figure 4.24: Hole-injection barrier ( $\Delta_h$ ) (upper plots) and vacuum level shift relative to pristine Au ( $\Delta_{vac}$ ) for (a) 6T (at 100 Å thickness), (b) 6P (at 80 Å thickness) and (c)  $\alpha$ -NPD (at 50 Å thickness) on F4-TCNQ/Au as function of F4-TCNQ pre-coverage ( $\theta_{F4-TCNQ}$ ). The symbol size corresponds to the experimental error.

From the obtained results it can be concluded that the energy level alignment at organic/metal interfaces in the presence of a strong electron acceptor (in this case F4-TCNQ) is largely determined by the number of acceptor molecules in direct contact to the metal substrate. In Fig. 4.25 the general principle is schematically shown. Low F4-TCNQ pre-coverage (left side) leads to a small interface dipole ( $\vec{\mu}$ ) and therefore to just a small increase in the substrate work function [Equ. 2.6]. However, for sub-monolayer coverage, the surface potential felt by subsequently deposited molecules is an average of local  $\phi$ 's of covered and uncovered substrate patches [98, 179–181]. The energy levels of the second material are then aligned relative to the coverage dependent, area-averaged surface potential established by F4-TCNQ/Au [181]. This is supported by the observation that the width of photoemission features from 6T, 6P, and  $\alpha$ -NPD did not depend on  $\theta_{F4-TCNQ}$ , which would be the case if the spectra arose from the superposition of emission from patches with underlying bare Au and those pre-covered with F4-TCNQ. Energy levels in valence electron region (only the HOMO is shown in Fig. 4.25), are vacuum aligned and the hole injection barrier is rather large. Higher F4-TCNQ pre-coverage leads to a larger  $\vec{\mu}$  and smaller  $\Delta_{vac}$ . Therefore also the hole injection barrier of the subsequently deposited COM is lower than for the smaller  $\theta_{F4-TCNQ}$ .

If charge transfer between the acceptor and the subsequently deposited organic material can be excluded, acceptor pre-coverage is the only parameter

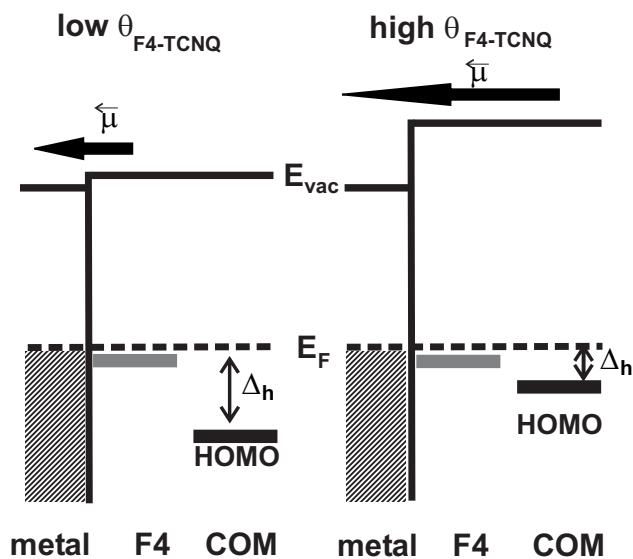


Figure 4.25: Simplified working principle of the energy level tuning mechanism.  $\theta_{F4-TCNQ}$  means F4-TCNQ pre-coverage thickness and F4 means F4-TCNQ. For details see text.

determining  $\Delta_h$ . Once the energy level alignment is defined at the interface, no further shifts of energy levels as a function of film thickness occur (except for photo-hole screening effects). The consequence is that the observation of energy level bending in co-evaporated samples (i.e. doping) probably arises from more acceptor molecules reaching the metal surface as the film thickness is increased. The possibility of extensive F4-TCNQ diffusion through an organic matrix has been reported [67], however, since most organic molecular materials do not follow a layer-by-layer growth mode [79], increasing the film thickness will also increase the amount of acceptor at the metal surface.

The key result is that for all three investigated material-pairs  $\Delta_h$  decreased with increasing F4-TCNQ pre-coverage (on Au) until a “critical coverage” ( $\theta_{crit}$ ) was reached, and remained virtually constant for larger F4-TCNQ. In particular, for 6P [Fig. 4.24 (b)] and  $\alpha$ -NPD [Fig. 4.24 (c)] it appears that in the range of  $\theta_{F4-TCNQ} = 0, \dots, \theta_{crit}$  a linear relationship may exist between  $\Delta_h$  and  $\theta_{F4-TCNQ}$ . The molecular levels of F4-TCNQ are pinned relative to the Au substrate by a charge transfer-type interaction and energy levels of subsequently deposited COMs are aligned to the modified substrate work function. This mechanism undoubtedly holds for material pairs without charge transfer. The situation becomes more complex, if the second organic material has electron donor-type character: molecules may react with F4-TCNQ that is not in contact with Au (multilayer), or may even

interact strongly with Au-F4-TCNQ, resulting in a charge transfer complex with three components. This can explain the unexpected behavior of  $\Delta_{vac}$  for 6T and F4-TCNQ [Fig. 4.24 (a)]: while  $\Delta_h$  was reduced by 0.7 eV,  $\Delta_{vac}$  changed by only 0.3 - 0.4 eV. In contrast, these two values change by the same amount for 6P and  $\alpha$ -NPD [Fig. 4.24 (a) and (b)], corresponding to a rigid shift of all energy levels (including the vacuum level) as function of F4-TCNQ pre-coverage thickness.

## 4.2.2 FAQ

Though F4-TCNQ is a strong acceptor and can tune  $\Delta_h$  of virtually any COM, it has the disadvantage of low molecular weight and low thermal stability. Hence F4-TCNQ is unlikely to be used in a real device and there is need for other acceptors strong enough to undergo a significant charge transfer with noble metal surfaces, such as Ag and Au, with higher molecular weight. FAQ is such a larger acceptor. In this section the ability of FAQ to accept sufficient negative charge from Ag and Au surfaces after adsorption, to allow for hole injection barrier reduction towards another conjugated electroactive organic material is demonstrated.

### CT between FAQ and noble metal substrates

Deposition of FAQ on Au [Fig. 4.26] resulted in the attenuation of Au photoemission features (Fermi-edge and 5d band peaks centered at 3.20 eV and 6.10 eV BE) and the appearance of new photoemission features, derived from molecules, most clearly visible a peak centered at 4.50 eV BE. The experimental curves show the time dependent evolution of the spectrum of a FAQ/Au film with a nominal thickness of 16 Å and the spectrum of the pristine Au as reference. Note that for all FAQ films “film thickness” refers to the nominal mass-thickness (determined by the quartz microbalance) of a molecular film. However, pronounced island-growth can result in large uncovered substrate patches next to comparably “thick” molecular multilayer-islands. With increasing time after deposition of FAQ on Au the contribution from Au to the spectrum is becoming stronger (compare spectra for 10 min and 55 min time laps between film preparation and UPS measurement in Fig. [4.26]). This can be interpreted as an increase of uncovered substrate patches, due to either FAQ desorption or dewetting [85]. Even the spectrum measured only 10 min. after evaporation shows contributions from Au, typical for Frank-van der Merve or Stranski-Krastanov growth mode. In order to obtain the molecule spectrum without the Au-contribution the pristine substrate spectrum was subtracted from the spectrum of FAQ/Au after normalization to

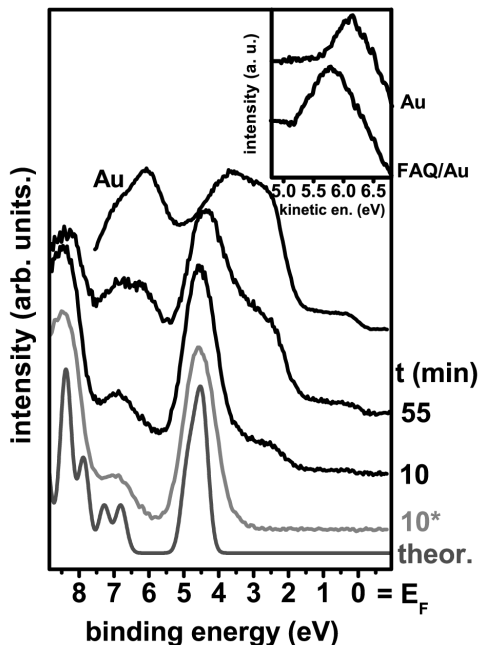


Figure 4.26: UPS spectra ( $h\nu = 45$  eV) of FAQ/Au: pristine Au (top) and chronological evolution of a nominally 16 Å thick FAQ film;  $t$  denotes the time lapsed between evaporation of FAQ on Au and UPS measurements. The spectrum “10\*” is spectrum “10” after Au contribution subtraction. The spectrum “theor.” is the calculated spectrum of FAQ. The inset displays the secondary electron cutoff of pristine Au and FAQ/Au with monolayer coverage.

the intensity at the Fermi-level [Fig. 4.26, spectrum 10\*]. This spectrum resembles closely the theoretical spectrum of a neutral molecule [Fig. 4.26, spectrum theor.]. This last observation would be expected for physisorbed molecules, since in this case the electronic structure of the adsorbed molecule is hardly disturbed by the metal. If molecules were chemisorbed via significant electron transfer from the metal, the electronic structure should change according to the schematic shown in Fig. 2.5. The stabilized former LUMO (now the HOMO of the charged molecule) is shifted to higher binding energies and should occur now in the UPS spectrum as CT-peak just below  $E_F$ . In addition to the stabilization of the LUMO, the CT should also cause an energetic relaxation of the HOMO due to a change in molecular conformation.

However, our measured spectra do not exhibit a clear CT-induced peak near  $E_F$  (even in a close-up of this region). After these simple considerations, one may consequently speculate that FAQ indeed physisorbs on Au. But the BE position of the FAQ HOMO with the onset at 3.10 eV BE is in contradiction to simple physisorption, because the optical energy gap of FAQ (measured with optical absorption spectroscopy in acetone solution) is 2.85 eV. Since the transport gap in the solid-state can be larger by several hundred meV than the optical gap [182], our experimental results indicate

that  $E_F$  is very close to or even at the LUMO of neutral FAQ. This situation is not commonly observed for COMs physisorbed on Au. However, a weak electron transfer from Au to FAQ could explain this behavior, as outlined above. The newly occupied states in the former energy gap lead to the appropriate movement of  $E_F$  relative to the molecular levels. Note that the electron transfer can be very small, inhibiting its observation by UPS. Further support for the proposed electron transfer from Au to FAQ comes from the change of  $\phi$  after deposition of the acceptor. Depositing FAQ in the monolayer region on Au resulted in a decrease of  $\phi$  by 0.40 eV [inset Fig. 4.26]. This value is very small compared to just physisorbed molecular layers, where decreases of typically  $\sim 1$  eV [18, 43, 51, 52] were reported. On the other hand, CT causes an increase in sample work function. Assuming a planar adsorption geometry, the small decrease of  $\phi$  for FAQ/Au is an indication of additional CT-induced dipoles, partially canceling the push-back induced  $\phi$ -decrease. However, the true situation cannot be simply explained by a superposition of push-back and CT-induced dipoles, since the both mechanisms are not decoupled on a molecular scale.

Deposition of FAQ on Ag(111) [Fig. 4.27 (a)] also resulted in an attenuation of metal photoemission features (Fermi-edge and Ag 4d band peaks centered at 4.90 eV and 6.50 eV BE) and the appearance of new photoemission features, derived from molecular orbitals. In contrast to FAQ/Au, no time-dependent spectral changes on the scale of several hours could be observed for FAQ/Ag(111). Apparent molecule-derived photoemission features included a peak centered at 0.95 eV BE and a shoulder at the lower BE side of the metal emission with its onset at 2.35 eV BE [Fig. 4.27 (b)]. With increasing nominal film thickness only intensities but not the position of these two features changed. Even for 48 Å FAQ the Fermi-edge of the substrate was still visible, which can be explained by island or Stranski-Krastanov growth mode. Consequently, the spectrum still contains significant contributions from Ag(111). In order to obtain the spectrum of the adsorbate only, the pristine substrate spectrum was subtracted from the one of 48 Å FAQ/Ag(111) [Fig. 4.27 (a), spectrum 48\*]. This spectrum has some similarity with the substrate-subtracted spectra of FAQ on Au [Fig. 4.26, spectrum 10\*], but there are three obvious differences: (i) the clear appearing of a low BE peak close to  $E_F$  (at 0.95 eV), (ii) the onset of the high intensity peak (2.35 eV) is shifted to lower BE by 0.75 eV compared to FAQ/Au (3.10 eV), and (iii) this peak appears to be composed of at least two components (centered at ca. 3.95 eV and 3.05 eV), while it appears as single component feature for FAQ/Au [centered at 4.55 eV; c.f. Fig. 4.26]. All these differences can be explained by a stronger CT between FAQ and Ag(111) in comparison to FAQ and Au. (i) If more negative charge is transferred from the metal



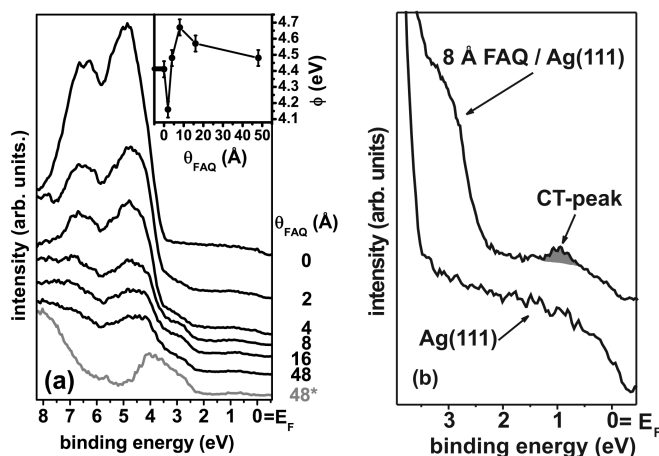


Figure 4.27: (a) UPS spectra ( $h\nu = 45$  eV) of FAQ on Ag(111) for increasing FAQ coverages ( $\theta_{FAQ}$ ). The spectrum “48\*” is the 48 Å FAQ spectrum after Ag-contribution subtraction. Inset: sample work function ( $\phi$ ) as function of FAQ coverage. (b) Close up of the near- $E_F$  region of 8 Å FAQ on Ag(111) with the pristine metal spectrum as reference. The shaded area corresponds to the LUMO-derived CT-peak.

to fill the former LUMO, the resultant CT-peak has more intensity, and was thus clearly observed by UPS [Fig. 4.27 (a)]. (ii) Due to the additional charge on FAQ, conformational rearrangements are more pronounced, leading to a larger relaxation of the HOMO. Consequently, the feature derived from the neutral FAQ HOMO is observed at lower BE. (iii) The apparent broadening (into at least two components) of the neutral FAQ HOMO-derived peak has two reasons: first, a superposition of negatively charged molecular emission from the chemisorbed monolayer, and emission from neutral molecules in multilayers. Second, calculations showed that the first strong photoemission peak [Fig. 4.26] is composed of six almost degenerate molecular orbitals. The CT and the accompanying geometrical changes on FAQ lift this degeneracy, resulting in the observed increased energy splitting of these six orbitals.

The inset in Fig. 4.27 (a) shows the evolution of  $\phi$  as function of nominal coverage. This evolution can be divided into three regions: (i) a decrease of  $\phi$  for coverages  $< 2$  Å, (ii) an increase up to 8 Å, and (iii) a small decrease for higher coverages. The following model is proposed to explain these different regions. Although FAQ on Ag(111) did not show pronounced desorption or dewetting on the time scale of minutes (as did FAQ on Au), FAQ can diffuse during the adsorption process on the metal surface on a much shorter

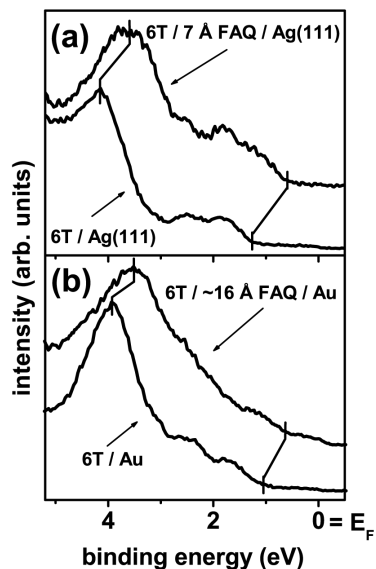


Figure 4.28: Comparison of UPS spectra ( $h\nu = 45$  eV) for 150 Å thick 6T films on FAQ-pre-covered metal surfaces (upper curves) and 6T deposited on pristine (a) Ag(111), and (b) Au. The vertical lines indicate the rigid shift of the spectra including the HOMO-onset and the localized  $\pi$ -orbital maximum (in the 4 eV BE region).

time scale. Nucleation in the low coverage regime possibly occurs at surface defects, such as step edges [183]. At defect sites, the dipole moment resulting from a CT between FAQ and metal needs not necessarily to point in the direction perpendicular to the metal surface. The dipole moments of the dipoles pointing in different direction can cancel each other or can even cause the measured decrease in  $\phi$ . At coverages higher than 2 Å defects are saturated, molecular island growth proceeds on terraces, and  $\phi$  increases as expected for a strong CT. The small decrease for coverages  $> 8$  Å can be due to multilayer formation, where no further charge transfer occurs, but subtle changes in the monolayer conformation may be induced by multilayer over-growth.

### Energy level tuning with FAQ

Fig. 4.28 depicts the results of experiments for 6T deposited on FAQ-pre-covered metal surfaces. Pre-covering Ag(111) with 7 Å FAQ resulted in a rigid shift of 0.60 eV to lower BE of the spectrum for a nominally 150 Å thick 6T film in comparison to 6T (of the same thickness) on pristine Ag(111) [Fig. 4.28 (a)]. The origin of the shift is the modified surface potential of the substrate due to the CT-type interaction. The formation of an organic-organic CT-complex between FAQ and 6T is unlikely, since optical absorption spectra of mixed DH6T and FAQ solutions did not exhibit new CT-induced absorption features below the individual molecules' energy gaps.

Pre-covering Au with FAQ also resulted in a rigid shift to lower BE of the 6T spectrum [Fig. 4.28 (b)], but to a smaller extent (0.40 eV). This is consistent with our proposition that there is a finite CT between FAQ and Au, but smaller than for Ag(111). Note that 6T features on FAQ pre-covered Au are broader compared to 6T on pristine Au. The origin are likely to be surface inhomogeneities (due to the pronounced island growth/dewetting of FAQ/Au) on a mesoscopic scale. In this case the measured spectrum is a superposition of spectra from substrate patches with different local work functions. Due to the island or Stranski-Krastanov growth mode of FAQ the 6T spectrum thus contains contributions from 6T lying directly on the Au surface, 6T on the chemisorbed monolayer FAQ, and on multilayer FAQ.

### 4.2.3 TCAQ

#### CT between TCAQ and Ag(111)

The deposition of 5 Å TCAQ (ca. one monolayer) onto Au resulted in the observation of new photoemission features [Fig. 4.29 (a)], and a decrease of  $\phi$  by 0.5 eV [inset of Fig. 4.29 (a);  $\phi$  of pristine Au: 5.1 eV]. Since the middle spectrum of Fig. 4.29 (a) still contains contributions from the Au substrate, these were subtracted (after normalization to the intensity at  $E_F$ ) to display the features of the organic adlayer only (bottom curve). The peak centered at 3.5 eV binding energy is assigned to be derived from the HOMO of TCAQ. Deposition of TCAQ onto Ag(111) also resulted in new photoemission features [Fig. 4.29 (b)]. After the subtraction of spectral contributions from Ag (bottom curve), the overall spectral shape of TCAQ/Ag closely resembles that of TCAQ/Au. The only significant difference is a rigid shift of 0.2 eV towards higher BE. Noteworthy, the secondary electron cutoff energy position before and after adsorption of TCAQ on Ag did not change [inset Fig. 4.29 (b)], i.e., sample  $\phi$  was constant at 4.45 eV. The ionization energy for both TCAQ/Au and TCAQ/Ag(111) is measured as 7.25 eV.

A rather weak interaction between TCAQ and Au is proposed, since no CT-induced occupied states in the empty energy gap could be observed (c.f. bottom curve Fig. 4.29 (a)). The reduction in sample  $\phi$  after adsorbing molecules is then explained by a decrease of the pristine metal surface dipole due to the electron push-back effect. The absence of changes in  $\phi$  for the deposition of TCAQ on Ag points towards a stronger type of interaction. The fact of constant instead of a decrease suggests an electron transfer from the metal towards the molecular layer. Furthermore, close inspection of the TCAQ/Ag spectrum reveals that a new photoemission feature appears close to  $E_F$  [at 0.7 eV BE in Fig. 4.29 (c)]. This CT-peak is absent for the pristine

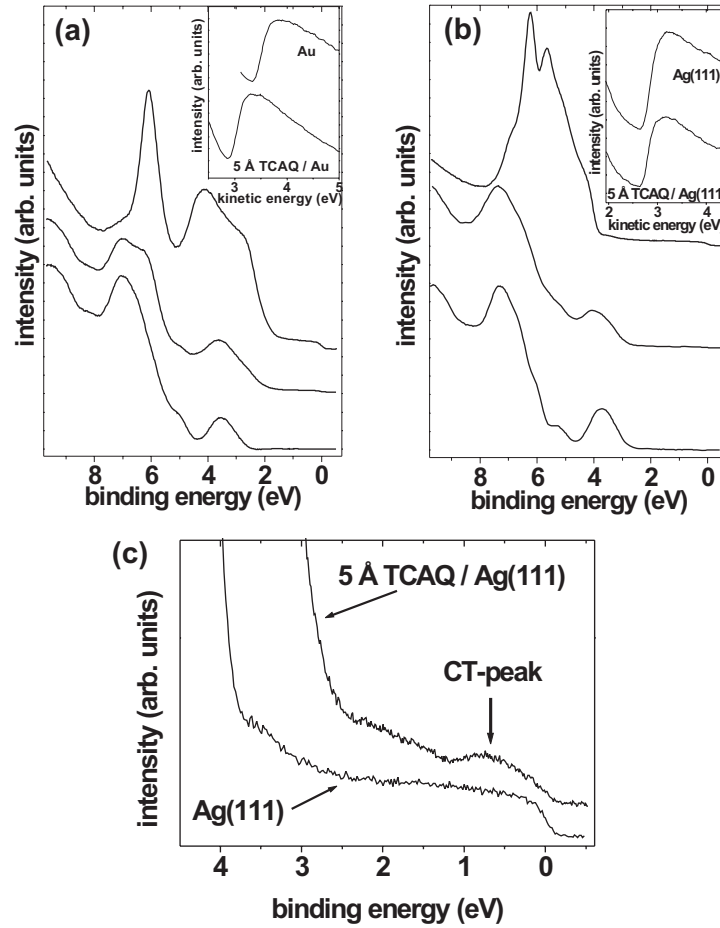


Figure 4.29: (a) UPS spectra of pristine polycrystalline Au (top), 5 Å TCAQ on Au (middle), and the Au-contribution subtracted (bottom). Inset: secondary electron cutoff spectra. (b) UPS spectra of pristine Ag(111) (top), 5 Å TCAQ on Ag(111) (middle), and the Ag-contribution subtracted (bottom). Inset: secondary electron cutoff spectra. (c) Near- $E_F$  UPS spectra of pristine Ag(111) (bottom) and 5 Å TCAQ on Ag(111) (top), displaying the additional photoemission feature (CT-peak) centered at 0.7 eV BE.

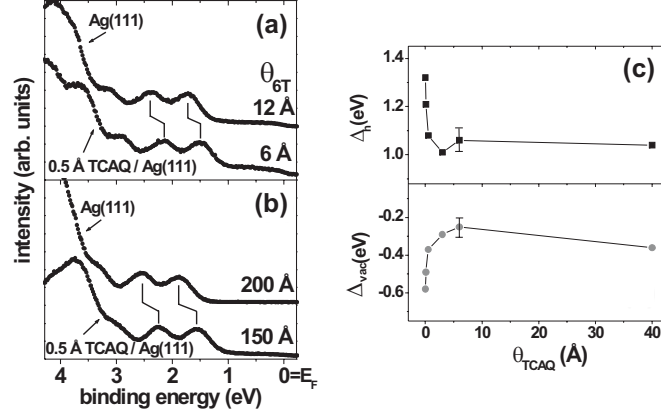


Figure 4.30: Comparison of UPS spectra for (a) low and (b) high 6T coverage ( $\theta_{6T}$ ) on Ag(111) with and without 0.5 Å TCAQ pre-adsorbed (as indicated). (c) Hole injection barrier ( $\Delta_h$ ) and interface dipole relative to pristine Ag(111) ( $\Delta_{vac}$ ) for 25 Å thick 6T films on Ag(111) as function of TCAQ pre-adsorbate coverage ( $\theta_{TCAQ}$ ).

Ag surface, as well as for TCAQ/Au. Consequently, it can be proposed that a TCAQ monolayer adsorbed on Ag undergoes such a charge transfer.

### Energy level tuning with TCAQ

When depositing 6T on top of a monolayer of TCAQ pre-adsorbed on Au, by UPS no differences in the energy level alignment compared to 6T directly deposited onto Au could be observed. For both cases, a  $\Delta_h$  between 6T and Au of 0.75 eV (spectra not shown) was measured, consistent with previous reports on 6T/Au [182]. In contrast, a significantly lower  $\Delta_h$  for 6T on Ag(111) could be found when TCAQ was pre-adsorbed on the metal surface, even in the sub-monolayer range.  $\Delta_h$  for low 6T coverage (Fig. 4.30 (a), top curve) on pristine Ag was 1.30 eV, and only 1.05 eV on Ag with only 0.5 Å TCAQ adsorbed before 6T deposition [Fig. 4.30 (a), bottom curve]. Similarly,  $\Delta_h$  for high 6T coverage [Fig. 4.30 (b), top curve] on pristine Ag was 1.4 eV, and 1.1 eV on Ag with 0.5 Å TCAQ pre-adsorbed [Fig. 4.30 (b), bottom curve]. In all cases, the spectra resemble pristine 6T. The rigid shift of spectra towards higher BE when comparing low and high 6T coverage (0.1-0.2 eV for peak maxima) is due to a decreased screening efficiency of the photo-hole farther away from the metal substrate [138]. Increasing TCAQ pre-coverage did not lead to a significant further decrease of  $\Delta_h$  for 6T on Ag. However, if only

0.1 Å TCAQ were adsorbed onto Ag before 6T deposition,  $\Delta_h$  was reduced by only 0.1 eV relative to 6T on pristine Ag. The values of  $\Delta_h$  for varying TCAQ coverage ( $\theta_{TCAQ}$ ) are summarized in Fig. 4.30 (c) together with  $\Delta_{vac}$ . Both values show the same dependence on the acceptor pre-coverage. Therefore the energy level alignment should only be controlled by the Ag(111)/TCAQ surface reaction and not by an organic/organic CT between TCAQ and 6T [Section 4.2.1]. And indeed, appreciable charge transfer between the electron acceptor TCAQ and the donor 6T can be ruled out. The ionization energy of 6T (measured in the present experiments at 5.2 eV) is much larger than the estimated electron affinity of TCAQ (upper limit: ionization energy (7.25 eV) - optical gap (3.1 eV [184]) = 4.15 eV). Furthermore, if charge transfer were the cause for the lowering of  $\Delta_h$  (in analogy to the reports on “doping” with fluorinated TCNQ [63–65, 67]), this effect would have been observed also for Au as substrate; this was not the case.

### 4.3 Energy level alignment mechanisms

This section is focused on the energy level alignment mechanisms at organic/metal and organic/organic interfaces. The two previously discussed issues –the role of the molecular orientation and the energy level tuning– are combined in one experiment, i.e. the energy levels of DH6T were measured on F4-TCNQ pre-covered metal substrates. A transition from vacuum-level alignment to molecular level pinning - reminiscent of Fermi-level pinning - at the homo-interface between DH6T monolayer and multilayers was observed, which depended on the amount of pre-deposited F4-TCNQ. The results of this section are published in Ref. [185].

#### DH6T/F4-TCNQ/Ag(111)

Fig. 4.31 (a) shows the spectra of a DH6T thickness-dependence series on 1 Å F4-TCNQ pre-covered Ag(111). F4-TCNQ chemisorbed on Ag resulted in three characteristic photoemission features (centered at 0.70 eV, 2.00 eV and 2.80 eV BE), reminiscent of an organic-metal charge transfer type interaction. Sample  $\phi$  was increased by 0.30 eV by F4-TCNQ deposition. The shape of the UPS spectra of DH6T deposited on 1 Å F4-TCNQ/Ag(111) was very similar to the spectra of DH6T on pristine Ag(111) [Fig. 4.1 (b)]. However, all spectra were rigidly shifted by 0.45 eV to lower binding energies, because the DH6T molecular levels were re-aligned to the F4-TCNQ modified substrate surface potential. As for DH6T/Ag(111) with increasing film thickness the spectra were shifted 0.60 eV towards lower BE and the intensity ratio of

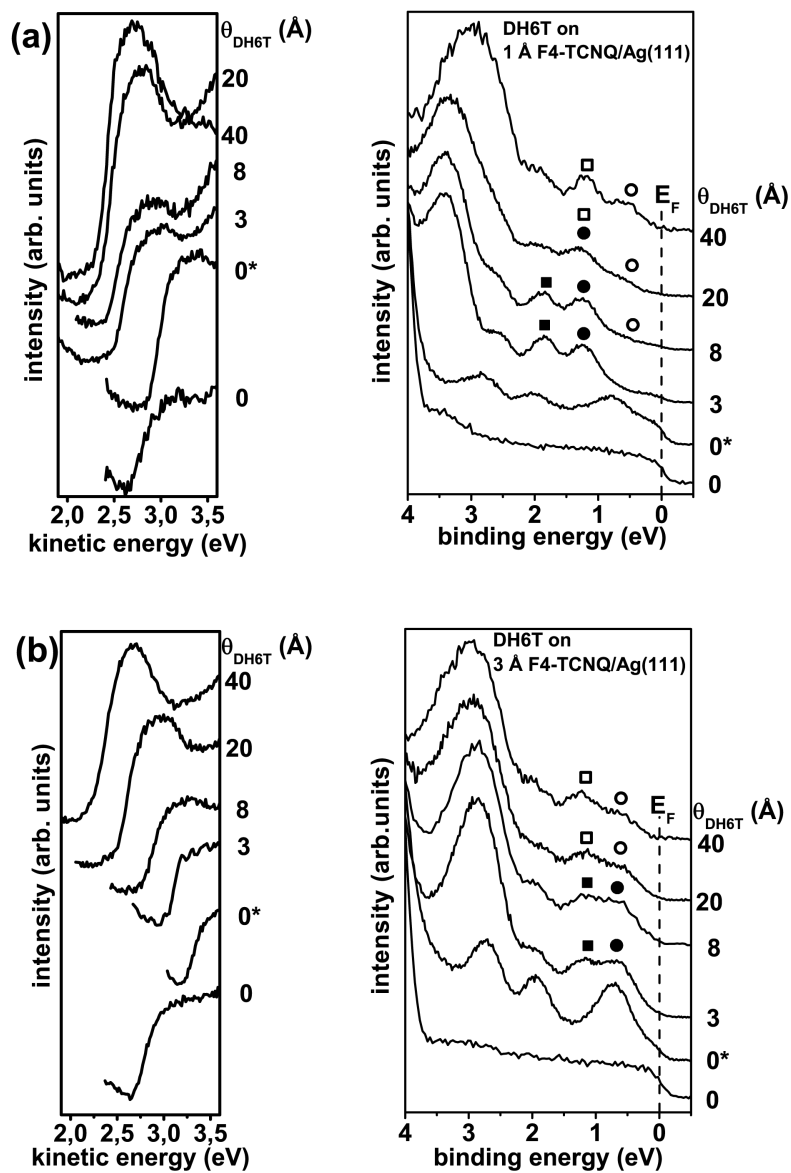


Figure 4.31: (a) SECO (left side) and valence region photoemission spectrum (right side) for DH6T with increasing coverage ( $\theta_{DH6T}$ ) on 1 Å F4-TCNQ pre-covered Ag(111). “0\*” is the spectrum of the F4-TCNQ pre-covered substrate. Closed symbols mark HOMO and HOMO-1 of L1, open symbols mark the same features for L2. (b) Same as (a) for 3 Å F4-TCNQ pre-coverage.

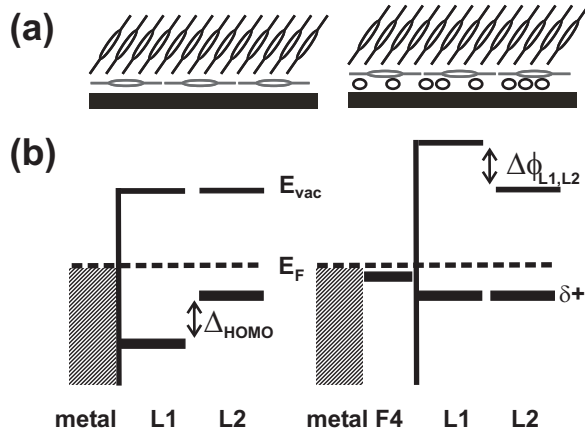


Figure 4.32: (a) Growth model and (b) interface electronic structure model for DH6T/Ag(111) (left side) and DH6T/(*thick*)F4-TCNQ/Ag(111) (right side). L1 indicates monolayer DH6T, L2 multilayer DH6T,  $E_{vac}$  vacuum level,  $E_F$  Fermi-level,  $\Delta\phi_{L1,L2}$  the work function shift,  $\Delta_{HOMO}$  the HOMO shift,  $\delta+$  symbolizes the slightly positively charged pinned HOMO, F4 means F4-TCNQ.

HOMO and HOMO-1 was changed from ca. 1:1 to ca. 1:2. These changes in the position and lineshape of DH6T spectra were already assigned to a transition from flat lying molecules in the monolayer to standing molecules in multilayers. Thus, beyond 3 Å DH6T coverage the formation of multilayers sets in [Fig. 4.31 (a)]. The hole injection barrier for multilayer (e.g., 40 Å) DH6T/Ag(111) was only 0.10 eV. Note that the SECO remained essentially at constant kinetic energy for monolayer and multilayer DH6T coverage.

Pre-covering Ag(111) with 3 Å F4-TCNQ led to a larger increase in sample  $\phi$  (0.60 eV) and hence to a larger rigid shift of molecular levels of subsequently deposited DH6T [Fig. 4.31 (b)] compared to DH6T on 1 Å F4-TCNQ/Ag(111). Now, even for the monolayer DH6T  $\Delta_h$  was only 0.10 eV. Going from L1 to L2 changed the intensity ratio of HOMO and HOMO-1 from almost 1:1 to ca. 1:2, which again is interpreted as evidence for standing molecules. Noteworthy, this change was not accompanied by a further decrease of  $\Delta_h$ . Also the SECO showed a different behavior compared to DH6T on 1 Å F4-TCNQ/Ag(111). Even after monolayer completion the SECO continued to shift towards lower kinetic energies and reached the same position for the multilayers as for the case shown in Fig. 4.31 (a).

Fig. 4.32 summarizes these results. Part (a) indicates the growth model of DH6T on pristine Ag(111) (left side) and DH6T on F4-TCNQ pre-covered Ag(111) (right side). Part (b) displays the corresponding schematic of the



interface electronic structure. Note that the energy level alignment of the DH6T homo-interface L1/L2 was the same for DH6T/Ag(111) and DH6T on 1 Å F4-TCNQ/Ag(111), however, rigidly shifted. For low (or even zero) F4-TCNQ (left side) the vacuum level remained constant at the DH6T homo-interface L1/L2, but the DH6T HOMO shifted towards  $E_F$  ( $\Delta_{HOMO}$ ), i.e., the ionization energy of L2 was smaller than for L1. On the other hand (right side), for F4-TCNQ > 3 Å the hole injection barrier stayed constant at the L1/L2 interface and  $E_{vac}$  exhibited a shift ( $\Delta\phi_{L1,L2}$ ). This behavior is typical for molecular orbital level pinning [55]. It has been suggested that the transition from vacuum level alignment to molecular orbital level pinning occurs when  $\Delta_h$  becomes of the same magnitude as the positive polaron relaxation energy [39, 55, 56]. In this case, charge must be redistributed across the interface, leading to an interface dipole. In other words, the vacuum level is changed but the hole injection barrier stays constant. The measured vacuum level shift  $\Delta\phi_{L1,L2}$  is direct evidence for an interface dipole and the accompanied charge redistribution across the DH6T homo-interface L1/L2. Remarkably, our results demonstrate that the insulating hexyl chains do not obstruct this charge transfer, but allow for thermodynamic equilibrium to be established. Since the hexyl chains are just tilted by 28° with respect to the nearly upright DH6T backbone, the charge has to flow almost along the hexyl long axis.

### DH6T/F4-TCNQ/Au

To extend the above results obtained on the model substrate Ag(111) to a more application relevant substrate, similar experiments were performed using polycrystalline Au as substrate. On pristine Au, DH6T showed the same rigid shift (as on Ag) of molecular levels when going from L1 to L2 [Fig. 4.33 (a), upper part]. For 1 Å F4-TCNQ pre-coverage, already the monolayer DH6T had a hole injection barrier of only 0.10 eV. Multilayer formation did not lead to a further reduction of  $\Delta_h$  [Fig. 4.33 (a), bottom part]. Changes in the hole injection barrier and the vacuum level for lower F4-TCNQ pre-coverages are summarized in Fig. 4.33 (b). The upper part displays  $\Delta_h$  of L1 and L2 of DH6T as function of F4-TCNQ pre-coverage. The bottom part displays the corresponding vacuum level shift ( $\Delta_{vac}$ ) with respect to pristine Au. Multilayer DH6T on pristine Au had the same  $\Delta_{vac}$  as monolayer DH6T, but a decreased  $\Delta_h$ , equivalent to DH6T/Ag(111) [Fig. 4.32 (b)]. For F4-TCNQ pre-covered Au with a monolayer of DH6T,  $\Delta_h$  depended almost linearly on F4-TCNQ until 0.5 Å was reached, leveled off between 0.5 Å and 1 Å and remained constant between 1 and 5 Å. Apparently, also the vacuum level shift was reduced until 1 Å F4-TCNQ pre-coverage and stayed

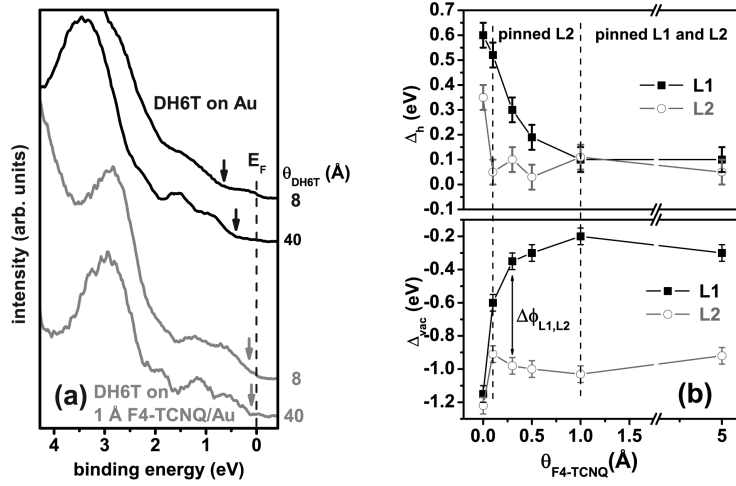


Figure 4.33: (a) UPS spectra of DH6T/Au (upper spectra) and DH6T on 1 Å F4-TCNQ/Au (bottom spectra),  $\theta_{DH6T}$  is the DH6T layer thickness, the arrows indicate the HOMO onset. (b) Hole injection barrier ( $\Delta_h$ ) and vacuum level shift ( $\Delta_{vac}$ ) [referenced to the vacuum level of pristine Au] of a monolayer (filled squares) and multilayers (open circles) DH6T on F4-TCNQ/Au films as function of F4-TCNQ pre-coverage thickness ( $\theta_{F4-TCNQ}$ ).

essentially constant further on. The constant values for the thick DH6T film point to molecular level pinning. In this case the alignment of molecular orbitals is controlled by the molecular polaronic level and not by the effective substrate work function. One can distinguish three different energy level alignment mechanisms regimes of DH6T as function F4-TCNQ pre-coverage: (i) On pristine Au and on 0.10 Å F4-TCNQ/Au the molecular levels of L1 and L2 were vacuum level controlled. (ii) From 0.10 to 1 Å F4-TCNQ/Au L1 was still vacuum level controlled, but L2 was molecular level pinned. (iii) For F4-TCNQ larger than 1 Å both L1 and L2 were pinned.

### Amount of charge transfer

One can estimate the average charge transfer per molecule using the Helmholtz equation [Equ. 2.6]:

$$\Delta\phi_{L1,L2} = \frac{q \cdot n_D \cdot \mu_{\perp}}{\epsilon\epsilon_0} \quad (4.2)$$

and the DH6T molecular area density  $n_M$ . ( $\Delta\phi_{L1,L2}$ : measured change in the work function at the monolayer/multilayer DH6T interface,  $q$ : elementary charge,  $n_D$ : dipole surface density,  $\mu_{\perp}$ : dipole moment perpendicular to

the surface,  $\varepsilon$ : dielectric constant,  $\varepsilon_0$ : vacuum permittivity.)  $\Delta\phi_{L1,L2}$  was measured to be 0.85 eV on both metal substrates. The layer thickness of L2 is known to be 36.5 Å for DH6T/Ag(111) [Sec. 4.1.4], and assumed to be similar for DH6T/Au. For our calculations, half of this value was used to estimate the distance between the charges giving rise to  $\Delta\phi_{L1,L2}$ . For  $\varepsilon$  a value of 3 was chosen, which is a commonly accepted value for conjugated organic materials [182].  $n_M$  was estimated from the crystal structure of L2 DH6T/Ag(111) with  $n_M = 4.20 \times 10^{14} \text{ cm}^{-2}$  [Sec. 4.1.4]. The ratio of  $n_D$  and  $n_M$  gives for the average charge per DH6T molecule in the multilayer 0.02 q. This relatively small value can explain why no new density of states (i.e., corresponding to polaronic levels) was observed close to  $E_F$  by photoemission.

Photoemission results of DH6T/F4-TCNQ/metal heterostructures have shown that for high work function electrodes (in this case metals covered with strong electron acceptors) the positive polaron relaxation energy of multilayer DH6T film is in the range of the DH6T hole injection barrier. In this case, the energy level alignment changes from being vacuum level controlled to molecular orbital level pinning. The measured shift in the vacuum level between monolayer and multilayer DH6T is direct evidence for interface dipoles and for charge transfer between molecular layers. The observed pinning behavior suggests that hexyl chains are not appropriate insulating layers for the use in molecular electronics, and longer chains may be needed.

## 4.4 Bonding Distance

In this section the interplay of bonding distance and electronic interface structure is described. In the first part the electronic structure of interfaces between noble metals and PTCDA are presented and compared with literature XSW-data of bonding distances of PTCDA on these substrates. In the second part the bonding distances of PEN and PFP on Cu(111) are presented. The XSW measurements and data analysis have been made in close collaboration with Alexander Gerlach (Universität Tübingen). The results are published in Refs. [186] (PTCDA) and [187] (PEN and PFP).

### 4.4.1 PTCDA on metals

#### PTCDA as model molecule

An interesting model molecule in the context of bonding distance vs. interface electronic structure is PTCDA. The electronic as well as the geometric structure of PTCDA on different metal substrates has been studied

in detail [188–201]. It is known that PTCDA can react strongly with metals *via* electron transfer [188–191], resulting in anionic molecular species. Despite the manifold possible interactions at the interface, PTCDA multilayers exhibit the same hole injection barrier on a variety of polycrystalline metal substrates, covering a wide range of work functions (ca. 3.7 eV to 5.2 eV). For PTCDA on Mg, In, Sn and Au, [192] as well as for PTCDA on Au and Co, [193] the molecular levels have been investigated by UPS. For PTCDA on Au, Al and Sn the hole injection barriers have been determined from current-voltage measurements in model devices [194]. Structural information for PTCDA adsorbed on single crystalline substrates Au(111), Ag(111) and Cu(111) has been obtained by means of low and high energy electron diffraction, STM and X-ray diffraction [195, 196, 200, 202]. Recent X-ray standing wave studies have shown different adsorption geometries for PTCDA on Au(111) [47], Ag(111) [47–49] and Cu(111) [49]. In addition to different average bonding distances of PTCDA on these metal surfaces, significant deviations from the planar bulk-conformation of the organic molecule were found. To obtain deeper insight in bonding mechanisms at organic/metal interfaces it is necessary to compare these data with the interfacial electronic structure of PTCDA on these three metal substrates. For PTCDA/Ag(111) it is already known that hybridization of unoccupied and occupied molecular orbitals with Ag 4d-bands occurs in the monolayer [188, 203], accompanied by electron transfer from the metal to the molecule. This well characterized system may act as a reference for PTCDA/Au(111), where the bonding is expected to be weaker than on Ag(111) [189, 197, 204] and for PTCDA/Cu(111) [200, 201], where a stronger chemical interaction is expected [49, 205]. UPS measurements on PTCDA/metal interfaces with Au(111), Ag(111) and Cu(111) substrates were performed. These data reveal a correlation between the adsorption geometry and the interface electronic structure, leading to deeper insight into this interesting model system. In addition, the electronic structure of multilayer PTCDA has been measured on each substrate. Despite the remarkable differences in adsorption geometry and interfacial electronic structure for monolayers, the multilayer electronic structure and energy level alignment are virtually identical for all three cases.

### **PTCDA/metals: UPS**

The thickness dependent evolution of the photoemission spectra for PTCDA on the three different (111)-substrates is shown in Figure 4.34.

The deposition of up to 2 Å PTCDA on Au(111) resulted in the attenuation of the Au derived photoemission features and the growth of a shoulder centered at 1.80 eV BE on the low binding energy side of the Au 5d-bands. In

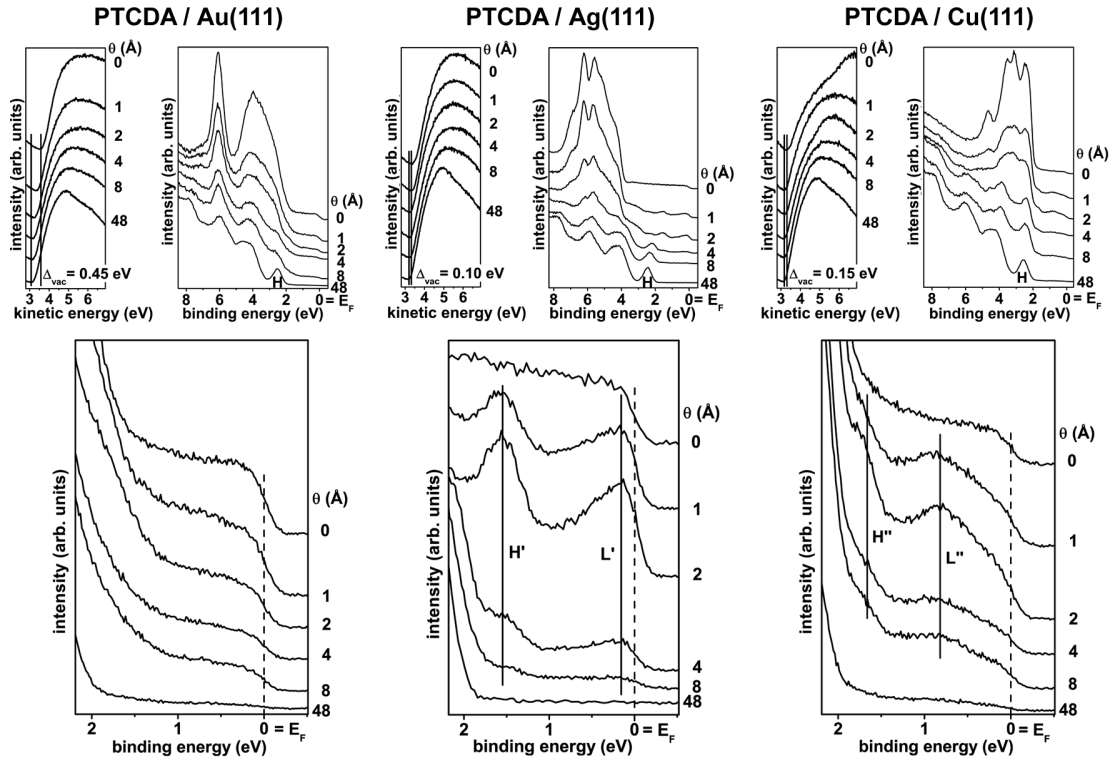


Figure 4.34: Thickness dependent UPS spectra of PTCDA on Au(111), Ag(111) and Cu(111).  $\theta$  denotes the layer thickness. The first row displays in each case the secondary electron cutoff spectra and the survey spectra. H marks in each case the HOMO of multilayer PTCDA. The second row shows the corresponding spectrum in the region close to the Fermi-energy ( $E_F$ ) on an enlarged scale. H' marks the HOMO and L' the LUMO derived interface states in the case of PTCDA/Ag(111), H'' and L'' the same for PTCDA/Cu(111).  $\Delta_{vac}$  denotes the decrease in the vacuum level between the pristine metal and multilayers of PTCDA.

analogy to earlier studies [182, 204], this feature is attributed to the HOMO of PTCDA. No indication for another molecular adsorption-induced photoemission feature close to  $E_F$  was found. Increasing the coverage up to 48 Å led to a continuous shift of this feature to 2.55 eV BE. At this multilayer coverage, the spectrum fully agrees with PTCDA spectra on polycrystalline Au reported previously [182, 193]. For 1 Å PTCDA/Au(111) the sample work function decreased by 0.20 eV compared to pristine Au(111), and by further 0.25 eV at a coverage of up to 48 Å (i.e., -0.45 eV total vacuum level shift).

For the Ag(111) substrate the deposition of 1 Å PTCDA resulted in several new photoemission features; a peak centered at 0.2 eV BE directly below the Fermi-edge of the metal ( $L'$ ) and another peak centered at 1.55 eV BE ( $H'$ ). Increasing the coverage up to 2 Å led to enhanced intensity of both peaks. However, for 4 Å PTCDA coverage the intensity of the two peaks  $L'$  and  $H'$  decreased and a new peak centered at 2.20 eV BE emerged. Increasing the coverage up to the final value of 48 Å led to a shift of this peak to 2.45 eV BE, while the two low BE peaks vanished. For sub-monolayer coverage  $\phi$  decreased by only 0.10 eV and stayed constant for higher coverages.

The deposition of up to 2 Å PTCDA on Cu(111) also resulted in two new photoemission features in the region near to  $E_F$ , i.e. a broad peak centered at 0.80 eV BE ( $L''$ ) and another peak centered at 1.70 eV BE ( $H''$ ). At higher coverages the intensities of these peaks decreased and at 48 Å PTCDA coverage these peaks and the metal Fermi-edge were no longer visible. However, similar to the case of PTCDA/Ag(111) a new peak centered at 2.55 eV BE emerged at multilayer coverage. The work function was decreased by 0.15 eV for a coverage of 1 Å PTCDA and stayed essentially constant for further PTCDA deposition.

The work function at monolayer coverage was 4.75 eV on all three substrates, regardless of the shape of the photoemission spectrum. Depending on the specific growth mode a nominal coverage of 2 to 3 Å corresponds to a nominal monolayer on all three substrates. The HOMO positions of all multilayer samples were virtually identical, with the peaks centered at 2.55 eV BE for PTCDA/Au(111) and PTCDA/Cu(111), and at 2.45 eV BE for PTCDA/Ag(111). Consequently, the PTCDA ionization energies were identical on all three substrates within the error bar of  $\pm 0.05$  eV, namely 6.80 eV on Au(111), 6.85 eV on Ag(111) and 6.75 eV on Cu(111).

### **PTCDA/metals: Bonding types**

In the following the photoemission results will be discussed in the light of previous knowledge about the properties of PTCDA/metal interfaces. Particular relation to recently reported bonding distance values will be made,

which will finally allow to arrive at a comprehensive picture of PTCDA/metal interface energetics.

It has been suggested that the interaction between a conjugated organic molecule and a Au(111) surface should be rather weak [189, 197]. Consequently, no clear signature of molecule-metal reaction-induced peaks within the energy gap region of PTCDA was observed in the spectra of PTCDA/Au(111), even at sub-monolayer coverage [Fig. 4.34]. The shift of the HOMO between monolayer and multilayer of 0.75 eV towards higher binding energies seems unusually large for weakly interacting conjugated organic molecules on metals. Usually, the screening of the photo-hole by the metal charge density results in shifts up to 0.40 eV between mono- and multilayer coverage of molecules on metals [102, 206]. The position of the HOMO in the monolayer (1.80 eV BE) is in good agreement with scanning tunneling spectroscopy (STS) data, where a HOMO position of 1.90 eV BE was measured [197]. In contrast, another STS study found the HOMO centered at 2.18 eV BE for monolayer PTCDA/Au(111) and at 2.32 eV BE for 2-3 layers PTCDA/Au(111) [204]. As an explanation for this discrepancy, different tip-surface interactions and/or tunneling distances were suggested [197]. A monolayer of PTCDA on Au(111) forms well ordered domains with two distinct structures, but only one modification is observed in the second and subsequent layers [207, 208]. A recent STS study of the unoccupied states of PTCDA/Au(111) reported differences in the position of the LUMO of up to 0.35 eV depending on the adsorption domain of PTCDA [209]. The authors suggested hydrogen-bond-mediated intermolecular interaction to be responsible for the different peak positions. By analogy, differences of the same order of magnitude should be possible for occupied states. The area-averaged UPS spectra reveal both peaks, but the peak at higher BE may be masked by the dominant Au 5d emission. However, the differences in the electronic structure of the two monolayer adsorption domains, coupled with the polarization effect of the photo-hole can explain the 0.75 eV shift of the PTCDA HOMO between mono- and multilayer. UPS data of multilayer PTCDA on polycrystalline Au report the HOMO peak centered at 2.60 eV BE [182] or 2.35 eV BE [193], respectively. Considering the structural differences between Au(111) and polycrystalline Au, our value is in good agreement with the literature.

The absence of clear molecule-derived photoemission features in the energy gap region may thus be interpreted as indicative of physisorption of PTCDA on Au(111). However, the small decrease of  $\phi$  by only 0.45 eV induced by a monolayer of PTCDA on Au(111) compared to the pristine substrate may indicate a stronger interaction than only physisorption. The electron push-back effect frequently leads to a larger decrease of  $\phi$  (in the range of 1 eV) for molecules physisorbed on Au surfaces [18, 43]. Molecules

chemisorbed on a metal via electron transfer (from the metal to the molecule) induce an additional contribution to the total interface dipole, which can partially or totally cancel the push back effect [Section 4.2]. If the charge transfer for PTCDA/Au(111) was very small, the experimental observation would merely be limited by the fact that the newly induced density of states is simply too low to be detected [Section 4.2.2]. Moreover, detailed theoretical work for PTCDA/Au(111) suggested significant molecular level broadening and interface electron density rearrangement induced by the metal proximity [92], which could be regarded as another way of describing a “soft” chemisorption process.

PTCDA on Ag(111) exhibits a strong chemical interaction, accompanied by electron transfer from Ag to PTCDA [188, 189]. Following earlier reports, the (sub-)monolayer peaks in the energy gap of PTCDA are assigned to hybrid states of the Ag 4d-bands and the LUMO (now partially filled L’), HOMO (now the H’), and the HOMO-1 states of neutral PTCDA [188, 203]. At elevated temperatures PTCDA/Ag(111) grows in the Stranski-Krastanov mode, but at room temperature the growth becomes more layer-by-layer like [210, 211]. Consequently, these interface states are no longer visible in the UPS signal for higher PTCDA coverages. The LUMO-derived interface peak (L’) is located directly at the Fermi-level, thus a monolayer PTCDA on Ag(111) is metallic [188]. The peak emerging at 2.20 eV BE at a coverage of 4 Å was assigned to the HOMO of neutral molecules [188]. The shift of the HOMO peak to 2.45 eV BE for 48 Å PTCDA coverage can be attributed to different polarization energies of PTCDA for the monolayer and multilayers [204]. The decrease in  $\phi$  between the pristine metal and monolayer PTCDA is much smaller than for PTCDA/Au(111), also indicative of a stronger chemical interaction between the substrate and the adsorbate.

The observation of interface states for a monolayer of PTCDA on Cu(111) shows that strong chemical interaction occurs at this interface. As the behavior of the SECO is similar to PTCDA/Ag(111), significant electron transfer from the metal to the molecule takes place as well. Thus, peak L” is assigned to the (partially) filled LUMO and H” from the HOMO of the neutral PTCDA molecule. However, these interface states of PTCDA on Cu(111) are centered at significantly higher binding energies than for PTCDA/Ag(111). The energetic differences indicate that the hybridization of the molecular levels and the Cu 3d-bands is different from the case of PTCDA/Ag(111). Because the peaks are shifted to higher binding energies, stronger bonding of PTCDA to Cu(111) is likely. For monolayer PTCDA on Cu(111) the LUMO derived interface state (L”) is located clearly below the Fermi-level, i.e., a monolayer of PTCDA on Cu(111) is expected to be semiconducting, in contrast to the metallic molecular layer on Ag(111). Since PTCDA on Cu(111)



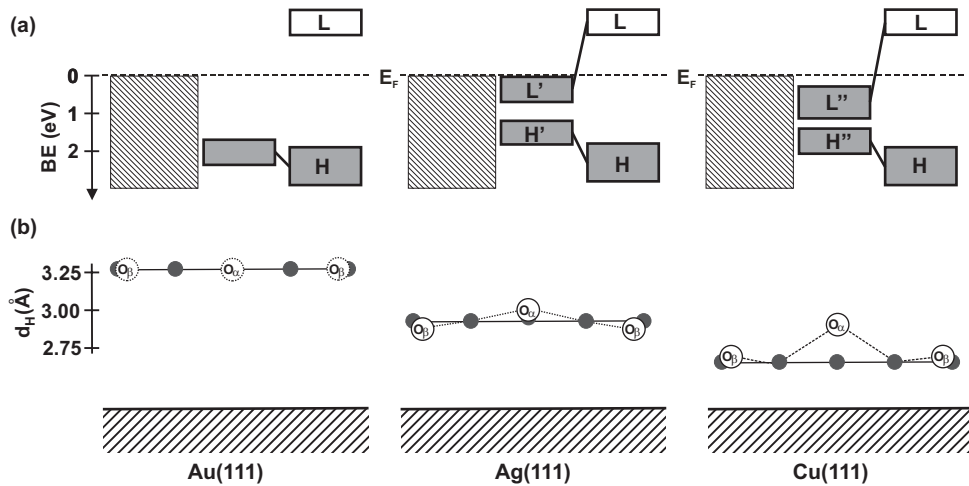


Figure 4.35: (a) Schematic energy level diagram of PTCDA on Au(111), Ag(111) and Cu(111). The shaded area corresponds to the metal electron density, gray bars to occupied and open bars to unoccupied molecular orbitals. From left to right, the pristine metal, the interface region with the LUMO and HOMO derived interface states labeled L' and H' for the metallic case of PTCDA/Ag(111) and L'' and H'' for the semiconductive case of PTCDA/Cu(111) and multilayer PTCDA (H and L) are shown. The positions of the LUMOs are estimated from the transport gap, measured with (inverse) photoemission for PTCDA/Ag [204]. (b) Schematic binding positions of PTCDA on the three different substrates as measured in [47–49]. The position of the oxygen atoms in PTCDA/Au(111) was not measured with XSW, however a merely planar adsorption geometry of PTCDA on Au(111) might be assumed [195, 196].

grows in the Stranki-Krastanov mode [200], the interface state photoemission is not completely attenuated by overlayer material in the UPS spectra at multilayer coverages. The position of the HOMO of the multilayer is consistent with UPS data for PTCDA on polycrystalline Cu, where a HOMO position of 2.47 eV BE has been reported [193].

### Electronic structure vs. bonding distance

The electronic structure of PTCDA on the different substrates exhibits remarkable differences, ranging from “soft” chemisorption (on Au) to strong hybridization of metal bands and molecular orbitals, yielding metallic (on Ag) or semiconducting monolayers (on Cu). It is now interesting to see how these differences in the electronic structure are reflected in the adsorption

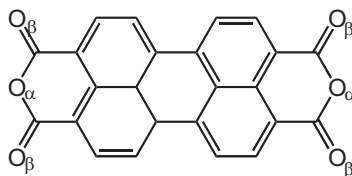


Figure 4.36: Chemical structure of PTCDA, the indices mark the anhydride ( $O_\alpha$ ) and the carboxylic ( $O_\beta$ ) oxygen.

geometry and bonding distance of PTCDA on the metal substrates (or, of course, *vice versa*). In Fig. 4.35 the binding models of PTCDA on Au(111), Ag(111) and Cu(111), are summarized schematically. The PTCDA energy levels in the interface region are compared to those in PTCDA multilayers [Fig. 4.35 (a)] and the binding positions  $d_H$  of the carbon and oxygen atoms of PTCDA adsorbed on the three noble metals [Fig. 4.35 (b)], using the results from X-ray standing wave studies [47–49].

The comparably weak PTCDA/Au(111) interaction is reflected in both the electronic structure and the adsorption geometry. In the UPS spectra no LUMO-derived features appeared at the PTCDA/Au(111) interface. The XSW results report an average carbon bonding distance of PTCDA on Au(111) ( $d_H = 3.27 \text{ \AA}$ ) [47] close to the molecular stacking distance measured in PTCDA single crystals ( $d_{(102)} = 3.22 \text{ \AA}$ ) [212], which also suggests a rather weak interaction. For PTCDA on Ag(111) a clear LUMO-derived peak ( $L'$ ) appeared in the interface region directly at the Fermi-edge, which leads to the metallic character of adsorbed PTCDA. The interface electronic structure of PTCDA on Ag(111) has already been discussed in detail [188, 203] and is presented here for completeness. The adsorption geometry with an average carbon bonding distance of  $d_H = 2.86 \text{ \AA}$  [48, 49] directly supports the strong chemical interaction of PTCDA with Ag(111). In addition, PTCDA on Ag(111) shows a nonplanar adsorption geometry with the carboxylic oxygens ( $O_\beta$ ) [Fig. 4.36] bent towards and the anhydride oxygens ( $O_\alpha$ ) bent away from the metal surface with respect to the carbon plane. On the Cu(111) substrate the higher binding energy of the LUMO-derived peak ( $L''$ ) compared to PTCDA/Ag(111) nicely correlates with the even smaller bonding distance of PTCDA carbons ( $d_H = 2.66 \text{ \AA}$ ) [49]. In addition, the PTCDA bending on Cu is also different than on Ag, as all of the oxygen atoms are bent away from the surface with respect to the PTCDA carbon plane.

Making an overall comparison of UPS and XSW results, a direct correlation between the adsorption geometry and strength of chemical bonding can be found. With increasing metal reactivity the chemical interaction, as revealed by the interfacial electronic structure, increases and the car-

bon bonding distance decreases accordingly. The distortion of the PTCDA molecules in the case of the strongly interacting systems PTCDA/Ag(111) and PTCDA/Cu(111) is not yet fully understood [49]. However, it can be speculated that the different molecular conformations (i.e., bending of the carboxylic oxygens) are directly related to the amount of charge transferred to the molecule, evidenced by the metallic-type monolayer PTCDA on Ag(111) and the semiconducting-type on Cu(111).

### PTCDA energy level alignment

In the following, the properties of the PTCDA multilayers on the three different substrates are considered. The PTCDA ionization energies were found to be essentially the same on all three substrates. Despite the obvious differences in the (sub-)monolayer spectra, the hole injection barriers of multilayer PTCDA on all three substrates are virtually identical. Considering the work functions of PTCDA monolayers on the three substrates this finding is no longer surprising, since  $\phi$  for all three monolayer PTCDA/metal systems is the same. Particularly for PTCDA on Ag(111) and Cu(111) the chemisorbed monolayer must be regarded as a modified metal substrate for the multilayer growth. The molecular levels of PTCDA in the multilayer are thus aligned relative to the modified substrate  $\phi$  as in other organic heterostructures [173, 213]. Therefore the observation of the nearly equal  $\Delta_h$  on all three substrates irrespective of the initial clean metal substrate work function cannot be interpreted in terms of “classical” Fermi-level pinning in the framework of organic/metal interfaces, where besides a small charge transfer between the metal and the adsorbate no chemical interaction occurs and a small density of interface states is able to pin the molecular orbitals [39, 40]. Reactive PTCDA is possibly a special case, which is not compatible with the existing energy level alignment models. The three-layer model (metal – chemisorbed monolayer – multilayer) can explain our findings, but the reason for the constant work functions of the PTCDA/metal systems remains open. An alternative approach may be provided by the calculations of charge neutrality levels (CNL) [92, 214]. In the case of PTCDA on Au(111), a CNL level is found ( $2.45 \pm 0.10$ ) eV above the center of the PTCDA HOMO level, the CNL again is located 0.02 eV above  $E_F$  [92]. This result is in good agreement with our measured HOMO positions. Vázquez et al. [92, 214] stated that changes in the bonding distance of PTCDA and distortions in the range of the experimentally measured values on the different substrates have no significant influence on the position of the CNL. Therefore, also for PTCDA/Ag(111) and PTCDA/Cu(111) the CNL theory should be applicable. It should be interesting to see in future work, whether

this theory, which was designed for chemically weakly interacting systems, can successfully describe the physics at these interfaces.

### **PTCDA summary**

In conclusion, chemisorption with different interaction strength of PTCDA on the substrates Au(111), Ag(111) and Cu(111) could be demonstrated using photoemission. Our results confirm the results from recent XSW studies and reveal the correlation between the strength of the chemical interaction and the average bonding distance. Taking PTCDA on Ag(111) as a reference it can be found that PTCDA binds more strongly to Cu(111) and less strongly to Au(111). For PTCDA on Au(111) no additional states are observed in the energy gap and the bonding distance is large. For PTCDA on Cu(111) the LUMO-derived interface state is more tightly bound than on Ag(111), the bonding distance is smaller, and the PTCDA molecule is distorted. Multiple layers of PTCDA on all three substrates have the same hole injection barrier since the work function of PTCDA monolayers is identical in all three cases.

### **4.4.2 Perfluoropentacene and Pentacene**

So far, in this thesis the emphasis was on the hole injection barrier at organic/metal interfaces, but also the electron injection barrier ( $\Delta_e$ ) has to be considered since the magnitude of the  $\Delta_e$  has the same impact on device performance as the magnitude of  $\Delta_h$  [26, 27]. The determination of  $\Delta_e$  is more demanding than that of  $\Delta_h$ , since inverse photoemission often results in rapid sample damage. Therefore, also in literature, mainly  $\Delta_h$  is discussed in detail. One strategy to decrease  $\Delta_e$  at organic semiconductor/metal interfaces is to increase IE of the organic material. This increase can efficiently be facilitated by the attachment of building blocks with high electron affinity like fluorine to the COM backbone.

Within the simple model of the Schottky-Mott limit,  $\Delta_e$  then decreases for any given metal. However, the invalidity of the Schottky-Mott limit (i.e., vacuum level alignment) for organic/metal interfaces is well documented in literature [18, 19]. The actual value of charge injection barriers is governed by the type and strength of organic/metal interaction, often accompanied by metal surface charge redistribution due to the adsorbed molecules, and also charge transfer between metal and molecules. In addition, charge polarization by surrounding matter, and changes of molecular conformation (possibly inducing/changing intramolecular dipoles) strongly influence charge injection barrier heights. This complex combination of several effects makes it practically impossible to predict injection barriers based on simple mod-

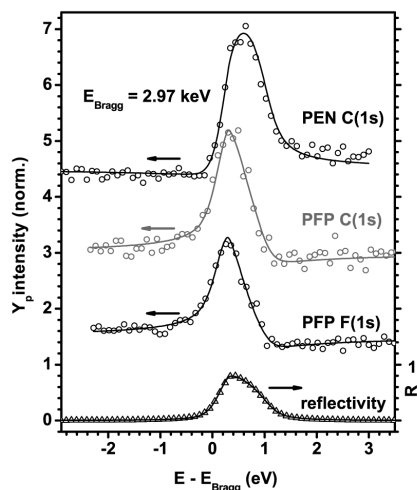


Figure 4.37: X-ray standing wave yield ( $Y_p$ ) for PEN and PFP atoms on Cu(111). The curves are vertically shifted by 1.5 for clearness. In addition the reflectivity signal (R) of the Cu(111) substrate is shown.

els. However, in order to elucidate the influence of the bonding distance on  $\Delta_e$  and  $\Delta_h$   $d_h$  of two prototypical organic semiconductor materials (PEN and perfluorinated PEN) on the Cu(111) surface are compared. The results are discussed in conjunction with results of UPS, XPS, STM and model calculations. The discussion allows to assess hole injection barriers, sample work function changes, strength of organic/metal interaction, molecule-metal bonding distances, molecular distortions and distortion-induced intramolecular dipoles.

### Bonding distances of PEN and PFP on Cu(111)

For PEN and PFP the bonding distances on Cu(111) were measured using XSW, the results are shown in Fig. 4.37. The characteristic variation of the photoelectron yield in the X-ray interference field of the Bragg reflection provides different coherent positions. Retrieving the phase information an (average) C-Cu bonding distance of  $(2.34 \pm 0.02) \text{ \AA}$  for PEN, and  $(2.98 \pm 0.07) \text{ \AA}$  for PFP is found, i.e., a significant difference of  $0.64 \text{ \AA}$  between the two adsorbates. Moreover, the XSW results suggest that the PFP molecule does not adsorb in a coplanar conformation, as would generally be expected due to the weak molecule-metal interaction. The F atoms of PFP reside above the aromatic core, i.e., at a distance of  $(3.08 \pm 0.04) \text{ \AA}$  from the Cu

	<b>PEN</b>	<b>PFP</b>	
	C(1s)	C(1s)	F(1s)
$f_H$	0.55(6)	0.41(7)	0.41(4)
$P_H$	0.120(9)	0.424(35)	0.472(17)
$d_h$	<b>2.34(2) Å</b>	<b>2.98(7) Å</b>	<b>3.08(4) Å</b>

Table 4.3: Coherent fraction ( $f_H$ ), coherent position ( $P_H$ ) and bonding distance ( $d_h$ ) of PEN and PFP on Cu(111).

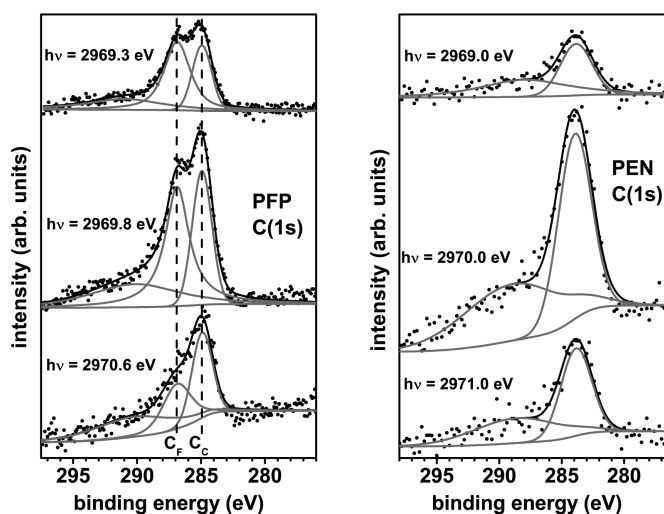


Figure 4.38: C(1s) core level spectra and corresponding fits of PFP and PEN on Cu(111) for different excitation energies ( $h\nu$ ) near the Bragg condition.

surface. The results from the XSW analysis are summarized in Tab. 4.3.

A careful analysis of the XPS spectra of PFP/Cu(111) shows a splitting of the C(1s) peak in three independent peaks [Fig. 4.38]. This finding is consistent with high resolution XPS spectra of PFP/Cu(111) [187]. In Ref. [187] the two components of the C1s core-levels are assigned to the chemically inequivalent C atoms within a molecule, i.e., C atoms directly bound to F (peak centered at 286.90 eV,  $C_F$ ) and those bound just to neighboring C (peak centered at 284.90 eV,  $C_C$ ). The broad component centered at 290.70 eV is assigned to a shake-up of the C(1s) core level.

Unfortunately in the low resolution XPS spectra for the XSW scans the splitting could not be resolved in detail. It was not possible to measure high resolution XPS scans for the XSW analysis, due to the experimental limitation of beam stability, which was not sufficient for long acquisition times.

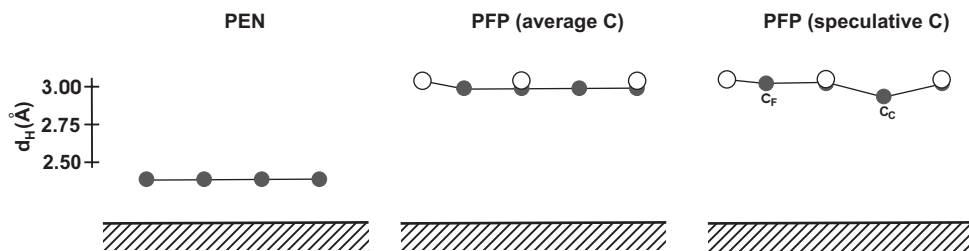


Figure 4.39: Schematic conformation of PEN and PFP on Cu(111) with the molecular long axis parallel to the page (not entire molecule shown). Open circles correspond to F, gray circles to C. For PFP two models exist (see text).

Therefore the value for the C-Cu distance given in Table 4.3 corresponds to the averaged distance of the two carbon species. Note that the coherent fraction for PFP is significantly lower than for PEN. But a few high resolution XPS spectra recorded at different excitation energies near the Bragg-condition allows to resolve the two different carbon species [Fig. 4.38]. The intensity ratio of the two peaks exhibits significant differences for the different photon energies. A comparison with the calculated curves for the XSW yield [Fig. 2.22] led to the assumption that  $C_F$  is at a higher bonding position than  $C_C$ . This finding is corroborated by the higher bonding position of F in comparison to the average bonding position of C. A quantitative estimation is not possible due to the lack of sufficient data even for an analysis in the Argand-diagram [215].

In high resolution XPS scans also the C(1s) core level of monolayer PEN/Cu(111) is split of in two peaks [187]. This split is explained by strong organic/metal chemisorption. In contrast, multilayer PEN on Cu(111) does not show such a split [187]. Unfortunately the peak-split of 0.65 eV is not resolvable in the XPS scans for the XSW analysis due to experimental limitations, here the C(1s) peak can only be fitted with one component in this case [Fig. 4.38]. Again, the broad component at higher BE is assigned to shake-ups. The shape of the C(1s) peak did not change for different excitation energies, suggesting a flat adsorption geometry of PEN on Cu(111). However, since the splitting of the C1s core level is too small to be resolved in XSW scans a non-planar adsorption geometry cannot be ruled out.

The XSW results of PEN and PFP on Cu(111) are summarized in Fig. 4.39. For PFP two models are suggested: The model labeled “average C” is derived quantitatively from the XSW analysis and corresponds to the average carbon bonding distance neglecting the two different carbon species ( $C_C$  and  $C_F$ ). The model labeled “speculative C” corresponds to the more likely case of dif-

ferent bonding positions of  $C_C$  and  $C_F$ . However, a quantitative description of bonding distances is not possible in this case.

As discussed in Section 4.4.1, the bonding distance may act as direct indicator for the strength of chemical bonding at an organic/metal interface. Hence, PEN should be bound stronger to Cu than PFP. Indeed, this assumption is directly evidenced by STM imaging [187, 216]. No stable images of laterally ordered domains could be obtained at room temperature for PFP on Cu(111) [187], whereas for PEN on Cu(119) individual molecules of a disordered phase could be imaged at room temperature, due to strong chemisorption [216]. The distortion of the PFP molecule allows the estimation of the lower limit of the PFP-Cu bonding energy, by comparing the total energies of a molecule in its coplanar to its distorted conformation. Quantum chemical calculations for the “average C” model [187] yield an energy difference of  $\sim 0.11$  eV for these two conformations, which hence corresponds to the minimum of energy gained by the molecular adsorption on the metal surface.

### Adsorption induced dipoles

In the following the impact of the distortion of PFP on Cu(111) on the energy level alignment will be discussed. The deposition of PFP on Cu(111) leads to a decrease of the sample work function by 0.35 eV [187]. This is a comparably small value for a weak chemisorbed COM on a metal. Usually the push-back effect leads to a reduction of  $\phi$  in the order of up to 1 eV [18, 43, 51, 52]. The distortion of PFP leads to an additional internal dipole moment, which has to be considered in the energy level alignment process. The measurement of the different bonding distances of F and C in PFP/Cu(111) allows to calculate the dipole moment of PFP normal to the molecular plane to  $\mu_{\perp} \approx 0.53$  D [187]. Taking into account this dipole induced change of the sample work function ( $\Delta\phi$ ) via the Helmholtz-equation [Equ. 2.6] and using the surface molecular density  $n_m = 7.8 \times 10^{13} \text{ cm}^{-2}$  obtained from STM [187], a value of  $\Delta\phi \approx +0.15$  eV can be obtained for the intramolecular dipole induced work function increase ( $\Delta\phi = +0.16$  eV for a relative dielectric constant  $\varepsilon = 1$ , and  $\Delta\phi = +0.13$  eV for  $\varepsilon = 1.22$  [73] which is the only estimate available at present of for an organic monolayer on a metal surface). This effect counteracts the lowering of  $\phi$  in the weak-adsorption regime. Therefore, the dipole induced by the molecular bending has to be added to the measured  $\Delta_{vac}$  in order to correctly determine the magnitude of the push-back effect at the PFP/Cu(111) interface. Notably, this value of 0.50 eV agrees quantitatively with reported experimental [43] and theoretical [217] values for physisorbed cyclohexane ( $C_6H_{12}$ ) on Cu(111), where



the adsorption-induced lowering of  $\phi$  was exclusively related to Pauli repulsion. This highlights that an adsorption-induced intramolecular dipole (of an initially non-dipolar molecule), even in the regime of supposedly weak organic/metal interaction, has to be taken into account to derive a complete picture of adsorption energetics. Interestingly, while theory quantitatively described the vacuum level changes upon the adsorption of molecules, the bonding distances seem overestimated [43]. Apparently, while details of the adsorption of organic molecules on metal surfaces can coherently be assessed experimentally, a full theoretical description remains a challenging task.

The understanding of the structural and electronic properties of interfaces formed between conjugated organic molecules and metals is a crucial prerequisite for future progress in the fields of organic and molecular electronics. It could be shown that clear-cut correlations exist between strength of molecule/metal interaction, average bonding distances, adsorption-induced molecular conformation changes leading to intramolecular dipoles, organic/metal interface dipoles, and the resulting energy level alignment. The adsorption induced situation for two archetypal organic molecules, i.e., PEN and PFP on Cu(111), showed that even for weak organic/metal interactions (PFP) significant distortions of the molecule occurred. This resulted in adsorption-induced intramolecular dipoles ( $\approx 0.5$  D), which considerably influenced interface energetics, and allowed to derive a coherent physical picture of the investigated interfaces.

# Chapter 5

## Conclusions and Outlook

This work correlated various properties of a number of organic/metal interfaces, in order to gain deeper insight in the mechanisms allowing to control interfacial energy level alignment. For this purpose a variety of experimental techniques was used: With UPS the electronic structure at organic/metal interfaces could be monitored, including the energetic positions of molecular orbital levels and of vacuum levels. Furthermore, information on the morphology and the molecular orientation could be obtained. With XPS chemical shifts could be observed that allowed the identification of chemical reactions at the investigated interfaces. MAES helped to determine the molecular orientation, with XSW information on the bonding distance could be obtained and XRD allowed to assess the crystalline structure of thin organic films. The experimental work was in parts supported by theoretical calculations from collaborators.

The most important interface property for device efficiency in organic electronics is the energy level alignment, since the charge injection barriers at organic/metal interfaces determine the current flow. The energetic position of molecular orbital levels at such interfaces is however governed by the interplay of numerous properties, which have to be carefully correlated in order to gain a thorough understanding of interface energetics. The electronic structure is mainly affected by: (i) interface dipoles resulting from: the electron push back effect, charge transfer between metal and adsorbate and intramolecular dipoles (intrinsic or adsorption induced), (ii) chemical interactions of adsorbates (physisorption vs. chemisorption), (iii) the thin film morphology, (iv) the molecular orientation and conformation and (v) bonding distances of adsorbates. The aim of this thesis was to collect as much knowledge as possible about these points (i) to (v).

With the experiments performed on DH6T it was possible to clearly correlate the molecular orientation to the electronic structure of organic thin

films. It was shown that the lowering of the hole injection barrier by an orientational transition from lying to standing molecules affects all molecular orbitals. It was demonstrated that shifts of the observed magnitude cannot be explained by changes in the polarization energies for different molecular orientations alone. Therefore, a novel concept was established extending the approach of orientation dependent work functions of metal single crystals to the ionization energy of van der Waals crystals. Furthermore the molecular orientation of a COM could be controlled by pre-patterning the metal substrate with another COM.

With the experiments performed on electron acceptors it was possible to correlate an interface charge transfer to an effective substrate work function. This enables energy level tuning of virtually any COM over a large energy range, which enables to control the hole injection barrier of COMs on metals. Moreover, the combination of strong electron acceptors with the orientational change of DH6T at the monolayer/multilayer interface led to insight into energy level alignment mechanisms at organic/organic interfaces, where a thermodynamically driven charge transfer across nominally insulating hexyl changes was demonstrated.

With the experiments on PTCDA a strong correlation between bonding distance and interfacial charge transfer could be established. The XSW-measurements on PEN and PFP allowed to determine adsorption induced intramolecular dipoles also for weakly interacting systems.

With the obtained correlations various unanswered questions on organic/metal interfaces have been addressed. The findings may be helpful on the way to fully understand the interface physics. By an enhanced control over interface properties higher device efficiency in organic electronics may be achieved. Several starting points for future investigations based on this work are evident: One approach could be to find strong acceptors with high thermal stability for energy level tuning, since the acceptors used in this work are either too weak (TCAQ) or thermally too unstable (F4-TCNQ and FAQ) to be used in applications. The control over the molecular orientation by pre-treating the substrates was demonstrated to be another tool to lower charge injection barriers at organic/metal interfaces, since the orientation of 6T was successfully changed by DH6T pre-coverage lowering the 6T hole injection barrier. The mechanisms behind the pre-patterning results are not fully understood yet and should be explored further. The new knowledge generated through this thesis is expected to directly lead to application-oriented progress in the fields of organic and molecular electronics. New device architectures are anticipated, which can pave the way towards high efficiency organic devices on various length-scales via controlled handling of interface properties.

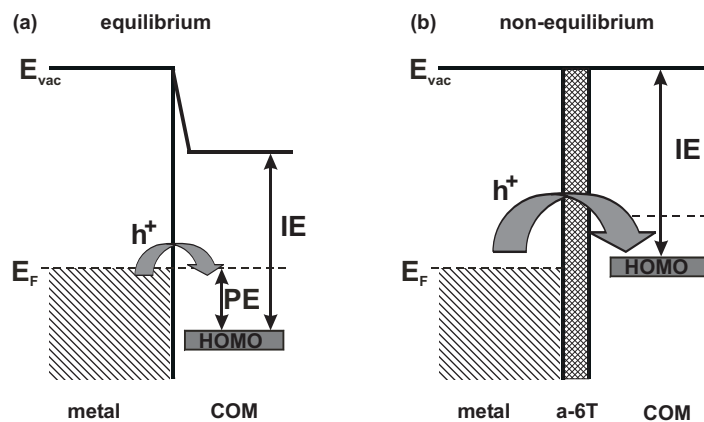


Figure 5.1: Schematic energy level diagram of an organic/metal interface (a) in thermodynamic equilibrium and (b) in thermodynamic non-equilibrium enabled by a spacer layer of alkylated sexithiophene (a-6T). In the equilibrium case, the positive polaron relaxation energy (PE) builds up a barrier for hole ( $h^+$ ) injection from the metal to the HOMO of the COM. In the non-equilibrium case this barrier is reduced to zero and charge can flow unhampered.

A central question that is raised by the results of this work is: Can persistent thermodynamic non-equilibrium at organic/metal interfaces be achieved by specific design, and can this be used to reduce charge carrier injection barriers at organic/metal interfaces below present limits? As a first step it would be necessary for this purpose to extend the work to 6T substituted with longer alkyl chains (e.g., dodecyl) than hexyl, in order to establish an alkyl chain length at which thermodynamic equilibrium across the organic layer can no longer be established by spontaneous charge carrier tunneling processes on practical time scales. It can be expected that sexithiophenes with longer alkyl chains will exhibit a similar growth mode as DH6T. It would be necessary that films of the alkylated 6T exhibit highly ordered layer by layer growth to enable smooth films without pinhole-connections to the substrate. As a next step, further work could be directed towards establishing a reliable mechanism to reduce the hole injection barrier at organic/metal interfaces to virtually zero. For this purpose heterostructures of a low IE COM (e.g. PEN) on top of metals pre-covered with a smooth bilayer of alkyl substituted 6T with the lying monolayer/standing second layer arrangement could be fabricated. If the alkyl chain length is sufficiently high to hamper establishing thermodynamic equilibrium between the metal substrate and PEN, occupied states in the top PEN layer should actually be located above the metal Fermi-energy. This would correspond to a situation far off equilibrium,

and is expected to exhibit interesting charge injection properties [Fig. 5.1]. Moreover, such an ordered organic semiconducting layer separated from a metal substrate by insulating alkyl chains could be used to fabricate field effect transistor structures with yet unprecedented high switching speed and low gate voltages.

# Bibliography

- [1] C. D. Müller, A. Falcou, N. Reckefuss, M. Rojahn, V. Wiederhirn, P. Rudati, H. Frohne, O. Nuyken, H. Becker, and K. Meerholz. Multi-colour organic light-emitting displays by solution processing. *Nature*, 421:829–833, 2003.
- [2] S. R. Forrest. The path to ubiquitous and low-cost organic electronic appliances on plastic. *Nature*, 428:911–918, 2004.
- [3] H. Sirringhaus, N. Tessler, and R. H. Friend. Integrated optoelectronic devices based on conjugated polymers. *Science*, 280:1741–1744, 1998.
- [4] H. Hoppe and N. S. Sariciftici. Organic solar cells: An overview. *J. Mater. Res*, 19:1924–1945, 2004.
- [5] A. Hagfeldt and M. Grätzel. Molecular photovoltaics. *Accounts Chem. Res.*, 33:269–277, 2000.
- [6] P. Peumans, S. Uchida, and S. R. Forrest. Efficient bulk heterojunction photovoltaic cells using small-molecular-weight organic thin films. *Nature*, 425:158–162, 2003.
- [7] Y. Sakamoto, T. Suzuki, M. Kobayashi, Y. Gao, Y. Fukai, Y. Inoue, F. Sato, and S. Tokito. Perfluoropentacene: High-performance p-n junctions and complementary circuits with pentacene. *J. Am. Chem. Soc.*, 126:8138–8140, 2004.
- [8] C. D. Dimitrakopoulos and P. R. L. Malenfant. Organic Thin Film Transistors for Large Area Electronics. *Adv. Mater.*, 14:99–117, 2002.
- [9] G. Horowitz. Organic Field-Effect Transistors. *Adv. Mater.*, 10:365–377, 1998.
- [10] J. R. Sheats, H. Antoniadis, M. Hueschen, W. Leonard, J. Miller, R. Moon, D. Roitman, and A. Stocking. Organic electroluminescent devices. *Science*, 273:884–888, 1996.

- [11] R. H. Friend, R. W. Gymer, A. B. Holmes, J. H. Burroughes, R. N. Marks, C. Taliani, D. D. C. Bradley, D. A. Dos Santos, J. L. Brédas, M. Lögdlund, and W. R. Salaneck. Electroluminescence in conjugated polymers. *Nature*, 397:121–128, 1999.
- [12] S. M. Sze. *Physics of Semiconductor Devices*. John Wiley and Sons, 1981.
- [13] N. W. Ashcroft and N. D. Mermin. *Solid State Physics*. Brooks/Cole Thomson Learning, 2005.
- [14] C. Kittel. *Introduction to Solid State Physics*. John Wiley and Sons, 2004.
- [15] M. Schwoerer and H. C. Wolf. *Organic Molecular Solids*. Wiley-VCH, 2006.
- [16] D. Baeriswyl, D. Campbell, and S. Mazumdar. *Conjugated Conducting Polymers*. Springer-Verlag, Berlin, 1992.
- [17] E. A. Silinsh. *Organic Molecular Crystals*. Springer, Berlin, 1980.
- [18] A. Kahn, N. Koch, and W. Y. Gao. Electronic structure and electrical properties of interfaces between metals and  $\pi$ -conjugated molecular films. *J. Poly. Sci. B*, 41:2529–2548, 2003.
- [19] H. Ishii, K. Sugiyama, E. Ito, and K. Seki. Energy level alignment and interfacial electronic structures at organic/metal and organic/organic interfaces. *Adv. Mat.*, 11:605–625, 1999.
- [20] W. R. Silveira and J. A. Marohn. Microscopic view of charge injection in an organic semiconductor. *Phys. Rev. Lett.*, 93:116104, 2004.
- [21] N. Koch. Organic Electronic Devices and Their Functional Interfaces. *ChemPhysChem*, 8:1438–1455, 2007.
- [22] H. Fukagawa, H. Yamane, T. Kataoka, S. Kera, M. Nakamura, K. Kudo, and N. Ueno. Origin of the highest occupied band position in pentacene films from ultraviolet photoelectron spectroscopy: Hole stabilization versus band dispersion. *Phys. Rev. B*, 73(24):245310, 2006.
- [23] N. Koch, I. Salzmann, R. L. Johnson, J. Pflaum, R. Friedlein, and J. P. Rabe. Molecular orientation dependent energy levels at interfaces with pentacene and pentacenequinone. *Org. Electron.*, 7:537–545, 2006.

- [24] R. Friedlein, X. Crispin, M. Pickholz, M. Keil, S. Stafström, and W. R. Salaneck. High intercalation levels in lithium perylene stoichiometric compounds. *Chem. Phys. Lett.*, 354:389–394, 2002.
- [25] X. T. Hao, T. Hosokai, N. Mitsuo, S. Kera, K. Mase, K. K. Okudaira, and N. Ueno. Electronic density tailing outside pi-conjugated polymer surface. *Appl. Phys. Lett.*, 89:182113, 2006.
- [26] W. R. Salaneck, S. Stafström, and J.-L. Brédas. *Conjugated polymer surfaces and interfaces; electronic and chemical structure of interfaces for polymer light emitting devices*. Cambridge Univ. Press, Cambridge, 1996.
- [27] W. R. Salaneck, K. Seki, A. Kahn, and J.-J. Pireaux, editors. *Conjugated Polymer and Molecular Interfaces: Science and Technology for Photonic and Optoelectronic Applications*. Marcel Dekker, New York, 2001.
- [28] W. R. Salaneck, R. H. Friend, and J. L. Brédas. Electronic structure of conjugated polymers: consequences of electron-lattice coupling. *Phys. Rep.*, 319:231–251, 1999.
- [29] T. Ito, A. Chainani, T. Haruna, K. Kanai, T. Yokoya, S. Shin, and R. Kato. Temperature-dependent luttinger surfaces. *Phys. Rev. Lett.*, 95:246402, 2005.
- [30] N. Koch, A. Vollmer, I. Salzmann, B. Nickel, H. Weiss, and J. P. Rabe. Evidence for temperature-dependent electron band dispersion in pentacene. *Phys. Rev. Lett.*, 96:156803, 2006.
- [31] H. Yamane, S. Kera, K. K. Okudaira, D. Yoshimura, K. Seki, and N. Ueno. Intermolecular energy-band dispersion in PTCDA multilayers. *Phys. Rev. B*, 68:033102, 2003.
- [32] L. Torsi, A. Dodabalapur, L. J. Rothberg, A. W. P. Fung, and H. E. Katz. Intrinsic transport properties and performance limits of organic field-effect transistors. *Science*, 272:1462–1464, 1996.
- [33] W. Brütting, S. Berleb, and A. G. Mückl. Device physics of organic light-emitting diodes based on molecular materials. *Org. Electron.*, 2: 1–36, 2001.
- [34] N. Karl. Charge carrier transport in organic semiconductors. *Synth. Met.*, 133-134:649–657, 2003.



- [35] H. Bäessler. Charge Transport in Disordered Organic Photoconductors a Monte Carlo Simulation Study. *phys. stat. soli. (b)*, 175:15–56, 1993.
- [36] M. Henzler and W. Göpel. *Oberflächenphysik des Festkörpers*. B. G. Teubner Stuttgart, 1994.
- [37] P. S. Davids, I. H. Campbell, and D. L. Smith. Device model for single carrier organic diodes. *J. Appl. Phys.*, 82:6319–6325, 1997.
- [38] M. A. Baldo and S. R. Forrest. Interface-limited injection in amorphous organic semiconductors. *Phys. Rev. B*, 64:085201, 2001.
- [39] N. Koch and A. Vollmer. Electrode-molecular semiconductor contacts: Work-function-dependent hole injection barriers versus fermi-level pinning. *Appl. Phys. Lett.*, 89:162107, 2006.
- [40] H. Fukagawa, S. Kera, T. Kataoka, S. Hosoumi, Y. Watanabe, K. Kudo, and N. Ueno. Role of ionization potential in vacuum-level alignment at organic semiconductors interfaces. *Adv. Mater.*, 19:665–668, 2007.
- [41] X. Crispin, V. Geskin, A. Crispin, J. Cornil, R. Lazzaroni, W. R. Salaneck, and J.-L. Bredas. Characterization of the interface dipole at organic/ metal interfaces. *J. Am. Chem. Soc.*, 124:8131–8141, 2002.
- [42] N. Koch, A. Elschner, J. Schwartz, and A. Kahn. Organic molecular films on gold versus conducting polymer: Influence of injection barrier height and morphology on current–voltage characteristics. *Appl. Phys. Lett.*, 82(14):2281, 2003.
- [43] G. Witte, S. Lukas, P. S. Bagus, and Christof Wöll. Vacuum level alignment at organic/metal junctions: “Cushion” effect and the interface dipole. *Appl. Phys. Lett.*, 87:263502, 2005.
- [44] E. Ito, H. Oji, H. Ishii, K. Oichi, Y. Ouchi, and K. Seki. Interfacial electronic structure of long-chain alkane/metal systems studied by UV-photoelectron and metastable atom electron spectroscopies. *Chem. Phys. Lett.*, 287:137–142, 1998.
- [45] K. Seki, E. Ito, and H. Ishii. Energy level alignment at organic/metal interfaces studied by UV photoemission. *Synth. Met.*, 91:137–142, 1997.
- [46] S. Kera, Y. Yabuuchi, H. Yamane, H. Setoyama, K. K. Okudaira, A. Kahn, and N. Ueno. Impact of an interface dipole layer on molecular level alignment at an organic-conductor interface studied by ultraviolet photoemission spectroscopy. *Phys. Rev. B*, 70:085304, 2004.

- [47] S. K. M. Henze, O. Bauer, T.-L. Lee, M. Sokolowski, and F. S. Tautz. Vertical bonding distances of PTCDA on Au(111) and Ag(111): Relation to the bonding type. *Surf. Sci.*, 601:1566–1573, 2007.
- [48] A. Hauschild, K. Karki, B. C. C. Cowie, M. Rohlfing, F. S. Tautz, and M. Sokolowski. Molecular Distortions and Chemical Bonding of a Large pi-Conjugated Molecule on a Metal Surface. *Phys. Rev. Lett.*, 94:036106, 2005.
- [49] A. Gerlach, S. Sellner, F. Schreiber, N. Koch, and J. Zegenhagen. Substrate-dependent bonding distances of PTCDA: A comparative x-ray standing-wave study on Cu(111) and Ag(111). *Phys. Rev. B*, 75:045401, 2007.
- [50] R. Smoluchowski. Anisotropy of the electronic work function of metals. *Phys. Rev.*, 60:661–674, 1941.
- [51] I. G. Hill, D. Milliron, J. Schwartz, and A. Kahn. Organic semiconductor interfaces: electronic structure and transport properties. *Appl. Surf. Sci.*, 166:354–362, 2000.
- [52] V. De Renzi, R. Rousseau, D. Marchetto, R. Biagi, S. Scandolo, and U. del Pennino. Metal work-function changes induced by organic adsorbates: A combined experimental and theoretical study. *Phys. Rev. Lett.*, 95:046804, 2005.
- [53] J.-L. Bredas, D. Beljonne, V. Coropceanu, and J. Cornil. Charge-Transfer and Energy-Transfer Processes in  $\pi$ -Conjugated Oligomers and Polymers: A Molecular Picture. *Chem. Rev.*, 104:4971–5004, 2004.
- [54] E. Zojer, J. Cornil, G. Leising, and J. L. Brédas. Theoretical investigation of the geometric and optical properties of neutral and charged oligophenylenes. *Phys. Rev. B*, 59:7957–7968, 1999.
- [55] C. Tengstedt, W. Osikowicz, W. R. Salaneck, I. D. Parker, C.-H. Hsu, and M. Fahlman. Fermi-level pinning at conjugated polymer interfaces. *Appl. Phys. Lett.*, 88:053502, 2006.
- [56] P. S. Davids, A. Saxena, and D. L. Smith. Bipolaron lattice formation at metal-polymer interfaces. *Phys. Rev. B*, 53:4823–4833, 1996.
- [57] R. S. Mulliken. Structures of complexes formed by halogen molecules with aromatic and with oxygenated solvents. *J. Am. Chem. Soc.*, 72:600 – 608, 1950.

- [58] C. W. Chu, J. M. E. Harper, T. H. Geballe, and R. L. Greene. Pressure dependence of the metal-insulator transition in tetrathiofulvalinium tetracyanoquinodimethane (TTF-TCNQ). *Phys. Rev. Lett.*, 31: 1491–1494, 1973.
- [59] R. Kumai, Y. Okimoto, and Y. Tokura. Current-Induced Insulator-Metal Transition and Pattern Formation in an Organic Charge-Transfer Complex. *Science*, 284:1645–1647, 1999.
- [60] N. Koch, A. Rajagopal, J. Ghijsen, R. L. Johnson, G. Leising, and J.-J. Pireaux. Bipolaron: The stable charged species in n-doped p-sexiphenyl. *J. Phys. Chem. B*, 104:1434–1438, 2000.
- [61] T. Reda, A. F. Collings, C. Barton, and P. Lukins. Functionalized nanoparticle films with rectifying conduction properties. *J. Phys. Chem. B*, 107:13774–13781, 2003.
- [62] E. F. Aziz, A. Vollmer, S. Eisebitt, W. Eberhardt, P. Pingel, D. Neher, and N. Koch. Localized Charge Transfer in a Molecularly Doped Conducting Polymer. *Adv. Mater.*, 19:3257–3260, 2007.
- [63] J. Blochwitz, M. Pfeiffer, T. Fritz, and K. Leo. Low voltage organic light emitting diodes featuring doped phthalocyanine as hole transport material. *Appl. Phys. Lett.*, 73:729–731, 1998.
- [64] X. Zhou, M. Pfeiffer, J. Blochwitz, A. Werner, A. Nollau, T. Fritz, and K. Leo. Very-low-operating-voltage organic light-emitting diodes using a p-doped amorphous hole injection layer. *Appl. Phys. Lett.*, 78: 410–412, 2001.
- [65] W. Gao and A. Kahn. Controlled p-doping of zinc phthalocyanine by coevaporation with tetrafluorotetracyanoquinodimethane: A direct and inverse photoemission study. *Appl. Phys. Lett.*, 79:4040–4042, 2001.
- [66] J. Blochwitz, T. Fritz, M. Pfeiffer, K. Leo, D. M. Alloway, P. A. Lee, and N. R. Armstrong. Interface electronic structure of organic semiconductors with controlled doping levels. *Org. Electron.*, 2:97–104, 2001.
- [67] W. Gao and A. Kahn. Controlled p doping of the hole-transport molecular material N,N'-diphenyl-N,N'-bis(1-naphthyl)-1,1'-biphenyl-4,4'-diamine with tetrafluorotetracyanoquinodimethane. *J. Appl. Phys.*, 94:359–366, 2003.

- [68] M. Pfeiffer, A. Beyer, T. Fritz, and K. Leo. Controlled doping of phthalocyanine layers by cosublimation with acceptor molecules: A systematic seebeck and conductivity study. *Appl. Phys. Lett.*, 73:3202–3204, 1998.
- [69] B. Maennig, M. Pfeiffer, A. Nollau, X. Zhou, K. Leo, and P. Simon. Controlled p-type doping of polycrystalline and amorphous organic layers: Self-consistent description of conductivity and field-effect mobility by a microscopic percolation model. *Phys. Rev. B*, 64:195208, 2001.
- [70] M. Brinkmann, V. S. Videva, A. Bieber, J. J. Andre, P. Turek, L. Zuppiroli, P. Bugnon, M. Schaer, F. Nuesch, and R. Humphry-Baker. Electronic and structural evidences for charge transfer and localization in iodine-doped pentacene. *J. Phys. Chem. A*, 108:8170–8179, 2004.
- [71] J. Topping. On the Mutual Potential Energy of a Plane Network of Doublets. *Proc. R. Soc. London Ser. A*, 114:67–72, 1927.
- [72] A. Natan, L. Kronik, H. Haick, and R. T. Tung. Electrostatic Properties of Ideal and Non-ideal Polar Organic Monolayers: Implications for Electronic Devices. *Adv. Mater.*, 19:4103–4117, 2007.
- [73] H. Fukagawa, H. Yamane, S. Kera, K. K. Okudaira, and N. Ueno. Experimental estimation of the electric dipole moment and polarizability of titanyl phthalocyanine using ultraviolet photoelectron spectroscopy. *Phys. Rev. B*, 73:041302(R), 2006.
- [74] A. Dodabalapur, L. Torsi, and H. E. Katz. Organic Transistors: Two-Dimensional Transport and Improved Electrical Characteristics. *Science*, 268(5208):270–271, 1995.
- [75] F. Dinelli, M. Murgia, P. Levy, M. Cavallini, F. Biscarini, and D. M. de Leeuw. Spatially correlated charge transport in organic thin film transistors. *Phys. Rev. Lett.*, 92(11):116802, 2004.
- [76] X. L. Chen, A. J. Lovinger, Z. Bao, and J. Sapjeta. Morphological and transistor studies of organic molecular semiconductors with anisotropic electrical characteristics. *Chem. Mater.*, 13(4):1341, 2001.
- [77] P. Sreearunothai, A. C. Morteani, I. Avilov, J. Cornil, D. Beljonne, R. H. Friend, R. T. Phillips, C. Silva, and L. M. Herz. Influence of copolymer interface orientation on the optical emission of polymeric semiconductor heterojunctions. *Phys. Rev. Lett.*, 96(11):117403, 2006.

- [78] H. Sirringhaus, P. J. Brown, R. H. Friend, M. M. Nielsen, K. Bechgaard, B. M. W. Langeveld-Voss, A. J. H. Spiering, R. A. J. Janssen, E. W. Meijer, P. Herwig, and D. M. de Leeuw. Two-dimensional charge transport in self-organized, high-mobility conjugated polymers. *Nature*, 401:685, 1999.
- [79] G. Witte and C. Wöll. Growth of aromatic molecules on solid substrates for applications in organic electronics. *J. Mater. Res.*, 19:1889–1916, 2004.
- [80] S. R. Forrest. Ultrathin organic films grown by organic molecular beam deposition and related techniques. *Chem. Rev.*, 97(6):1793–1896, 1997.
- [81] S. M. Barlow and R. Raval. Complex organic molecules at metal surfaces: bonding, organisation and chirality. *Surf. Sci. Rep.*, 50:201–341, 2003.
- [82] D. E. Hooks, T. Fritz, and M. D. Ward. Epitaxy and molecular organization on solid substrates. *Adv. Mater.*, 13:227, 2001.
- [83] J. Locklin, M. E. Roberts, S. C. B. Mannsfeld, and Z. Bao. Optimizing the thin film morphology of organic field-effect transistors: The influence of molecular structure and vacuum deposition parameters on device performance. *J. Macromol. Sci. Polym. Rev.*, 46:79–101, 2006.
- [84] P.W. Atkins. *Physical Chemistry*. W.H. Freeman & Company, 1982.
- [85] G. Beernink, T. Strunskus, G. Witte, and Ch. Wöll. Importance of dewetting in organic molecular-beam deposition: Pentacene on gold. *Appl. Phys. Lett.*, 85:398–400, 2004.
- [86] C. E. Heiner, J. Dreyer, I. V. Hertel, N. Koch, H.-H. Ritze, W. Widdra, and B. Winter. Anisotropy in ordered sexithiophene thin films studied by angle-resolved photoemission using combined laser and synchrotron radiation. *Appl. Phys. Lett.*, 87(9):093501, 2005.
- [87] G. Yoshikawa, M. Kiguchi, S. Ikeda, and K. Saiki. Molecular orientations and adsorption structures of  $\alpha$ -sexithienyl thin films grown on Ag(110) and Ag(111) surfaces. *Surf. Sci.*, 559:77–84, 2004.
- [88] F. Rosei, M. Schunack, Y. Naitoh, P. Jiang, A. Gourdon, E. Laegsgaard, I. Stensgaard, C. Joachim, and F. Besenbacher. Properties of large organic molecules on metal surfaces. *Prog. Surf. Sci.*, 71:95–146, 2003.

- [89] R. Ruiz, A. C. Mayer, G. G. Malliaras, B. Nickel, G. Scoles, A. Kazimirov, H. Kim, R. L. Headrick, and Z. Islam. Structure of pentacene thin films. *Appl. Phys. Lett.*, 85:4926–4928, 2004.
- [90] B. Servet, G. Horowitz, S. Ries, O. Lagorsse, P. Alnot, A. Yassar, F. Deloffre, P. Srivastava, R. Hajlaoui, P. Lang, and F. Garnier. Polymorphism and charge transport in vacuum-evaporated sexithiophene films. *Chem. Mater.*, 6:1809, 1994.
- [91] K. Ihm, B. Kim, T.-H. Kang, K.-J. Kim, M. Ho Joo, T. H. Kim, S. S. Yoon, and S. Chung. Molecular orientation dependence of hole-injection barrier in pentacene thin film on the au surface in organic thin film transistor. *Appl. Phys. Lett.*, 89:033504, 2006.
- [92] H. Vázquez, R. Oszwaldowski, P. Pou, J. Ortega, R. Pérez, F. Flores, and A. Kahn. Dipole formation at metal/PTCDA interfaces: Role of the Charge Neutrality Level. *Europhys. Lett.*, 65:802–808, 2004.
- [93] A. Gerlach, F. Schreiber, S. Sellner, H. Dosch, I. A. Vartanyants, B. C. C. Cowie, T.-L. Lee, and J. Zegenhagen. Adsorption-induced distortion of  $F_{16}CuPc$  on Cu(111) and Ag(111): An x-ray standing wave study. *Phys. Rev. B*, 71:205425, 2005.
- [94] C. Stadler, S. Hansen, A. Schöll, T.-L. Lee, J. Zegenhagen, C. Kumpf, and E. Umbach. Molecular distortion of NTCDA upon adsorption on Ag(111): a normal incidence x-ray standing wave study. *New J. Phys.*, 9:50, 2007.
- [95] H. Yamane, Y. Yabuuchi, H. Fukagawa, S. Kera, K. K. Okudaira, and N. Ueno. Does the molecular orientation induce an electric dipole in cu-phthalocyanine thin films? *J. Appl. Phys.*, 99:093705, 2006.
- [96] R. Magnee, Z. Mekhalif, C. Doneux, A.-S. Duwez, C. Gregoire, J. Riga, J. Delhalle, and J.-J. Pireaux. On the impact of electron spectroscopies (versus optical techniques) to study organized organic layers and their interfaces. *J. Electron Spectrosc. Relat. Phen.*, 88-91:855–860, 1998.
- [97] N. Koch. Energy levels at interfaces between metals and conjugated organic molecules. *J. Phys.: Condens. Matter*, 20:184008, 2008.
- [98] M. Cardona and L. Ley, editors. *Photoemission in Solids I*, volume 26 of *Topics in Applied Physics*. Springer, Berlin, 1978.

- [99] F. J. Himpsel. Angle-resolved measurements of the photoemission of electrons in the study of solids. *Ad. Phys.*, 32:1–51, 1983.
- [100] S. Hüfner. *Photoelectron Spectroscopy*, volume 82 of *Solid-State Sciences*. Springer, 1995.
- [101] D. Cahen and A. Kahn. Electron Energetics at Surfaces and Interfaces: Concepts and Experiments. *Adv. Mater.*, 15:271–277, 2003.
- [102] N. Koch, G. Heimel, J. Wu, E. Zojer, R. L. Johnson, J.-L. Brédas, K. Müllen, and J. P. Rabe. Influence of molecular conformation on organic/metal interface energetics. *Chem. Phys. Lett.*, 413:390–395, 2005.
- [103] N. Koch, A. Vollmer, S. Duhm, Y. Sakamoto, and T. Suzuki. The Effect of Fluorination on Pentacene/Gold Interface Energetics and Charge Reorganization Energy. *Adv. Mater.*, 19:112–116, 2007.
- [104] N. E. Gruhn, D. A. da Silva Filho, T. G. Bill, M. Malagoli, V. Coropceanu, A. Kahn, and J.-L. Bredas. The Vibrational Reorganization Energy in Pentacene: Molecular Influences on Charge Transport. *J. Am. Chem. Soc.*, 124:7918–7919, 2002.
- [105] H. Yamane, S. Nagamatsu, H. Fukagawa, S. Kera, R. Friedlein, K. K. Okudaira, and N. Ueno. Hole-vibration coupling of the highest occupied state in pentacene thin films. *Phys. Rev. B*, 72:153412, 2005.
- [106] Y. Harada, S. Masuda, and H. Ozaki. Electron spectroscopy using metastable atoms as probes for solid surfaces. *Chem. Rev.*, 97(6):1897–1952, 1997.
- [107] K. Ohno, H. Mutoh, and Y. Harada. Study of electron distributions of molecular orbitals by penning ionization electron spectroscopy. *J. Am. Chem. Soc.*, 105:4555–4561., 1983.
- [108] M Birkholz. *Thin Film Analysis by X-Ray Scattering*. Wiley-VCH Verlag GmbH, 2006.
- [109] M Tolan. *X-ray Scattering from Soft-Matter Thin films*. Springer, 1999.
- [110] B. E. Warren. *X-Ray Diffraction*. Dover Publications Inc., 1990.
- [111] H. Kiessig. Interferenz von Röntgenstrahlen an dünnen Schichten. *Ann. Phys.*, 402:769 – 788, 1931.

- [112] F. Schreiber and A. Gerlach. Surface Structure Determination with X-ray Standing Waves – A short Tutorial. <http://www.soft-matter.uni-tuebingen.de>, 2006.
- [113] J. Zegenhagen. Surface structure determination with X-ray standing waves. *Surf. Sci. Rep.*, 18:202–271, 1993.
- [114] D. P. Woodruff, B. C. C. Cowie, and A. R. H. F. Ettema. Surface structure determination using x-ray standing waves: a simple view. *J. Phys.-Condens. Matter*, 6:10633–10645, 1994.
- [115] M. A. Loi, E. Da Como, F. Dinelli, M. Murgia, R. Zamboni, F. Biscarini, and M. Muccini. Supramolecular organization in ultra-thin  $\alpha$ -sexithiophene on silicon dioxide. *Nature Mater.*, 4:81, 2005.
- [116] G. Horowitz, F. Kouki, A. El Kassmi, P. Valat, V. Wintgens, and F. Garnier. Structure-dependent fluorescence in sexithiophene single crystals. *Adv. Mater.*, 11:234, 1999.
- [117] G. Horowitz, B. Bachet, A. Yassar, P. Lang, F. Demanze, J.-L. Fave, and F. Garnier. Growth and Characterization of Sexithiophene Single Crystals. *Chem. Mat.*, 7:1337–1341, 1995.
- [118] D. Fichou. Structural order in conjugated oligothiophenes and its implications on opto-electronic devices. *J. Mater. Chem.*, 10:571 – 588, 2000.
- [119] C. D. Dimitrakopoulos, B. K. Furman, T. Graham, S. Hegde, and S. Purushothaman. Field-effect transistors comprising molecular beam deposited  $\alpha,\omega$ -di-hexyl-hexathienylene and polymeric insulator. *Synth. Met.*, 92:47–52, 1998.
- [120] M. Halik, H. Klauk, U. Zschieschang, G. Schmid, S. Ponomarenko, S. Kirchmeyer, and W. Weber. Relationship between molecular structure and electrical performance of oligothiophene organic thin film transistors. *Adv. Mat.*, 15:917–922, 2003.
- [121] F. Garnier, A. Yassar, R. Hajlaoui, G. Horowitz, F. Deloffre, B. Servet, S. Ries, and P. Alnot. Molecular engineering of organic semiconductors: design of self-assembly properties in conjugated thiophene oligomers. *J. Am. Chem. Soc.*, 115:8716–8721, 1993.
- [122] L. Rossi, G. Lanzani, and F. Garnier. Charged photoexcitations in thiophene-based molecular semiconductors. *Phys. Rev. B*, 58:6684–6687, 1998.



- [123] J. Ackermann, C. Videlot, P. Raynal, A. El Kassmi, and P. Dumas. Effect of end-substitution of hexyl chains on the growth and electrical properties of quaterthiophene thin films. *Appl. Surf. Sci.*, 212-213: 26–32, 2003.
- [124] S. Duhm, H. Glowatzki, V. Cimpeanu, J. Klankermayer, J. P. Rabe, R. L. Johnson, and N. Koch. Weak charge transfer between an acceptor molecule and metal surfaces enabling organic/metal energy level tuning. *J. Phys. Chem. B*, 110(42):21069–21072, 2006.
- [125] N. Koch, S. Duhm, J. P. Rabe, S. Rentenberger, R. L. Johnson, J. Klankermayer, and F. Schreiber. Tuning the hole injection barrier height at organic/metal interfaces with (sub-) monolayers of electron acceptor molecules. *Appl. Phys. Lett.*, 87:101905, 2005.
- [126] C.D. Dimitrakopoulos and P.R.L. Malenfant. Organic thin film transistors for large area electronics. *Adv. Mater.*, 14(2):99–117, 2002.
- [127] T. W. Kelley, P. F. Baude, C. Gerlach, D. E. Ender, D. Muyres, M. A. Haase, D. E. Vogel, and S. D. Theiss. Recent progress in organic electronics: Materials, devices, and processes. *Chem. Mater.*, 16(23): 4413–4422, 2004.
- [128] Y.-Y. Lin, D.J. Gundlach, S.F. Nelson, and T.N. Jackson. Stacked pentacene layer organic thin-film transistors with improved characteristics. *IEEE Electron Device Lett.*, 18(12):606–608, 1997.
- [129] S. Lee, B. Koo, J. Shin, E. Lee, H. Park, and H. Kim. Effects of hydroxyl groups in polymeric dielectrics on organic transistor performance. *Appl. Phys. Lett.*, 88:162109, 2006.
- [130] Y. Inoue, Y. Sakamoto, T. Suzuki, M. Kobayashi, Y. Gao, and S. Tokito. Organic thin-film transistors with high electron mobility based on perfluoropentacene. *Jpn. J. Appl. Phys.*, 44:3663–3668, 2005.
- [131] N. Koch, E. Zojer, A. Rajagopal, J. Ghjisen, R. L. Johnson, G. Leising, and J.-J. Pireaux. Electronic properties of the interfaces between the wide bandgap organic semiconductor para-sexiphenyl and samarium. *Adv. Funct. Mater.*, 11:51–58, 2001.
- [132] Y. Yamamoto, H. Ohara, K. Kajikawa, H. Ishii, N. Ueno, K. Seki, and Y. Ouchi. Differential thermal analysis and ultraviolet photoemission study on the surface freezing effect of n-alkane. *J. Electron Spectrosc. Relat. Phenom.*, 103:555–558, 1999.

- [133] J. Weckesser, D. Fuhrmann, K. Weiss, C. Wöll, and N. V. Richardson. Photoemission from long chain alkanes adsorbed on a metal surface and the electronic structure of trans-polyethylene (CH<sub>2</sub>)<sub>n</sub>. *Surf. Rev. Lett.*, 4:209–218, 1997.
- [134] M. Yamamoto, Y. Sakurai, Y. Hosoi, H. Ishii, E. Ito, K. Kajikawa, Y. Ouchi, and K. Seki. Physisorption of a long-chain n-alkane on Ag(111) surface: an infra-red reflection absorption spectroscopic study. *Surf. Sci.*, 427-428:388–392, 1999.
- [135] R. L. Johnson and J. Reichardt. FLIPPER II – a new photoemission system in HASYLAB. *Nucl. Instrum. Methods Phys. Res.*, 208:791–796, 1983.
- [136] A. Vollmer, O. D. Jurchescu, I. Arfaoui, I. Salzmann, T. T. M. Palstra, P. Rudolf, J. Niemax, J. Pflaum, J. P. Rabe, and N. Koch. The effect of oxygen exposure on pentacene electronic structure. *Eur. Phys. J. E*, 17:339–343, 2005.
- [137] H. Yamane, H. Fukagawa, S. Nagamatsu, M. Ono, S. Kera, K. K. Okudaira, and N. Ueneo. Direct Observation of HOMO-Hole/Vibration Coupling in Pentacene Thin Films by Means of High-Resolution Ultraviolet Photoelectron Spectroscopy. *IPAP Conf. Series*, 6:19–22, 2005.
- [138] A. C. Dürr, N. Koch, M. Kelsch, A. Rühm, J. Ghijsen, R. L. Johnson, J.-J. Pireaux, J. Schwartz, F. Schreiber, H. Dosch, and A. Kahn. Interplay between morphology, structure, and electronic properties at diindenoperylene-gold interfaces. *Phys. Rev. B*, 68:115428, 2003.
- [139] S. Schiefer, M. Huth, A. Dobrinevski, and B. Nickel. Determination of the crystal structure of substrate-induced pentacene polymorphs in fiber structured thin films. *J. Am. Chem. Soc.*, 129(34):10316–10317, 2007.
- [140] M. J. Frisch, G. W. Trucks, H. B. Schlegel, G. E. Scuseria, M. A. Robb, J. R. Cheeseman, J. A. Montgomery, Jr., T. Vreven, K. N. Kudin, J. C. Burant, J. M. Millam, S. S. Iyengar, J. Tomasi, V. Barone, B. Mennucci, M. Cossi, G. Scalmani, N. Rega, G. A. Petersson, H. Nakatsuji, M. Hada, M. Ehara, K. Toyota, R. Fukuda, J. Hasegawa, M. Ishida, T. Nakajima, Y. Honda, O. Kitao, H. Nakai, M. Klene, X. Li, J. E. Knox, H. P. Hratchian, J. B. Cross, V. Bakken, C. Adamo, J. Jaramillo, R. Gomperts, R. E. Stratmann, O. Yazyev, A. J. Austin, R. Cammi, C. Pomelli, J. W. Ochterski, P. Y. Ayala, K. Morokuma,

- G. A. Voth, P. Salvador, J. J. Dannenberg, V. G. Zakrzewski, S. Dapprich, A. D. Daniels, M. C. Strain, O. Farkas, D. K. Malick, A. D. Rabuck, K. Raghavachari, J. B. Foresman, J. V. Ortiz, Q. Cui, A. G. Baboul, S. Clifford, J. Cioslowski, B. B. Stefanov, G. Liu, A. Liashenko, P. Piskorz, I. Komaromi, R. L. Martin, D. J. Fox, T. Keith, M. A. Al-Laham, C. Y. Peng, A. Nanayakkara, M. Challacombe, P. M. W. Gill, B. Johnson, W. Chen, M. W. Wong, C. Gonzalez, and J. A. Pople. Gaussian 03, Revision C.02, 2004. Gaussian, Inc., Wallingford, CT, 2004.
- [141] T. Schwieger, X. Liu, H. Peisert, B. Adolphi, N. Kiriy, and M. Knupfer. Electronic properties of interfaces between different sexithiophenes and gold. *J. Appl. Phys.*, 97:123712, 2005.
- [142] R. Friedlein, X. Crispin, C. Suess, M. Pickholz, and W. R. Salaneck. The role of intermolecular polarization for the stability of lithium intercalation compounds of alpha- and beta-perylene. *J. Chem. Phys.*, 121:2239–2245, 2004.
- [143] S. Duhm, H. Glowatzki, J. P. Rabe, N. Koch, and R. L. Johnson. Influence of alkyl chain substitution on sexithienyl-metal interface morphology and energetics. *Appl. Phys. Lett.*, 88(20):203109, 2006.
- [144] S. Duhm, G. Heimel, I. Salzmann, H. Glowatzki, R. L. Johnson, A. Vollmer, J. P. Rabe, and N. Koch. Orientation-dependent ionisation energies and interface dipoles in ordered molecular assemblies. *Nature Mater.*, 7:326–332, 2008.
- [145] S. Duhm, I. Salzmann, N. Koch, H. Fukagawa, T. Kataoka, S. Hosoumi, K. Nebashi, S. Kera, and N. Ueno. Vacuum sublimed  $\alpha,\omega$ -dihexylsexithiophene thin films: Electronic structure and molecular orientation. *J. Appl. Phys.*, in press, 2008.
- [146] F. Biscarini, R. Zamboni, P. Samorí, P. Ostoja, and C. Taliani. Growth of conjugated oligomer thin films studied by atomic-force microscopy. *Phys. Rev. B*, 52:14868–14877, 1995.
- [147] R. Ruiz, D. Choudhary, B. Nickel, T. Toccoli, K.-C. Chang, A.C. Mayer, P. Clancy, J.M. Blakely, R.L. Headrick, S. Iannotta, and G.G. Malliaras. Pentacene thin film growth. *Chem. Mater.*, 16(23):4497–4508, 2004.

- [148] J. Ivanco, F. P. Netzer, and M. G Ramsey. On validity of the Schottky-Mott rule in organic semiconductors: Sexithiophene on various substrate. *J. Appl. Phys.*, 101:103712, 2007.
- [149] J. Ivanco, B. Winter, F. P. Netzer, and M. G Ramsey. Substrate-Mediated Electronic Structure and Properties of Sexiphenyl Films. *Adv. Mater.*, 15:1812–1815, 2003.
- [150] F. Amy, C. Chan, and A. Kahn. Polarization at the gold/pentacene interface. *Org. Electron.*, 6:85–91, 2005.
- [151] M. B. Casu, Y. Zou, S. Kera, D. Batchelor, Th. Schmidt, and E. Umbach. Investigation of polarization effects in organic thin films by surface core-level shifts. *Phys. Rev. B*, 76:193311, 2007.
- [152] T. C. Chiang, G. Kaindl, and T. Mandel. Layer-resolved shifts of photoemission and Auger spectra from physisorbed rare-gas multilayers. *Phys. Rev. B*, 33:695–711, 1986.
- [153] M. Coville and T. D. Thomas. Molecular effects on inner-shell lifetimes: Possible test of the one-center model of Auger decay. *Phys. Rev. A*, 43:6053–6056, 1991.
- [154] A. Föhlisch, P. Feulner, F. Hennies, A. Fink, D. Menzel, D. Sanchez-Portal, P. M. Echenique, and W. Wurth. Direct observation of electron dynamics in the attosecond domain. *Nature*, 436:373–376, 2005.
- [155] H. B. Michaelson. The work function of the elements and its periodicity. *J. Appl. Phys.*, 48:4729–4733, 1977.
- [156] H. L. Skriver and N. M. Rosengaard. Surface energy and work function of elemental metals. *Phys. Rev. B*, 46:7157–7168, 1992.
- [157] N. D. Lang and W. Kohn. Theory of Metal Surfaces: Work Function. *Phys. Rev. B*, 3:1215–1223, 1971.
- [158] M. Weinert and R. E. Watson. Contributions to the work function of crystals. *Phys. Rev. B*, 29:3001–3008, 1984.
- [159] H. Häkkinen, B. Yoon, U. Landman, X. Li, H.-J. Zhai, and L.-S. Wang. On the Electronic and Atomic Structures of Small  $Au_N$ - ( $N=4-14$ ) clusters: A Photoelectron Spectroscopy and Density-Functional Study. *J. Phys. Chem. A*, 107:6168–6175, 2003.

- [160] J. Li, X. Li, H. J. Zhai, and L. S. Wang. Au<sub>20</sub>: A Tetrahedral Cluster. *Science*, 299:864–867, 2003.
- [161] B. Servet, S. Ries, M. Trotel, P. Alnot, G. Horowitz, and F. Garnier. X-ray determination of the crystal structure and orientation of vacuum evaporated sexithiophene films. *Adv. Mater.*, 5:461–464, 1993.
- [162] J. Bernstein, J. A. R. P. Sarma, and A. Gavezzotti. Generation of unknown crystal phases for aromatic hydrocarbons by packing energy calculations. *Chem. Phys. Lett.*, 174:361–368, 1990.
- [163] T. Siegrist, R. M. Fleming, R. C. Haddon, R. A. Laudise, A. J. Lovinger, H. E. Katz, P. Bridenbaugh, and D. D. Davis. The crystal structure of the high-temperature polymorph of  $\alpha$ -hexathienyl ( $\alpha$ -6T/HT). *J. Mater. Res.*, 10:2170–2173, 1995.
- [164] C. C. Mattheus, G. A. de Wijs, R. A. de Groot, and T. T. M. Palstra. Modeling the Polymorphism of Pentacene. *J. Am. Chem. Soc.*, 125:6323–6330, 2003.
- [165] M. Oehzelt, R. Resel, C. Suess, R. Friedlein, and W. R. Salaneck. Crystallographic and morphological characterization of thin pentacene films on polycrystalline copper surfaces. *J. Chem. Phys.*, 124:054711, 2006.
- [166] M. Moret, M. Campione, A. Borghesi, L. Miozzo, A. Sassella, S. Trabatttoni, B. Lotz, and A. Thierry. Structural characterisation of single crystals and thin films of  $\alpha,\omega$ -dihexylquaterthiophene. *J. Mater. Chem.*, 15:2444 – 2449, 2005.
- [167] S. Masuda, H. Hayashi, and Y. Harada. Spatial distribution of the wave functions of a graphite surface studied by use of metastable-atom electron spectroscopy. *Phys. Rev. B*, 42:3582–3585, 1990.
- [168] T. Takahashi, H. Tokailin, and T. Sagawa. Angle-resolved ultraviolet photoelectron spectroscopy of the unoccupied band structure of graphite. *Phys. Rev. B*, 32:8317–8324, 1985.
- [169] H. Glowatzki, S. Duhm, K.-F. Braun, J. P. Rabe, and N. Koch. Molecular chains and carpets of sexithiophenes on Au(111). *Phys. Rev. B*, 76:125425, 2007.
- [170] A. Stabel and J. P. Rabe. Scanning tunneling microscopy of alkylated oligothiophenes at interfaces with graphite. *Synth. Met.*, 67:47–53, 1994.

- [171] H. Ozaki and Y. Harada. Penning Ionization Electron Spectroscopy of n-Alkane Ultrathin Films. Molecular Orbitals and Orientation of Molecules. *J. Am. Chem. Soc.*, 112:5735–5740, 1990.
- [172] S. P. Chenakin, B. Heinz, and H. Morgner. Sputtering of hexadecanethiol monolayers self-assembled onto Ag(111). *Surf. Sci.*, 397:84–100, 1998.
- [173] N. Koch, S. Duhm, J. P. Rabe, A. Vollmer, and R. L. Johnson. Optimized hole injection with strong electron acceptors at organic-metal interfaces. *Phys. Rev. Lett.*, 95:237601, 2005.
- [174] F. Jäckel. *Self-Assembly and Electronic Properties of Conjugated Molecules: Towards Mono-Molecular Electronics*. PhD thesis, Humboldt University Berlin, 2005.
- [175] J. M. Lindquist and J. C. Hemminger. High-resolution core level photoelectron spectra of solid TCNQ: determination of molecular orbital spatial distribution from localized shake-up features. *J. Phys. Chem.*, 92:1394–1396, 1988.
- [176] C. Rojas, J. Caro, M. Grioni, and J. Fraxedas. Surface characterization of metallic molecular organic thin films: tetrathiafulvalene tetracyanoquinodimethane. *Surf. Sci.*, 482-485:546–551, 2001.
- [177] S. Hotta and K. Waragai. Alkyl-substituted oligothiophenes: crystallographic and spectroscopic studies of neutral and doped forms. *J. Mater. Chem.*, 1:835 – 842,, 1991.
- [178] G. Brocks. Theoretical study of the charge transfer in the organic crystal of dimethylquaterthiophene and tetrafluoro-tetracyanoquinodimethane. *Phys. Rev. B*, 55:6816–6819, 1997.
- [179] N. D. Lang and A. R. Williams. Theory of local-work-function determination by photoemission from rare-gas adsorbates. *Phys. Rev. B*, 25: 2940–2942, 1982.
- [180] R. Fischer, S. Schuppler, N. Fischer, Th. Fauster, and W. Steinmann. Image states and local work function for Ag/Pd(111). *Phys. Rev. Lett.*, 70:654–657, 1993.
- [181] G. Koller, F. P. Netzer, and M. G. Ramsey. Band alignment on a nanoscopically patterned inorganic–organic interface. *Appl. Phys. Lett.*, 83:563–565, 2003.

- [182] I. G. Hill, A. Kahn, Z. G. Soos, and R. A. Pascal, Jr. Charge-separation energy in films of  $\pi$ -conjugated organic molecules. *Chem. Phys. Lett.*, 327:181–188, 2000.
- [183] J. A. Venables, G. D. T. Spiller, and M. Hanbücken. Nucleation and growth of thin films. *Rep. Prog. Phys.*, 47:399–459, 1984.
- [184] C. Ecker. private communication, 2005.
- [185] S. Duhm, H. Glowatzki, J. P. Rabe, N. Koch, and R. L. Johnson. Spontaneous charge transfer at organic-organic homointerfaces to establish thermodynamic equilibrium. *Appl. Phys. Lett.*, 90:122113, 2007.
- [186] S. Duhm, A. Gerlach, I. Salzmann, B. Bröker, R. L. Johnson, F. Schreiber, and N. Koch. PTCDA on Au(111), Ag(111) and Cu(111): Correlation of interface charge transfer to bonding distance. *Org. Electron.*, 9:111–118, 2008.
- [187] N. Koch, A. Gerlach, S. Duhm, H. Glowatzki, G. Heimel, A. Vollmer, Y. Sakamoto, T. Suzuki, J. Zegenhagen, J. P. Rabe, and F. Schreiber. Adsorption induced intramolecular dipole: Correlating molecular conformation and interface electronic structure. *J. Am. Chem. Soc.*, 130:7300–7304, 2008.
- [188] Y. Zou, L. Kilian, A. Schöll, Th. Schmidt, R. Fink, and E. Umbach. Chemical bonding of PTCDA on Ag surfaces and the formation of interface states. *Surf. Sci.*, 600:1240–1251, 2006.
- [189] M. Eremtchenko, D. Bauer, J. A. Schaefer, and F. S. Tautz. Polycyclic aromates on close-packed metal surfaces: functionalization, molecular chemisorption and organic epitaxy. *New J. Phys.*, 6:4, 2004.
- [190] Y. Hirose, A. Kahn, V. Aristov, P. Soukiassian, V. Bulovic, and S. R. Forrest. Chemistry and electronic properties of metal-organic semiconductor interfaces: Al, Ti, In, Sn, Ag, and Au on PTCDA. *Phys. Rev. B*, 54:13748–13758, 1996.
- [191] G. Gavrila, D. R. T. Zahn, and W. Braun. High resolution photoemission spectroscopy: Evidence for strong chemical interaction between Mg and 3,4,9,10-perylene-tetracarboxylic dianhydride. *Appl. Phys. Lett.*, 89:162102, 2006.
- [192] I. G. Hill, A. Rajagopal, A. Kahn, and Y. Hu. Molecular level alignment at organic semiconductor-metal interfaces. *Appl. Phys. Lett.*, 73:662–664, 1998.

- [193] E. Kawabe, H. Yamane, K. Koizumi, R. Sumii, K. Kanai, Y. Ouchi, and K. Seki. The Electronic Structure and the Energy Level Alignment at the Interface Between Organic Molecules and Metals. *Mater. Res. Soc. Symp. Proc.*, 965:S09, 2007.
- [194] R. Agrawal and S. Ghosh. Electrical characterization of fermi level pinning in metal/3,4,9,10 perylenetetracarboxylic dianhydride interfaces. *Appl. Phys. Lett.*, 89:222114, 2006.
- [195] P. Fenter, F. Schreiber, L. Zhou, P. Eisenberger, and S. R. Forrest. In situ studies of morphology, strain, and growth modes of a molecular organic thin film. *Phys. Rev. B*, 56:3046–3053, 1997.
- [196] T. Schmitz-Hübsch, T. Fritz, F. Sellam, R. Staub, and K. Leo. Epitaxial growth of 3,4,9,10-perylene-tetracarboxylic-dianhydride on Au(111): A STM and RHEED study. *Phys. Rev. B*, 55:7972–7976, 1997.
- [197] N. Nicoara, E. Román, J. M. Gómez-Rodríguez, J. A. Martín-Gago, and J. Méndez. Scanning tunneling and photoemission spectroscopies at the PTCDA/Au(111) interface. *Org. Electron.*, 7:287–294, 2006.
- [198] M. Schneider, E. Umbach, and M. Sokolowski. Growth-dependent optical properties of 3,4,9,10-perylenetetracarboxylicacid-dianhydride (PTCDA) films on Ag(1 1 1). *Chem. Phys.*, 325:185–192, 2006.
- [199] V. Shklover, F. S. Tautz, R. Scholz, S. Sloboshanin, M. Sokolowski, J. A. Schaefer, and E. Umbach. Differences in vibronic and electronic excitations of PTCDA on Ag(111) and Ag(110). *Surf. Sci.*, 454-456: 60–66, 2000.
- [200] Th. Wagner, A. Bannani, C. Bobisch, H. Karacuban, M. Stöhr, M. Gabriel, and R. Möller. Growth of 3,4,9,10-perylenetetracarboxylic-dianhydride crystallites on noble metal surfaces. *Org. Electron.*, 5:35–43, 2004.
- [201] Th. Wagner, A. Bannani, C. Bobisch, H. Karacuban, and R. Möller. The initial growth of PTCDA on Cu(111) studied by STM. *J. Phys. Condens. Matter*, 19:056009, 2007.
- [202] B. Krause, A. C. Dürr, F. Schreiber, H. Dosch, and O. H. Seeck. Thermal stability and partial dewetting of crystalline organic thin films: 3,4,9,10-perylenetetracarboxylic dianhydride on Ag(111). *J. Chem. Phys.*, 119:3429–3435, 2003.



- [203] F. S. Tautz, M. Eremtchenko, J. A. Schaefer, M. Sokolowski, V. Shklover, and E. Umbach. Strong electron-phonon coupling at a metal/organic interface: PTCDA/Ag(111). *Phys. Rev. B*, 65:125405, 2002.
- [204] E. V. Tsiper, Z. G. Soos, W. Gao, and A. Kahn. Electronic polarization at surfaces and thin films of organic molecular crystals: PTCDA. *Chem. Phys. Lett.*, 360:47–52, 2002.
- [205] A. Schmidt, T. J. Schuerlein, G. E. Collins, and N. R. Armstrong. Ordered Ultrathin Films of Perylenetetracarboxylic Dianhydride (PTCDA) and Dimethylperylenebis(dicarboximide) (Me-PTCDI) on Cu(100): Characterization of Structure and Surface Stoichiometry by LEED, TDMS, and XPS. *J. Phys. Chem.*, 99:11770–11779, 1995.
- [206] I. G. Hill, A. J. Mäkinen, and Z. H. Kafafi. Initial stages of metal/organic semiconductor interface formation. *J. Appl. Phys.*, 88: 889–895, 2000.
- [207] I. Chizhov, A. Kahn, and G. Scoles. Initial growth of 3,4,9,10-perylenetetracarboxylic-dianhydride (PTCDA) on Au(111): a scanning tunneling microscopy study. *J. Cryst. Growth*, 208:449–458, 2000.
- [208] L. Kilian, E. Umbach, and M. Sokolowski. A refined structural analysis of the PTCDA monolayer on the reconstructed Au(111) surface—“Rigid or distorted carpet?”. *Surf. Sci.*, 600:2633–2643, 2006.
- [209] J. Kröger, H. Jensen, R. Berndt, R. Rurali, and N. Lorente. Molecular orbital shift of perylenetetracarboxylic-dianhydride on gold. *Chem. Phys. Lett.*, 438:249–253, 2007.
- [210] B. Krause, A. C. Dürr, K. Ritley, F. Schreiber, H. Dosch, and D. Smilgies. Structure and growth morphology of an archetypal system for organic epitaxy: PTCDA on Ag(111). *Phys. Rev. B*, 66:235404, 2002.
- [211] B. Krause, F. Schreiber, H. Dosch, A. Pimpinelli, and O. H. Seeck. Temperature dependence of the 2D-3D transition in the growth of PTCDA on Ag(111): A real-time X-ray and kinetic Monte Carlo study. *Europhys. Lett.*, 65(3):372–378, 2004.
- [212] M. Möbus, N. Karl, and T. Kobayashi. Structure of perylene-tetracarboxylic-dianhydride thin films on alkali halide crystal substrates. *J. Cryst. Growth*, 116:495–504, 1992.

- [213] I. G. Hill and A. Kahn. Energy level alignment at interfaces of organic semiconductor heterostructures. *J. Appl. Phys.*, 84:5583–5586, 1998.
- [214] H. Vázquez, W. Gao, F. Flores, and A. Kahn. Energy level alignment at organic heterojunctions: Role of the charge neutrality level. *Phys. Rev. B*, 71:041306, 2005.
- [215] C. Stadler, S. Hansen, F. Pollinger, C. Kumpf, E. Umbach, T.-L. Lee, and J. Zegenhagen. Structural investigation of the adsorption of SnPc on Ag(111) using normal-incidence x-ray standing waves. *Phys. Rev. B*, 74:035404, 2006.
- [216] L. Gavioli, M. Fanetti, M. Sancrotti, and M. G. Betti. Long-range-ordered pentacene chains assembled on the Cu(119) vicinal surface. *Phys. Rev. B*, 72:035458, 2005.
- [217] P. S. Bagus, K. Hermann, and C. Wöll. The interaction of C<sub>6</sub>H<sub>6</sub> and C<sub>6</sub>H<sub>12</sub> with noble metal surfaces: Electronic level alignment and the origin of the interface dipole. *J. Chem. Phys.*, 123:184109, 2005.

# Abbreviations

The acronyms for the molecules used in this work are not contained in this list, details are given in Tab. 3.1 and Fig. 3.1.

BE	binding energy
CNL	charge neutrality level
COM	conjugated organic molecule
CT	charge transfer
CTC	charge transfer complex
DFT	density functional theory
$d_h$	bonding distance
DOS	density of occupied states
$e^-$	electron
$E_B$	binding energy
$E_{Bragg}$	Bragg energy
$E_F$	Fermi-level
$E_{kin}$	kinetic energy
$E_{vac}$	vacuum level
$f_H$	coherent fraction
GID	grazing incidence diffraction
$h$	Planck's constant
HOMO	highest occupied molecular orbital
HOPG	highly oriented pyrolytic graphite
IE	ionization energy
L1	(lying) monolayer
L2	(standing) multilayer
LEED	low electron energy diffraction
LUMO	lowest unoccupied molecular orbital
MAES	metastable atom electron spectroscopy

MO	molecular orbital
$n_D$	dipole surface density
OLED	organic light emitting device
PES	photoelectron spectroscopy
$P_H$	coherent position
$P_h$	positive polarization energy
q	elementary charge
$q_z$	momentum transfer
QCM	quartz crystal microbalance
SECO	secondary electron cut off
STM	scanning tunneling microscopy
STS	scanning tunneling spectroscopy
UHV	ultrahigh vacuum
UPS	ultraviolet photoelectron spectroscopy
UV	ultraviolet
XPS	X-ray photoelectron spectroscopy
XRD	X-ray diffraction
XRR	X-ray reflectivity
XSW	X-ray standing waves
$Y_p$	X-ray standing wave yield
$\alpha_i$	incident angle
$\alpha_f$	exit angle
$\Delta_e$	electron injection barrier
$\Delta_h$	hole injection barrier
$\Delta_{HOMO}$	HOMO shift
$\Delta_{vac}$	vacuum level shift
$\Delta\phi$	work function change
$\Delta\phi_{L1,L2}$	vacuum level shift at the L1/L2 interface
$\epsilon$	dielectric constant
$\epsilon_0$	vacuum permittivity
$\theta$	coverage
$\theta_e$	electron take-off angle
$\Theta_B$	Bragg angle
$\vec{\mu}$	dipole moment
$\mu_{\perp}$	perpendicular dipole moment
$\nu$	frequency
$\phi$	work function

# Publications

Publications of which parts belong to this thesis' work and which have been discussed in chapter 4 are marked by a fat indenture number.

- 1.** Tuning the Hole Injection Barrier Height at Organic/Metal Interfaces With (Sub)Monolayers of Electron Acceptor Molecules  
N. Koch, S. Duhm, J. P. Rabe, S. Rentenberger, R. L. Johnson, J. Klankermayer and F. Schreiber  
Appl. Phys. Lett. **87** (2005), 101905
- 2.** Optimized Hole Injection with Strong Electron Acceptors at Organic-Metal Interfaces  
N. Koch, S. Duhm, J. P. Rabe, A. Vollmer and R. L. Johnson  
Phys. Rev. Lett. **95** (2005), 237601
- 3.** Influence of Alkyl Chain Substitution on Sexithienyl-Metal Interface Morphology and Energetics  
S. Duhm, H. Glowatzki, J. P. Rabe, R. L. Johnson and N. Koch  
Appl. Phys. Lett. **88** (2006), 203109
- 4.** Morphology, Interfacial Electronic Structure, and Optical Properties of Oligothiophenes Grown on ZnSe(100) by Molecular Beam Deposition  
S. Blumstengel, N. Koch, S. Duhm, H. Glowatzki, R. L. Johnson, C. Xu, A. Yassar, J. P. Rabe and F. Henneberger  
Phys. Rev. B **73** (2006), 165323
- 5.** Weak Charge Transfer between an Acceptor Molecule and Metal Surfaces Enabling Organic/Metal Energy Level Tuning  
S. Duhm, H. Glowatzki, V. Cimpeanu, J. Klankermayer, J. P. Rabe, R. L. Johnson and N. Koch  
J. Phys. Chem. B **110** (2006), 21069

6. The effect of Fluorination on Pentacene/Gold Interface Energetics and Charge Reorganization Energy  
N. Koch, A. Vollmer, S. Duhm, Y. Sakamoto and T. Suzuki  
Adv. Mater. **19** (2007), 112
  
7. Spontaneous Charge Transfer at Organic-Organic Homo-Interfaces to Establish Thermodynamic Equilibrium  
S. Duhm, H. Glowatzki, J. P. Rabe, R. L. Johnson and N. Koch  
Appl. Phys. Lett. **90** (2007), 122113
  
8. The impact of low 6,13-pentacenequinone concentration on pentacene thin film growth  
I. Salzmann, S. Duhm, R. Opitz, J. P. Rabe and N. Koch  
Appl. Phys. Lett. **91** (2007), 051919
  
9. Internal structure of nanoporous TiO<sub>2</sub> / polyion thin films prepared by layer-by-layer deposition  
R. Kniprath, S. Duhm, H. Glowatzki, N. Koch, S. Rogaschewski, J. P. Rabe and S. Kirstein  
Langmuir **23** (2007) 9860
  
10. Molecular chains and carpets of sexithiophenes on Au(111)  
H. Glowatzki, S. Duhm, K. F. Braun, J. P. Rabe and N. Koch  
Phys. Rev. B **76** (2007), 125425
  
11. Impact of Bidirectional Charge Transfer and Molecular Distortions on the Electronic Structure of a Metal-Organic Interface  
L. Romaner, G. Heimel, J.-L. Brédas, A. Gerlach, F. Schreiber, R. L. Johnson, J. Zegenhagen, S. Duhm, N. Koch and E. Zojer  
Phys. Rev. Lett. **99** (2007), 256801
  
12. Sub-nm Control of the Inter-layer Spacing in Thin Films of Inter-calated Rodlike Conjugated Molecules  
J.-O. Vogel, I. Salzmann, R. Opitz, S. Duhm, B. Nickel, J. P. Rabe and N. Koch  
J. Phys. Chem. B, **111** (2007), 14097

13. PTCDA on Au(111), Ag(111) and Cu(111): Correlation of interface charge transfer to bonding distance  
S. Duhm, A. Gerlach, I. Salzmänn, B. Bröker, R. L. Johnson, F. Schreiber and N. Koch  
Org. Electron. **9** (2008), 111
14. Orientation-dependent ionization energies and interface dipoles in ordered molecular assemblies  
S. Duhm, G. Heimel, I. Salzmänn, H. Glowatzki, R. L. Johnson, A. Vollmer, J. P. Rabe and N. Koch  
Nature Mater., **7** (2008), 326
15. Adsorption-Induced Intramolecular Dipole: Correlating Molecular Conformation and Interface Electronic Structure  
N. Koch, A. Gerlach, S. Duhm, H. Glowatzki, G. Heimel, A. Vollmer, Y. Sakamoto, T. Suzuki, J. Zegenhagen, J. P. Rabe and F. Schreiber  
J. Am. Chem. Soc., **130** (2008), 7300
16. Structural Order in Perfluoropentacene Thin Films and Heterostructures with Pentacene  
I. Salzmänn, S. Duhm, G. Heimel, J. P. Rabe, N. Koch, M. Oehzelt, Y. Sakamoto and T. Suzuki  
Langmuir, **24** (2008), 7294
17. Vacuum sublimed  $\alpha,\omega$ -dihexylsexithiophene thin films: Electronic structure and molecular orientation  
S. Duhm, I. Salzmänn, N. Koch, H. Fukagawa, T. Kataoka, S. Hosoumi, K. Nebashi, S. Kera and N. Ueno  
J. Appl. Phys., **in press**
18. Structural and electronic properties of pentacene-fullerene heterojunctions  
I. Salzmänn, S. Duhm, R. Opitz, R. L. Johnson, J. P. Rabe and N. Koch  
**submitted**

19. Tuning the ionization energy of organic semiconductor films: The role of polar intra-molecular bonds  
I. Salzmann, S. Duhm, G. Heimel, M. Oehzelt, R. Kniprath, R. L. Johnson, J. P. Rabe and N. Koch  
**submitted**



# Acknowledgements

This thesis would not have been possible without the help of many people. Dr. Norbert Koch gave me the possibility to conduct this work in his research group. He introduced me to FLIPPER II at HASYLAB, where I performed most of the experiments. Beside his enormous experimental experience he also shared his overwhelming knowledge in organic electronics with me – especially in all the various thin film properties which can be measured with UPS. Prof. Robert L. Johnson (Universität Hamburg) is keeping FLIPPER II (including a PDP-11) running since 1982. Since FLIPPER II is –to my knowledge– one of the world leading machines to measure UPS on organic thin films, this extraordinary engagement cannot be appreciated too much.

The synchrotron work was always done in teamwork. At FLIPPER II most of the measurements were done with Hendrik Glowatzki. At some beamtimes also Dr. Stephan Rentenberger (TU Graz), Dr. Alexander Gerlach (Universität Tübingen), Benjamin Bröker and Ingo Salzmänn participated. The XRD measurements at the W1 beamline at HASYLAB were lead managed by Ingo Salzmänn, he also did most of the analysis of the results. The local contact Dr. Wolfgang Caliebe provided an excellent machine. The XPS and UPS measurements at BESSY were done together with Dr. Antje Vollmer (BESSY) and Dr. Norbert Koch. Besides the marvelous maintenance of the SurICat machine, Dr. Antje Vollmer was also involved in measurements and discussions. The XSW measurements at the ESRF were done in collaboration with Prof. Frank Schreiber (Universität Tübingen) and Dr. Alexander Gerlach. Both are renowned experts in this rather exotic technique and let me and Dr. Norbert Koch participate on their expertise. Dr. Jörg Zegenhagen and Dr. Tien-Lien Lee (both ESRF) gave us the possibility to measure with one of the rare state-of-the-art XSW-machines.

Prof. Nobuo Ueno (Chiba University) gave me the opportunity to visit his research group and to extend the spectroscopic methods to the metastable one. During my stay he as well as Prof. Satoshi Kera have always been interested in fruitful discussions. The laboratory work was done together with Shunsuke Hosoumi, Kohjiro Nebashi, Dr. Hirohiko Kampo Fukagawa

and Takashi Kataoka, the latter two also contributed helpful ideas to data analysis.

Without knowing them personally, I want to mention Dr. Jürgen Klankermayer and Dr. Valentin Cimpeanu (both RWTH Aachen), who synthesized FAQ and TCAQ.

Although most of the work was done at synchrotron facilities also the work of several people at Humboldt University has to be acknowledged. Dr. Georg Heibel had the idea of orientation dependent ionization energies of van der Waals crystals and did the calculations. Prof. Jürgen P. Rabe was a critical reader of my manuscripts and always provided elucidating suggestions. Evi Poblentz, Lothar Geyer and Sabine Schönherr provided excellent technical and administrative support. Ingo Salzmänn and Carsten Jost shared the office with me in a very pleasant manner. Ingo Salzmänn again and Beate Müller had always time for stimulating discussions as the time for proof-reading this thesis.

# Selbständigkeitserklärung

Hiermit erkläre ich, die Dissertation selbständig und nur unter Verwendung der angegebenen Hilfen und Hilfsmittel angefertigt zu haben.

Ich habe mich anderwärts nicht um einen Doktorgrad beworben und besitze einen entsprechenden Doktorgrad nicht.

Ich erkläre die Kenntnisnahme der dem Verfahren zugrunde liegenden Promotionsordnung der Mathematisch-Naturwissenschaftlichen Fakultät I der Humboldt-Universität zu Berlin.

Berlin, 20. März 2008